Hydrotrioxide (ROOOH) formation in the atmosphere

Torsten Berndt,[1*] Jing Chen,[2] Eva R. Kjærgaard,[2] Kristian H. Møller,[2] Andreas Tilgner,[1] Erik H. Hoffmann,[1] Hartmut Herrmann,[1] John D. Crounse,[3] Paul O. Wennberg,[3,4] Henrik G. Kjaergaard[2*]

[1] Atmospheric Chemistry Department (ACD), Leibniz Institute for Tropospheric Research (TROPOS), Permoserstraße 15, 04318 Leipzig, Germany.
[2] Department of Chemistry, University of Copenhagen, Universitetsparken 5, DK-2100 Ø, Denmark.
[3] Division of Geological and Planetary Sciences, California Institute of Technology, Pasadena, California 91125, United States.
[4] Division of Engineering and Applied Science, California Institute of Technology, Pasadena, California 91125, United States.

Abstract:

Organic hydrotrioxides, ROOOH, are known to be strong oxidants used in organic synthesis. Previously, there has been speculated that they are formed in the atmosphere via the gas-phase reaction of organic peroxy radicals, RO_2, with OH. Here, we report direct observation of ROOOH formation from several atmospherically relevant RO_2 radicals. Kinetic analysis confirmed rapid RO_2 + OH reactions forming ROOOH with rate coefficients close to the collision limit. For the OH-initiated degradation of isoprene, global modeling predicts molar hydrotrioxide formation yields of up to 1 % representing an annual ROOOH formation of about 10 million metric tons. The atmospheric lifetime of ROOOH is estimated to be minutes to hours. Hydrotrioxides represent a previously omitted substance class in the atmosphere whose impact needs to be examined.

One-sentence summary:

Direct mass spectrometric detection of the proposed, but hitherto unverified, substance class "hydrotrioxide" for atmospheric conditions is reported.

Hydrotrioxides (ROOOH) are known, thermally unstable products formed in the low-temperature ozonolysis of saturated organic compounds in organic solvents. They are a chemical source of the powerful oxidant singlet molecular oxygen ($^1O_2$) released during their decomposition. (*1-3*) Accordingly, hydrotrioxides are used in preparative chemistry to form the corresponding oxetane and carbonyl products in the reaction with alkenes mostly carried out at dry-ice temperature. (*4*)

In atmospheric gas-phase chemistry, theoretical calculations have proposed the formation of hydrotrioxides as intermediates in the reaction of RO_2 radicals with OH, pathway (1). (*5, 6*) The rapid radical recombination reaction is exothermic by about 130 kJ mol^{-1}, nearly independent of the RO_2 radical, initially forming the energy-rich ROOOH*. This chemically excited species can decompose leading to the corresponding alkoxy radical RO and HO_2, pathway (2), or to a lesser extent to an alcohol and O_2, pathway (3). In competition with decomposition, collisions with bath gas molecules, M, result in thermalized ROOOH, pathway (4). (*5-8*)

$RO_2 + OH$	$\rightarrow$	ROOOH*	(1)
ROOOH*	$\rightarrow$	$RO + HO_2$	(2)
ROOOH*	$\rightarrow$	$ROH + O_2$	(3)
ROOOH* + M	$\rightarrow$	ROOOH + M	(4)

Previous experimental investigations of the RO_2 + OH reaction at 298 K and 50 Torr He found a decreasing HO_2 yield with the RO_2 radical size increasing from C_1 to C_4. For CH_3O_2, the HO_2 yield was 0.90 ± 0.10, which decreased to 0.15 ± 0.03 for n-$C_4H_9O_2$. (*7*) Calculations, supported by these experimental findings, suggested that at 298 K and 1 bar N_2 channel (4) was the dominant fate of ROOOH* in the case of $C_2H_5O_2$ (78 %) and larger RO_2 radicals (> 95 %), and for CH_3O_2 radicals decomposition into CH_3O and HO_2 via channel (2) still dominates. (*7, 8*) Thus, with exception of CH_3O_2 radicals, formation of the thermalized ROOOH is the expected dominant product from RO_2 + OH reactions in the atmosphere.

There has been a lot of speculation in the literature about the physical chemistry of the reactions of RO_2 radicals with OH in the atmosphere. All evidence that hydrotrioxides are formed has, to date, been indirect and an experimental proof of hydrotrioxides is missing up to now. (*5-9*)

Here, we conclusively demonstrate via their direct detection that hydrotrioxide (ROOOH) formation takes place from RO_2 + OH reactions under atmospheric conditions. The investigations were conducted in a free-jet flow system at 295 ± 2 K, a pressure of 1 bar air and a reaction time of 7.5 s using product monitoring by chemical ionization mass spectrometry. (*10, 11*) Quantum chemical calculations (*12-14*) were carried out in support of the reaction mechanisms as well as the thermal and photo stability of hydrotrioxides. (*15*)

We observed a strong signal being consistent with ROOOH formation in the reaction of OH radicals with trimethylamine ($N(CH_3)_3$) using iodide for product ionization in the mass-spectrometric detection (Fig. S **1**). In this reaction system, an efficient autoxidation mechanism (*16*) (repeated RO_2 isomerization and O_2 addition) rapidly formed the RO_2 radical $(HOOCH_2)_2NCH_2O_2$ (**I**) as a main product. (*12, 17*) The RO_2 radical (**I**) can react with OH to form the hydrotrioxide (**III**), however, in competition with unimolecular RO_2 isomerization forming the dihydroperoxy amide (**II**) and with the RO_2 self-reaction, **I** + **I**, forming the accretion product (**IV**), as illustrated in Scheme 1.

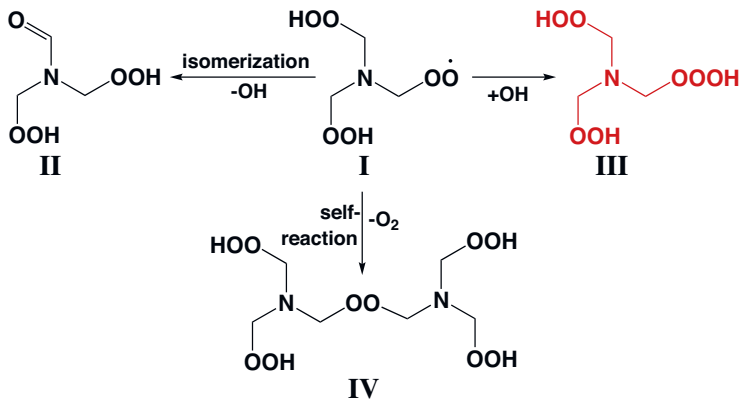

Scheme 1. Product formation starting from the RO_2 radical I.

The signal with the mass of the hydrotrioxide $(HOOCH_2)_2NCH_2OOOH$ **(III)** steeply increased with increasing concentrations of the OH precursor, IPN, i.e., for rising OH and RO_2 radical concentrations in the experiment (Fig. 1A). The signal of **III** behaved similar to that of the accretion product **IV** formed in the self-reaction of the RO_2 radical **I**. Both followed second-order kinetics (*18*) in clear contrast to the first-order kinetics of amide $(HOOCH_2)_2NCHO$ (**II**) formation, arising from the RO_2 isomerization of **I**. (*12*) Because OH and RO_2 radical concentrations increased in a similar way with increasing IPN

concentrations, the product of the RO_2 + OH reaction increased almost parallel to the accretion product **IV** (Fig. 1A).

For further mechanistic validation of ROOOH formation, we increased the OH level in the experiment by lowering the trimethylamine concentration for a constant OH production rate using unchanged isopropyl nitrite (IPN) and nitric oxide (NO) in the photolysis (Fig. 1B). Here, the OH level grew due to the decreasing OH loss rate with lowering of the main OH consumer trimethylamine. At sufficiently small trimethylamine concentrations, OH started to react significantly with CO, methane and other trace gases in the air resulting in clear weakening of the RO_2 radical **I** production (Fig. 1B). Simultaneously, the signals of the RO_2 isomerization product **II** and the accretion product **IV** declined. In contrast, the signal attributed to the hydrotrioxide **III** showed a clear increase with increasing OH level, which emphasizes that **III** has to be formed in a second OH reaction subsequent to the initial OH + trimethylamine reaction forming **I**. Additional tests revealed that the hydrotrioxide formation was not influenced by interfering processes either during product ionization and photolysis (Fig. S2), or by the presence of water vapor (Fig. S3), or by elevated NO concentrations (Fig. S4). Using modelled OH concentrations, the linear dependence of signal(ROOOH) vs. signal(RO_2) × $[OH]_{model}$ was found to be in accordance with the expected formation mechanism of ROOOH (Fig. S5). (*15*) OH radical measurements in amine systems were not possible with our technique preventing a more accurate analysis.

The same product formation from OH + trimethylamine, including hydrotrioxide production, was also measured using nitrate as the reagent ion (Fig. S6). H/D exchange experiments in the presence of heavy water (*10, 19*) (to determine the number of weakly bound, exchangeable, H atoms) showed a signal shift by 3 mass units in the mass spectrum, in accord with the presence of two OOH groups and the OOOH group further supporting the structure of **III** (Fig. S7). All experimental findings were consistent with the formation of the hydrotrioxide **III** via a RO_2 + OH reaction.

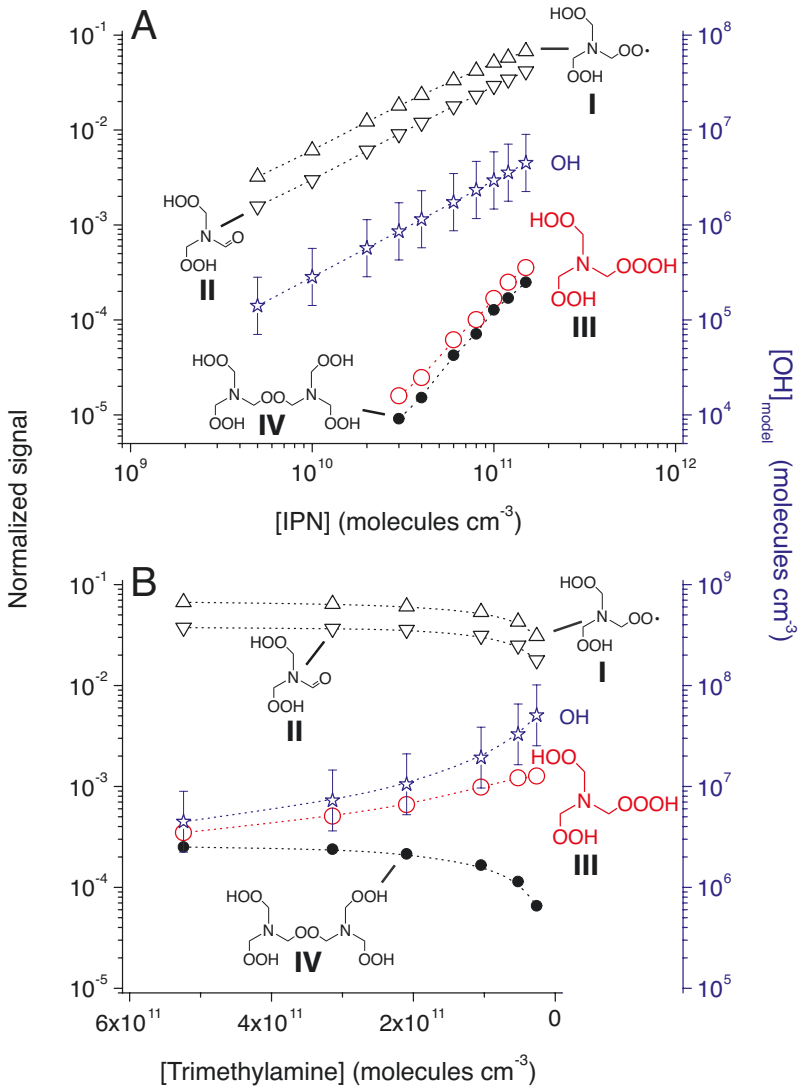

Fig. 1: Product formation from OH + trimethylamine for increasing OH levels. (**A**) Rising OH and RO_2 radical levels were due to increasing IPN for otherwise constant reactant concentrations, [NO] = 1.0×10^{10} and [trimethylamine] = 5.2×10^{11} molecules cm^{-3}. (**B**) Rising OH levels resulted from constant OH production, i.e., constant IPN and NO concentrations ([IPN] = 1.5×10^{11} and [NO] = 1.0×10^{10} molecules cm^{-3}), and lowering of the main OH consumer trimethylamine. In both experiments, OH radicals were produced from IPN photolysis in air whereby the OH generation finally proceeded via $NO + HO_2 \rightarrow OH + NO_2$. Product signals were measured with an uncertainty of < 20 %. Stated OH concentrations were taken from modelling with an assumed uncertainty of a factor of 2.

In Fig. 2, we show the calculated energy diagram of reaction (1) and (2) for the observed hydrotrioxide $(HOOCH_2)_2NCH_2OOOH$. The decomposition of the hydrotrioxide leading to the alkoxy

radical and HO_2 was about 20 kJ mol^{-1} lower in energy than that leading to the RO_2 radical and OH, in overall agreement with previous calculations performed on small C_1 - C_4 hydrotrioxides. (*5, 7*) Formation of three strong internal hydrogen bonds in $(HOOCH_2)_2NCH_2OOOH$ increased its thermostability, compared with that of less functionalized hydrotrioxides. (*15*)

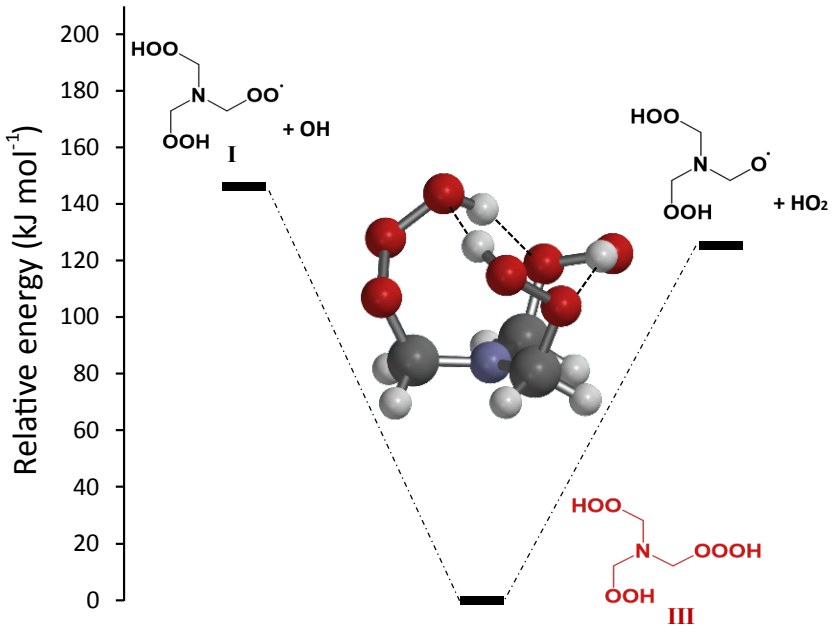

Fig. 2: Energy diagram for the formation of hydrotrioxide $(HOOCH_2)_2NCH_2OOOH$ (III). Its formation from $(HOOCH_2)_2NCH_2OO$ **(I)** + OH was exothermic by 146 kJ mol^{-1} and its decomposition into the corresponding alkoxy radical and HO_2 was endothermic by 126 kJ mol^{-1}. The lowest energy conformer of the hydrotrioxide is shown and dashed lines illustrate the three hydrogen bonds. The zero point vibrational energy corrected electronic energies were calculated at the UCCSD(T)-F12/VDZ-F12//M06-2X/aug-cc-pVTZ level. (*15*)

ROOOH formation was also probed in the reaction of OH radicals with isoprene (C_5H_8), one of the most important non-methane hydrocarbons in the atmosphere (Fig. S8). (*20*) Here, different isomeric RO_2 radicals were formed due to isoprene´s structure and the different positions of OH and O_2 addition as well as the RO_2 interconversion in this system. (*21, 22*) Moreover, RO_2 autoxidation led to a suite of different oxidized RO_2 radicals $HO\text{-}C_5H_8(O_2)_xO_2$, x = 0, 1, 2. (*11, 14, 21-23*) In Fig. 3, we show the results from an experiment with rising OH level due to lowering of isoprene in the reaction gas for constant photolysis conditions. The OH concentration was determined indirectly by monitoring SO_3 formation from OH +

SO_2. The small SO_2 addition did not disturb the OH + isoprene reaction (Fig. S9). Signals consistent with hydrotrioxides HO-$C_5H_8(O_2)_xOOOH$, x = 0 and 1, emerged beside those from the corresponding RO_2 radicals. Both substance classes showed the expected behavior, i.e., the RO_2 radical concentrations decreased with lowering of the isoprene concentration and the ROOOH compounds increased proportional to the product $[RO_2] \times [OH]$. Experiments with rising OH and RO_2 radical concentrations, due to increasing IPN concentrations, confirmed these findings (Fig. S10).

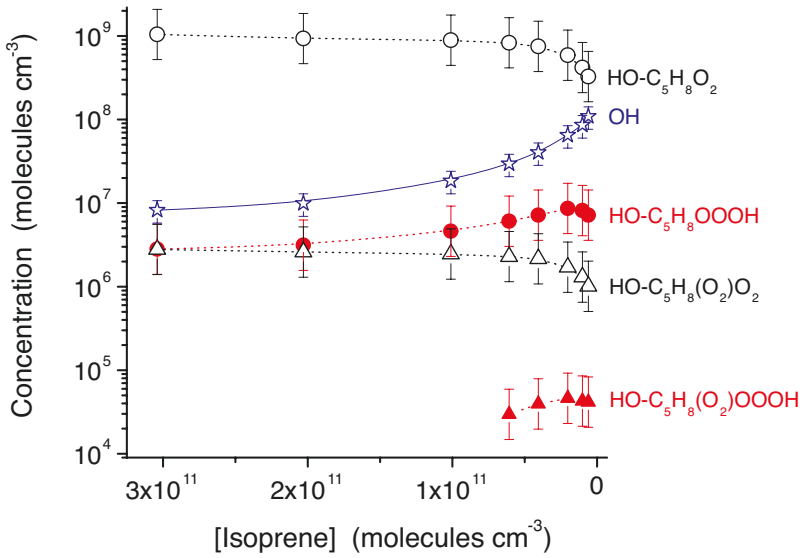

Fig. 3: Formation of RO_2 radicals and hydrotrioxides from OH + isoprene. Product concentrations with an uncertainty of a factor of 2 were obtained using calibration factors from former investigations. (*15*) Increasing OH concentrations (blue stars) for constant OH production in the IPN photolysis ([IPN] = 2.15×10^{11} and [NO] = 1.0×10^{10} molecules cm^{-3}) were due to lowering of the OH loss rate by reducing the main consumer isoprene. Iodide was used as the reagent ion. The uncertainty of OH radical concentrations has been estimated to be about 30 %. (*15*)

The ROOOH´s formation kinetics was assessed based on the measured ROOOH, RO_2 and OH radical concentrations (Fig. 4). From the linear dependence of [ROOOH] vs. $[RO_2] \times [OH]$ in the case of HO-C_5H_8OOOH, a rate coefficient k(HO-$C_5H_8O_2$+OH) = 5.1×10^{-11} cm^3 $molecule^{-1}$ s^{-1} follows. (*15*) For the higher oxidized HO-$C_5H_8(O_2)OOOH$, the analysis yields k(HO-$C_5H_8(O_2)O_2$+OH) = 1.1×10^{-10} cm^3 $molecule^{-1}$ s^{-1} assuming a regression line through zero (insert in Fig. 4). These rate coefficients have an

uncertainty of a factor of 3 - 4. Previously, high rate coefficients of RO_2 + OH reactions were reported for C_1 - C_4 RO_2 radicals via detection of the OH decay, e.g., $k(C_4H_9O_2+OH) = (1.5 \pm 0.3) \times 10^{-10}$ cm^3 $molecule^{-1}$ s^{-1} at 298 K (*24, 25*), supporting our findings.

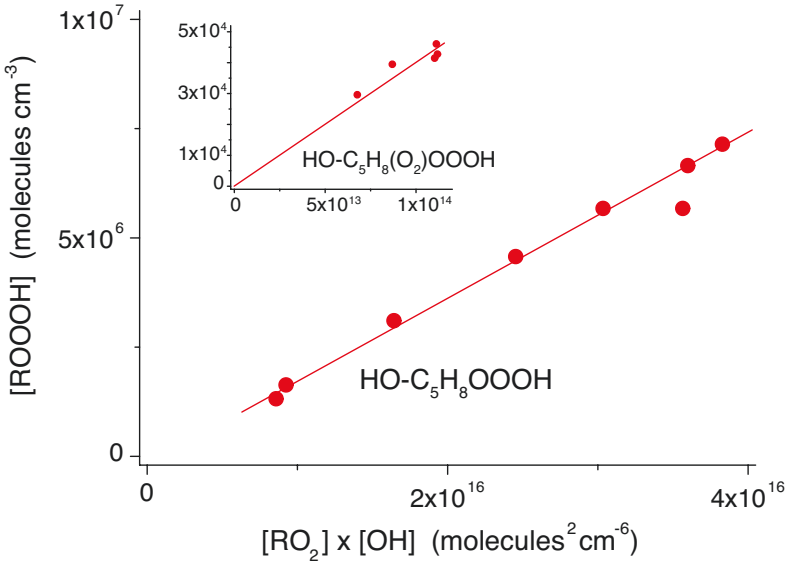

Fig. 4: Kinetic analysis of ROOOH formation in the OH + isoprene reaction. Data were taken from the experiments depicted in Fig. 3. Deduced rate coefficients of $HO\text{-}C_5H_8OOOH$ and $HO\text{-}C_5H_8(O_2)OOOH$ formation from the corresponding RO_2 + OH reactions were 5.1×10^{-11} and 1.1×10^{-10} cm^3 $molecule^{-1}$ s^{-1}, respectively. Error bars are not shown for clarity.

We tested the general validity of hydrotrioxide formation from RO_2 + OH reactions, especially for RO_2 radicals with atmospheric relevance. In the OH radical-initiated oxidation of dimethyl sulfide (DMS), α-pinene, toluene and 1-butene, the corresponding hydrotrioxide formation from the principal RO_2 radicals in the respective reaction system was clearly detectable in the flow experiment (Figs. S11 - S18). Data analysis revealed a linear dependence of signal(ROOOH) vs. signal(RO_2) × [OH] each (Figs. S19 - S22). In the cases where RO_2 radicals and ROOOH could be detected with close to maximum sensitivity, the rate coefficients $k(RO_2+OH)$ were estimated (Fig. S5 and Fig. S20), further supporting that RO_2 + OH reactions proceed with rate coefficients close to the collision limit. (*15*) Table 1 summarizes the rate coefficients determined in this study. Moreover, signals consistent with hydrotrioxide formation from the reaction of OH radicals with 2-methylpropene were observed in separate experiments conducted

in a 1 m^3 Teflon (FEP) chamber in air using CF_3O^- chemical ionization mass spectrometry (Fig. S23). (*15*) Consequently, it could be inferred that RO_2 + OH reactions represent a universal pathway of hydrotrioxide formation under atmospheric conditions.

Table 1: Rate coefficients k(RO_2+OH) derived from ROOOH formation, T = 295 ± 2 K.

RO_2 radical	k(RO_2 + OH) (cm^3 $molecule^{-1}$ s^{-1})
HO-$C_5H_8O_2$	5.1×10^{-11} [a]
HO-$C_5H_8(O_2)O_2$	1.1×10^{-10} [a]
HO-$C_{10}H_{16}(O_2)_2O_2$	1.8×10^{-10} [b]
$(HOOCH_2)_2NCH_2O_2$	3.2×10^{-10} [b,c,d] 2.6×10^{-10} [b,c,e]

[a] uncertainty of a factor of 3 - 4
[b] uncertainty of a factor of 5
[c] using modelled OH concentrations
[d] IPN dependent experiments, Fig. 1A
[e] NO dependent experiments, Fig. S4

The hydroxy hydrotrioxide formed in the OH + 2-methylpropene reaction, as observed in the environmental chamber experiment (Fig. S23), suggested an experimental ROOOH lifetime of about 20 min at 296 K including thermal gas-phase decomposition and losses on the chamber wall. (*15*) Thus, 20 min can be regarded as a lower bound of its thermal lifetime. Theoretical calculations on the thermal decomposition energies for several hydrotrioxides (Fig. 2) pointed to similar or longer thermal lifetimes. In addition, the calculations did not indicate any fast photolysis pathways for ROOOH. (*15*)

We estimated the atmospheric lifetime of hydrotrioxides against the OH reaction to be about 2 hours to a few days assuming [OH] = (5 - 20) × 10^5 molecules cm^{-3} and k(OH+ROOOH) = (1 - 7.5) × 10^{-11} cm^3 $molecule^{-1}$ s^{-1}, relevant for saturated and unsaturated hydrotrioxides assuming an OH reactivity similar to the corresponding hydroperoxides. (*26, 27*) Thus, hydrotrioxides, once formed, would be present in the atmosphere for minutes to hours before further processing. Theoretical calculations favored the formation of alkoxy radicals RO from the reaction of OH radicals with saturated ROOOH. In the isoprene system, however, OH + HO-C_5H_8OOOH mainly forms the dihydroxy epoxide IEPOX (*22*) and HO_2. (*15*) Global simulations with the chemistry climate model ECHAM-HAMMOZ (*28*) permitted an assessment of ROOOH production from the OH radical-initiated oxidation of isoprene (Figs. S24 and S25). We lumped all isoprene-derived RO_2 radicals ($RO_{2,isoprene}$) and calculated that up to 1 % of $RO_{2,isoprene}$ could

react with OH. Given the large emission of isoprene (*20*), an annual ROOOH production of up to about 10 million metric tons is calculated. Furthermore, the modeling revealed that isoprene-derived hydrotrioxides can reach atmospheric concentrations of around 10^7 molecules cm^{-3} (Fig. S24).

From the knowledge in preparative chemistry (1-4), we deduced that hydrotrioxides could act as oxidants. In the atmosphere, this reactivity could manifest itself in surface reactions after lung inhalation and reactions on and within aerosol particles forming $^1O_2$. Hydrotrioxides generated from highly oxidized RO_2 radicals represent HOMs (highly oxygenated organic molecules) (*29*) with a very large oxygen content, e.g., HO-$C_{10}H_{16}(O_2)_2$OOOH (Fig. S14). These ROOOH-HOMs would be relevant for atmospheric aerosol formation, and thus, for Earth´s radiation budget. (*30*) Here, further research is needed to ascertain the role of hydrotrioxides for health and the environment. We illustrated the direct observation of hydrotrioxides using mass spectrometry and this should open up opportunities to measure these compounds in different systems, including in the atmosphere following further optimization of the analytical techniques.

References and Notes:

1. F. E. Stary, D. E. Emge, R. W. Murray, Ozonization of organic substrates. Hydrotrioxide formation and decomposition to give singlet oxygen. *J. Am. Chem. Soc.* **98**, 1880-1884 (1976).
2. M. Zarth, A. De Meijere, Zum Mechanismus der Ozonolyse von C,H-Bindungen: SiO_2-Lösungsmitteleinfluß, H/D-Isotopieeffekt, Zwischenstufen. *Chem. Ber.* **118**, 2429-2449 (1985).
3. R. W. Murray, W. Lumma Jr, J. Lin, Singlet oxygen sources in ozone chemistry. Decomposition of oxygen-rich intermediates. *J. Am. Chem. Soc.* **92**, 3205-3207 (1970).
4. G. H. Posner, K. S. Webb, W. M. Nelson, T. Kishimoto, H. H. Seliger, A new oxidizing reagent: triethylsilyl hydrotrioxide. *J. Org. Chem.* **54**, 3252-3254 (1989).
5. J. F. Müller, Z. Liu, V. S. Nguyen, T. Stavrakou, J. N. Harvey, J. Peeters, The reaction of methyl peroxy and hydroxyl radicals as a major source of atmospheric methanol. *Nat. Commun.* **7**, 13213 (2016).
6. Y. Liu, L. Chen, D. Chen, W. Wang, F. Liu, W. Wang, Computational study on mechanisms of $C_2H_5O_2$ + OH reaction and properties of $C_2H_5O_3H$ complex. *Chem. Res. Chinese U.* **33**, 623-630 (2017).
7. E. Assaf, C. Schoemaecker, L. Vereecken, C. Fittschen, Experimental and theoretical investigation of the reaction of RO_2 radicals with OH radicals: Dependence of the HO_2 yield on the size of the alkyl group. *Int. J. Chem. Kinet.* **50**, 670-680 (2018).
8. C. Yan, L. N. Krasnoperov, Pressure-Dependent Kinetics of the Reaction between CH_3O_2 and OH: TRIOX Formation. *J. Phys. Chem. A* **123**, 8349-8357 (2019).
9. A. T. Archibald, A. S. Petit, C. J. Percival, J. N. Harvey, D. E. Shallcross, On the importance of the reaction between OH and RO_2 radicals. *Atmos. Sci. Lett.* **10**, 102-108 (2009).
10. T. Berndt, S. Richters, T. Jokinen, N. Hyttinen, T. Kurten, R. V. Otkjaer, H. G. Kjaergaard, F. Stratmann, H. Herrmann, M. Sipila, M. Kulmala, M. Ehn, Hydroxyl radical-induced formation of highly oxidized organic compounds. *Nat. Commun.* **7**, 13677 (2016).
11. T. Berndt, N. Hyttinen, H. Herrmann, A. Hansel, First oxidation products from the reaction of hydroxyl radicals with isoprene for pristine environmental conditions. *Commun. Chem.* **2**, 21 (2019).
12. K. H. Møller, T. Berndt, H. G. Kjaergaard, Atmospheric Autoxidation of Amines. *Environ. Sci. Technol.* **54**, 11087-11099 (2020).
13. E. Praske, R. V. Otkjær, J. D. Crounse, J. C. Hethcox, B. M. Stoltz, H. G. Kjaergaard, P. O. Wennberg, Atmospheric autoxidation is increasingly important in urban and suburban North America. *P. Natl. Acad. Sci. USA* **115**, 64-69 (2018).
14. K. H. Møller, K. H. Bates, H. G. Kjaergaard, The importance of peroxy radical hydrogen-shift reactions in atmospheric isoprene oxidation. *J. Phys. Chem. A* **123**, 920-932 (2019).
15. Materials and Methods.
16. J. D. Crounse, L. B. Nielsen, S. Jørgensen, H. G. Kjaergaard, P. O. Wennberg, Autoxidation of Organic Compounds in the Atmosphere. *J. Phys. Chem. Lett.* **4**, 3513-3520 (2013).
17. T. Berndt, K. H. Møller, H. Herrmann, H. G. Kjaergaard, Trimethylamine Outruns Terpenes and Aromatics in Atmospheric Autoxidation. *J. Phys. Chem. A* **125**, 4454-4466 (2021).
18. T. Berndt, W. Scholz, B. Mentler, L. Fischer, H. Herrmann, M. Kulmala, A. Hansel, Accretion Product Formation from Self- and Cross-Reactions of RO_2 Radicals in the Atmosphere. *Angew. Chem. Int. Ed. Engl.* **57**, 3820-3824 (2018).
19. M. P. Rissanen, T. Kurten, M. Sipila, J. A. Thornton, J. Kangasluoma, N. Sarnela, H. Junninen, S. Jørgensen, S. Schallhart, M. K. Kajos, R. Taipale, M. Springer, T. F. Mentel, T. Ruuskanen, T. Petaja, D. R. Worsnop, H. G. Kjaergaard, M. Ehn, The formation of highly oxidized multifunctional products in the ozonolysis of cyclohexene. *J. Am. Chem. Soc.* **136**, 15596-15606 (2014).

20. K. Sindelarova, C. Granier, I. Bouarar, A. Guenther, S. Tilmes, T. Stavrakou, J. F. Müller, U. Kuhn, P. Stefani, W. Knorr, Global data set of biogenic VOC emissions calculated by the MEGAN model over the last 30 years. *Atmos. Chem. Phys.* **14**, 9317-9341 (2014).
21. J. Peeters, T. L. Nguyen, L. Vereecken, HO_x radical regeneration in the oxidation of isoprene. *Phys. Chem. Chem. Phys.* **11**, 5935-5939 (2009).
22. P. O. Wennberg, K. H. Bates, J. D. Crounse, L. G. Dodson, R. C. McVay, L. A. Mertens, T. B. Nguyen, E. Praske, R. H. Schwantes, M. D. Smarte, J. M. St Clair, A. P. Teng, X. Zhang, J. H. Seinfeld, Gas-Phase Reactions of Isoprene and Its Major Oxidation Products. *Chem. Rev.* **118**, 3337-3390 (2018).
23. S. Wang, M. Riva, C. Yan, M. Ehn, L. Wang, Primary Formation of Highly Oxidized Multifunctional Products in the OH-Initiated Oxidation of Isoprene: A Combined Theoretical and Experimental Study. *Environ. Sci. Technol.* **52**, 12255-12264 (2018).
24. E. Assaf, S. Tanaka, Y. Kajii, C. Schoemaecker, C. Fittschen, Rate constants of the reaction of C_2–C_4 peroxy radicals with OH radicals. *Chem. Phys. Lett.* **684**, 245-249 (2017).
25. E. Assaf, B. Song, A. Tomas, C. Schoemaecker, C. Fittschen, Rate Constant of the Reaction between CH_3O_2 Radicals and OH Radicals Revisited. *J. Phys. Chem. A* **120**, 8923-8932 (2016).
26. J. M. St. Clair, J. C. Rivera-Rios, J. D. Crounse, H. C. Knap, K. H. Bates, A. P. Teng, S. Jørgensen, H. G. Kjaergaard, F. N. Keutsch, P. O. Wennberg, Kinetics and products of the reaction of the first-generation isoprene hydroxy hydroperoxide (ISOPOOH) with OH. *J. Phys. Chem. A* **120**, 1441-1451 (2016).
27. C. Fittschen, M. Al Ajami, S. Batut, V. Ferracci, S. Archer-Nicholls, A. T. Archibald, C. Schoemaecker, ROOOH: a missing piece of the puzzle for OH measurements in low-NO environments? *Atmos. Chem. Phys.* **19**, 349-362 (2019).
28. M. G. Schultz, S. Stadtler, S. Schröder, D. Taraborrelli, B. Franco, J. Krefting, A. Henrot, S. Ferrachat, U. Lohmann, D. Neubauer, C. Siegenthaler-Le Drian, S. Wahl, H. Kokkola, T. Kühn, S. Rast, H. Schmidt, P. Stier, D. Kinnison, G. S. Tyndall, J. J. Orlando, C. Wespes, The chemistry–climate model ECHAM6.3-HAM2.3-MOZ1.0. *Geosci. Model Dev.* **11**, 1695-1723 (2018).
29. F. Bianchi, T. Kurten, M. Riva, C. Mohr, M. P. Rissanen, P. Roldin, T. Berndt, J. D. Crounse, P. O. Wennberg, T. F. Mentel, J. Wildt, H. Junninen, T. Jokinen, M. Kulmala, D. R. Worsnop, J. A. Thornton, N. Donahue, H. G. Kjaergaard, M. Ehn, Highly Oxygenated Organic Molecules (HOM) from Gas-Phase Autoxidation Involving Peroxy Radicals: A Key Contributor to Atmospheric Aerosol. **119**, 3472-3509 (2019).
30. M. Kulmala, J. Kontkanen, H. Junninen, K. Lehtipalo, H. E. Manninen, T. Nieminen, T. Petaja, M. Sipila, S. Schobesberger, P. Rantala, A. Franchin, T. Jokinen, E. Jarvinen, M. Aijala, J. Kangasluoma, J. Hakala, P. P. Aalto, P. Paasonen, J. Mikkila, J. Vanhanen, J. Aalto, H. Hakola, U. Makkonen, T. Ruuskanen, R. L. Mauldin, 3rd, J. Duplissy, H. Vehkamaki, J. Back, A. Kortelainen, I. Riipinen, T. Kurten, M. V. Johnston, J. N. Smith, M. Ehn, T. F. Mentel, K. E. Lehtinen, A. Laaksonen, V. M. Kerminen, D. R. Worsnop, Direct observations of atmospheric aerosol nucleation. *Science* **339**, 943-946 (2013).
31. T. Berndt, R. Kaethner, J. Voigtlander, F. Stratmann, M. Pfeifle, P. Reichle, M. Sipila, M. Kulmala, M. Olzmann, Kinetics of the unimolecular reaction of CH_2OO and the bimolecular reactions with the water monomer, acetaldehyde and acetone under atmospheric conditions. *Phys. Chem. Chem. Phys.* **17**, 19862-19873 (2015).
32. J. D. Raff, B. J. Finlayson-Pitts, Hydroxyl radical quantum yields from isopropyl nitrite photolysis in air. *Environ. Sci. Technol.* **44**, 8150-8155 (2010).
33. W. Lindinger, A. Jordan, Proton-transfer-reaction mass spectrometry (PTR–MS): on-line monitoring of volatile organic compounds at pptv levels. *Chem. Soc. Rev.* **27**, 347-375 (1998).
34. F. L. Eisele, D. J. Tanner, Ion-assisted tropospheric OH measurements. *J. Geophys. Res.-Atmos.* **96**, 9295-9308 (1991).

35. M. Breitenlechner, L. Fischer, M. Hainer, M. Heinritzi, J. Curtius, A. Hansel, PTR3: An Instrument for Studying the Lifecycle of Reactive Organic Carbon in the Atmosphere. *Anal. Chem.* **89**, 5824-5831 (2017).
36. H. Junninen, M. Ehn, T. Petäjä, L. Luosujärvi, T. Kotiaho, R. Kostiainen, U. Rohner, M. Gonin, K. Fuhrer, M. Kulmala, D. R. Worsnop, A high-resolution mass spectrometer to measure atmospheric ion composition. *Atmos. Meas. Tech.* **3**, 1039-1053 (2010).
37. S. T. Arnold, R. A. Morris, A. A. Viggiano, J. T. Jayne, Ion chemistry relevant for chemical ionization detection of SO_3. *J. Geophys. Res.-Atmos.* **100**, 14141-14146 (1995).
38. T. Berndt, Peroxy Radical Processes and Product Formation in the OH Radical-Initiated Oxidation of alpha-Pinene for Near-Atmospheric Conditions. *J. Phys. Chem. A* **125**, 9151-9160 (2021).
39. M. A. Blitz, R. J. Salter, D. E. Heard, P. W. Seakins, An Experimental and Master Equation Study of the Kinetics of OH/OD + SO_2: The Limiting High-Pressure Rate Coefficients. *J. Phys. Chem. A* **121**, 3184-3191 (2017).
40. D. Aljawhary, A. K. Y. Lee, J. P. D. Abbatt, High-resolution chemical ionization mass spectrometry (ToF-CIMS): application to study SOA composition and processing. *Atmos. Meas. Tech.* **6**, 3211-3224 (2013).
41. S. Iyer, F. Lopez-Hilfiker, B. H. Lee, J. A. Thornton, T. Kurten, Modeling the Detection of Organic and Inorganic Compounds Using Iodide-Based Chemical Ionization. *J. Phys. Chem. A* **120**, 576-587 (2016).
42. R. Atkinson, D. L. Baulch, R. A. Cox, R. F. Hampson, J. A. Kerr, M. J. Rossi, J. Troe, Evaluated Kinetic, Photochemical and Heterogeneous Data for Atmospheric Chemistry: Supplement V. IUPAC Subcommittee on Gas Kinetic Data Evaluation for Atmospheric Chemistry. *J. Phys. Chem. Ref. Data* **26**, 521-1011 (1997).
43. R. Atkinson, D. L. Baulch, R. A. Cox, R. F. Hampson, J. A. Kerr, J. Troe, Evaluated Kinetic and Photochemical Data for Atmospheric Chemistry: Supplement IV. IUPAC Subcommittee on Gas Kinetic Data Evaluation for Atmospheric Chemistry. *J. Phys. Chem. Ref. Data* **21**, 1125-1568 (1992).
44. R. Atkinson, R. A. Perry, J. N. Pitts, Rate constants for the reactions of the OH radical with $(CH_3)_2NH$, $(CH_3)_3N$, and $C_2H_5NH_2$ over the temperature range 298–426 °K. *J. Chem. Phys.* **68**, 1850-1853 (1978).
45. B. Bohn, C. Zetzsch, Formation of HO_2 from OH and C_2H_2 in the presence of O_2. *J. Chem. Soc. Faraday Trans.* **94**, 1203-1210 (1998).
46. I. Barnes, J. Hjorth, N. Mihalopoulos, Dimethyl sulfide and dimethyl sulfoxide and their oxidation in the atmosphere. *Chem. Rev.* **106**, 940-975 (2006).
47. R. Wu, S. Wang, L. Wang, New mechanism for the atmospheric oxidation of dimethyl sulfide. The importance of intramolecular hydrogen shift in a CH(3)SCH(2)OO radical. *J. Phys. Chem. A* **119**, 112-117 (2015).
48. T. Berndt, W. Scholz, B. Mentler, L. Fischer, E. H. Hoffmann, A. Tilgner, N. Hyttinen, N. L. Prisle, A. Hansel, H. Herrmann, Fast Peroxy Radical Isomerization and OH Recycling in the Reaction of OH Radicals with Dimethyl Sulfide. *J. Phys. Chem. Lett.* **10**, 6478-6483 (2019).
49. S. Wang, R. Wu, T. Berndt, M. Ehn, L. Wang, Formation of Highly Oxidized Radicals and Multifunctional Products from the Atmospheric Oxidation of Alkylbenzenes. *Environ. Sci. Technol.* **51**, 8442-8449 (2017).
50. J. D. Crounse, K. A. McKinney, A. J. Kwan, P. O. Wennberg, Measurement of gas-phase hydroperoxides by chemical ionization mass spectrometry. *Anal. Chem.* **78**, 6726-6732 (2006).
51. J. Cerkovnik, E. Eržen, J. Koller, B. Plesničar, Evidence for HOOO Radicals in the Formation of Alkyl Hydrotrioxides (ROOOH) and Hydrogen Trioxide (HOOOH) in the Ozonation of C−H Bonds in Hydrocarbons[1]. *J. Am. Chem. Soc.* **124**, 404-409 (2002).
52. A. Abdrakhmanova, L. Khalitova, L. Spirikhin, V. Dokichev, S. Grabovskiy, N. Kabal'nova, Synthesis and thermal decomposition of hydrotrioxide obtained by ozonization of exo-bicyclo [2.2. 1] heptan-2-ol. *Russ. Chem. Bull.* **56**, 271-275 (2007).

53. M. Giorgetta, J. Jungclaus, C. Reick, S. Legutke, V. Brovkin, T. Crueger, M. Esch, K. Fieg, K. Glushak, V. Gayler, CMIP5 simulations of the Max Planck Institute for Meteorology (MPI-M) based on the MPI-ESM-LR model: The rcp85 experiment, served by ESGF. *World Data Cent. Clim.* **10**, 1594 (2012).
54. J. F. Lamarque, T. C. Bond, V. Eyring, C. Granier, A. Heil, Z. Klimont, D. Lee, C. Liousse, A. Mieville, B. Owen, M. G. Schultz, D. Shindell, S. J. Smith, E. Stehfest, J. Van Aardenne, O. R. Cooper, M. Kainuma, N. Mahowald, J. R. McConnell, V. Naik, K. Riahi, D. P. van Vuuren, Historical (1850–2000) gridded anthropogenic and biomass burning emissions of reactive gases and aerosols: methodology and application. *Atmos. Chem. Phys.* **10**, 7017-7039 (2010).
55. A. B. Guenther, X. Jiang, C. L. Heald, T. Sakulyanontvittaya, T. Duhl, L. K. Emmons, X. Wang, The Model of Emissions of Gases and Aerosols from Nature version 2.1 (MEGAN2.1): an extended and updated framework for modeling biogenic emissions. *Geosci. Model Dev.* **5**, 1471-1492 (2012).
56. J. D. Crounse, F. Paulot, H. G. Kjaergaard, P. O. Wennberg, Peroxy radical isomerization in the oxidation of isoprene. *Phys. Chem. Chem. Phys.* **13**, 13607-13613 (2011).
57. S. Stadtler, T. Kühn, S. Schröder, D. Taraborrelli, M. G. Schultz, H. Kokkola, Isoprene-derived secondary organic aerosol in the global aerosol–chemistry–climate model ECHAM6.3.0–HAM2.3–MOZ1.0. *Geosci. Model Dev.* **11**, 3235-3260 (2018).
58. S. Madronich, S. Flocke, in *Solar Ultraviolet Radiation,* C. S. Zerefos, A. F. Bais, Eds. (Springer Berlin Heidelberg, Berlin, Heidelberg, 1997), pp. 23-48.
59. S. M. Saunders, M. E. Jenkin, R. G. Derwent, M. J. Pilling, Protocol for the development of the Master Chemical Mechanism, MCM v3 (Part A): tropospheric degradation of non-aromatic volatile organic compounds. *Atmos. Chem. Phys.* **3**, 161-180 (2003).
60. D. Kinnison, G. P. Brasseur, S. Walters, R. Garcia, D. Marsh, F. Sassi, V. Harvey, C. Randall, L. Emmons, J. Lamarque, Sensitivity of chemical tracers to meteorological parameters in the MOZART‐3 chemical transport model. *J. Geophys. Res.-Atmos.* **112**, D20302 (2007).
61. Y. Zhao, M. Saunois, P. Bousquet, X. Lin, A. Berchet, M. I. Hegglin, J. G. Canadell, R. B. Jackson, D. A. Hauglustaine, S. Szopa, A. R. Stavert, N. L. Abraham, A. T. Archibald, S. Bekki, M. Deushi, P. Jöckel, B. Josse, D. Kinnison, O. Kirner, V. Marécal, F. M. O'Connor, D. A. Plummer, L. E. Revell, E. Rozanov, A. Stenke, S. Strode, S. Tilmes, E. J. Dlugokencky, B. Zheng, Inter-model comparison of global hydroxyl radical (OH) distributions and their impact on atmospheric methane over the 2000–2016 period. *Atmos. Chem. Phys.* **19**, 13701-13723 (2019).
62. D. Jeong, R. Seco, L. Emmons, R. Schwantes, Y. Liu, K. A. McKinney, S. T. Martin, F. N. Keutsch, D. Gu, A. B. Guenther, O. Vega, J. Tota, R. A. F. Souza, S. R. Springston, T. B. Watson, S. Kim, Reconciling Observed and Predicted Tropical Rainforest OH Concentrations. *J. Geophys. Res.-Atmos.* **127**, 1-18 (2022).
63. A. P. Teng, J. D. Crounse, P. O. Wennberg, Isoprene peroxy radical dynamics. *J. Am. Chem. Soc.* **139**, 5367-5377 (2017).
64. J. Peeters, T. L. Nguyen, Unusually fast 1,6-H shifts of enolic hydrogens in peroxy radicals: formation of the first-generation C_2 and C_3 carbonyls in the oxidation of isoprene. *J. Phys. Chem. A* **116**, 6134-6141 (2012).
65. Y. Duan, M. Monge-Palacios, E. Grajales-Gonzalez, D. Han, K. H. Møller, H. G. Kjaergaard, S. M. Sarathy, Oxidation kinetics of n-pentanol: A theoretical study of the reactivity of the 1-hydroxy-1-peroxypentyl radical. *Combust. Flame* **219**, 20-32 (2020).
66. P. Morajkar, C. Schoemaecker, M. Okumura, C. Fittschen, Direct measurement of the equilibrium constants of the reaction of formaldehyde and acetaldehyde with HO_2 radicals. *Int. J. Chem. Kinet.* **46**, 245-259 (2014).
67. K. H. Møller, R. V. Otkjær, J. Chen, H. G. Kjaergaard, Double bonds are key to fast unimolecular reactivity in first-generation monoterpene hydroxy peroxy radicals. *J. Phys. Chem. A* **124**, 2885-2896 (2020).

68. L. Xu, K. H. Møller, J. D. Crounse, R. V. Otkjær, H. G. Kjaergaard, P. O. Wennberg, Unimolecular reactions of peroxy radicals formed in the oxidation of α-pinene and β-pinene by hydroxyl radicals. *J. Phys. Chem. A* **123**, 1661-1674 (2019).
69. Q. Ye, M. B. Goss, G. Isaacman-VanWertz, A. Zaytsev, P. Massoli, C. Lim, P. Croteau, M. Canagaratna, D. A. Knopf, F. N. Keutsch, C. L. Heald, J. H. Kroll, Organic Sulfur Products and Peroxy Radical Isomerization in the OH Oxidation of Dimethyl Sulfide. *ACS Earth Space Chem.* **5**, 2013-2020 (2021).
70. K. H. Møller, E. Praske, L. Xu, J. D. Crounse, P. O. Wennberg, H. G. Kjaergaard, Stereoselectivity in Atmospheric Autoxidation. *J. Phys. Chem. Lett.* **10**, 6260-6266 (2019).
71. K. H. Møller, R. V. Otkjær, N. Hyttinen, T. Kurtén, H. G. Kjaergaard, Cost-effective implementation of multiconformer transition state theory for peroxy radical hydrogen shift reactions. *J. Phys. Chem. A* **120**, 10072-10087 (2016).
72. F. Saad, D. Cella, E. Basch, B. A. Hadaschik, P. N. Mainwaring, S. Oudard, J. N. Graff, K. McQuarrie, S. Li, S. Hudgens, J. Lawson, A. Lopez-Gitlitz, M. K. Yu, M. R. Smith, E. J. Small, Spartan 18; Wavefunction Inc. Irvine; CA. *Lancet Oncol.* **19**, 1404-1416 (2018).
73. T. A. Halgren, Merck molecular force field. I. Basis, form, scope, parameterization, and performance of MMFF94. *J. Comput. Chem.* **17**, 490-519 (1996).
74. M. Frisch, G. Trucks, H. Schlegel, G. Scuseria, M. Robb, J. Cheeseman, G. Scalmani, V. Barone, G. Petersson, H. Nakatsuji. (Gaussian, Inc. Wallingford, CT, 2016).
75. A. D. Dutoi, Y. Jung, M. Head-Gordon, An orbital-based definition of radical and multiradical character. *J. Phys. Chem. A* **108**, 10270-10279 (2004).
76. P. G. Szalay, T. Muller, G. Gidofalvi, H. Lischka, R. Shepard, Multiconfiguration self-consistent field and multireference configuration interaction methods and applications. *Chem. Rev.* **112**, 108-181 (2012).
77. H. J. Werner, P. J. Knowles, An efficient internally contracted multiconfiguration–reference configuration interaction method. *J. Chem. Phys.* **89**, 5803-5814 (1988).
78. P. Celani, H.-J. Werner, Analytical energy gradients for internally contracted second-order multireference perturbation theory. *J. Chem. Phys.* **119**, 5044-5057 (2003).
79. H.-J. Werner, P. J. Knowles, F. R. Manby, J. A. Black, K. Doll, A. Heßelmann, D. Kats, A. Köhn, T. Korona, D. A. Kreplin, The Molpro quantum chemistry package. *J. Chem. Phys.* **152**, 144107(144101-144124) (2020).
80. V. Vaida, H. Kjaergaard, P. Hintze, D. Donaldson, Photolysis of sulfuric acid vapor by visible solar radiation. *Science* **299**, 1566-1568 (2003).
81. P. E. Hintze, H. G. Kjaergaard, V. Vaida, J. B. Burkholder, Vibrational and electronic spectroscopy of sulfuric acid vapor. *J. Phys. Chem. A* **107**, 1112-1118 (2003).
82. C. M. Roehl, S. A. Nizkorodov, H. Zhang, G. A. Blake, P. O. Wennberg, Photodissociation of peroxynitric acid in the near-IR. *J. Phys. Chem. A* **106**, 3766-3772 (2002).
83. K. Mackeprang, H. G. Kjaergaard, Vibrational transitions in hydrogen bonded bimolecular complexes–A local mode perturbation theory approach to transition frequencies and intensities. *J. Mol. Spectrosc.* **334**, 1-9 (2017).
84. J. Wallberg, H. G. Kjaergaard, Absolute fundamental and overtone OH and OD stretching intensities of alcohols. *Spectrochim. Acta A Mol. Biomol. Spectrosc.* **208**, 315-324 (2019).
85. K. H. Møller, T. Kurten, K. H. Bates, J. A. Thornton, H. G. Kjaergaard, Thermalized Epoxide Formation in the Atmosphere. *J. Phys. Chem. A* **123**, 10620-10630 (2019).
86. J. M. Anglada, A. Sole, Tropospheric oxidation of methyl hydrotrioxide (CH_3OOOH) by hydroxyl radical. *Phys. Chem. Chem. Phys.* **20**, 27406-27417 (2018).
87. R. L. Caravan, M. A. H. Khan, J. Zador, L. Sheps, I. O. Antonov, B. Rotavera, K. Ramasesha, K. Au, M. W. Chen, D. Rosch, D. L. Osborn, C. Fittschen, C. Schoemaecker, M. Duncianu, A. Grira, S. Dusanter, A. Tomas, C. J. Percival, D. E. Shallcross, C. A. Taatjes, The reaction of hydroxyl and methylperoxy radicals is not a major source of atmospheric methanol. *Nat. Commun.* **9**, 4343 (2018).

Acknowledgments:

The author thanks A. Rohmer and K. Pielok for technical assistance and the tofTools team for providing the data analysis tools. This work used resources of the Deutsches Klimarechenzentrum (DKRZ) granted by its Scientific Steering Committee (WLA) under project ID bb1128.

Funding:

HGK: Independent Research Fund Denmark (9040-00142B).

HGK: High Performance Computing Center at the University of Copenhagen.

EHH and HH: German Research Foundation (Project ORIGAMY, number: 447349939)

POW and JDC: US National Science Fund for financial support (CHE-1905340).

POW and HGK: The Alfred P. Sloan Foundation under Award No. G-2019-12281.

Author contributions:

Conceptualization: TB, HGK

Methodology: All authors

Experiments: TB, JDC

Calculations: JC, ERK, KHM, HGK

Global modeling: AT, EHH, HH, POW

Writing – original draft: TB, HGK

Writing – review & editing: All authors

Competing interests: Authors declare that they have no competing interests.

Data and materials availability: All theoretical calculation output files are available online via the public research data archive of the University of Copenhagen: https://doi.org/10.17894/ucph.99bf9f39-ec48-4afe-b426-cf6ef0d3ea70. All ECHAM-HAMMOZ model output files are available online via the public research data archive Zenodo: https://doi.org/10.5281/zenodo.6373045. All other data are available in the main text or the supplementary materials.

Supplementary Materials

Materials and Methods

Supplementary Text

Figs. S1 to S47

Tables S1 to S9

References (31-87)

Supplementary Materials

for

Hydrotrioxide (ROOOH) formation in the atmosphere

Torsten Berndt,[1*] Jing Chen,[2] Eva R. Kjærgaard,[2] Kristian H. Møller,[2] Andreas Tilgner,[1] Erik H. Hoffmann,[1] Hartmut Herrmann,[1] John D. Crounse,[3] Paul O. Wennberg,[3,4] Henrik G. Kjaergaard[2*]

[1] Atmospheric Chemistry Department (ACD), Leibniz Institute for Tropospheric Research (TROPOS), Permoserstraße 15, 04318 Leipzig, Germany.

[2] Department of Chemistry, University of Copenhagen, Universitetsparken 5, DK-2100 Ø, Denmark.

[3] Division of Geological and Planetary Sciences, California Institute of Technology, Pasadena, California 91125, United States.

[4] Division of Engineering and Applied Science, California Institute of Technology, Pasadena, California 91125, United States.

Email:

Torsten Berndt: berndt@tropos.de

Henrik G. Kjaergaard: hgk@chem.ku.dk

Contents

S1. Experimental information

S1.1. TROPOS experimental setup

The experiments have been performed in a free-jet flow system at a pressure of 1 bar purified air, a temperature of 295 ± 2 K and a relative humidity of < 0.1 %. (*11, 31*) The relative humidity was increased up to 21 % in one example in order to examine the effect of water vapor on the product formation. This setup allows the investigation of oxidation reactions for atmospheric conditions in absence of wall effects.

The free-jet flow system consists of an outer tube (length: 200 cm, inner diameter: 15 cm) and a moveable inner tube (outer diameter: 9.5 mm) equipped with a nozzle. The OH radical precursor isopropyl nitrite (IPN) premixed with the carrier gas (5 L min^{-1} STP) is injected through the inner tube into the main gas stream (95 L min^{-1} STP), which contains the organic reactant (trimethylamine, isoprene, DMS, α-pinene, toluene or 1-butene). Large differences of the gas velocities at the nozzle outflow (nozzle: 15.9 m s^{-1}; main flow: 0.13 m s^{-1}) and the nozzle geometry ensure rapid reactant mixing downstream of the nozzle. Diffusion processes at 1 bar air are too slow to transport a significant fraction of the reaction products out of the center flow toward the walls within the time range of this experiment of 7.5 s.

IPN photolysis (*32*) for continuous OH radical production in the flow system was carried out downstream the mixing point of the reactant streams by means of 8 NARVA 36W Blacklight Blue lamps emitting in the range from 350 – 400 nm. The photolysis of IPN produces NO and i-C_3H_7O radicals, which rapidly form acetone and HO_2 radicals in the reaction with O_2. OH radical generation in the flow system eventually proceeds via $HO_2 + NO \rightarrow OH + NO_2$. NO addition of (5.0 - 50) × 10^9 molecules cm^{-3} enhanced the OH radical production. The residence time in the irradiated reaction zone was experimentally determined using a “chemical clock”. (*31*)

The concentrations of the organic reactants were followed by means of a proton transfer reaction mass spectrometer (Ionicon, PTR-MS 500). (*33*)

All gas flows were set by means of calibrated gas flow controllers (MKS 1259/1179). The organic reactants and gases had the following purity: trimethylamine (≥99.5 %, Aldrich), isoprene (>99 %, Aldrich), DMS (>99 %, Sigma-Aldrich), α-pinene (99.5 %, Fluka), toluene (99.8 %, Aldrich), 1-butene (99 %, Messer) and NO (498 ± 10 ppmV NO (99.5 %) in N_2 (99.999 %), Air Liquide). Air was taken from a commercial PSA (Pressure Swing Adsorption) unit with further purification by a series of absorber units filled with activated charcoal, 4 Å and 10 Å molecular sieves.

S1.2. Product analysis by mass spectrometry

The detection of RO_2 radicals and closed-shell products was performed by means of a CI-APi-TOF (chemical ionization – atmospheric pressure interface – time-of-flight) mass spectrometer (Tofwerk AG, Airmodus) with a resolving power > 3000 Th/Th sampling from the center flow of the free-jet flow system with a sampling rate of 10 L min^{-1} (STP). The ion-molecule reaction (IMR) took place at atmospheric pressure using a Boulder-type inlet. (*34*) As reagent ions served iodide (I^-) and nitrate (NO_3^-).

In the case of ionization by I^-, tert-C_4H_9I was added to a 35 L min^{-1} (STP) flow of purified N_2 with a concentration of ~5 × 10^{11} molecules cm^{-3} producing the charger ions after ionization with a ^{241}Am source. In the case of ionization by nitrate (NO_3^-), a 0.5 ml nitric acid-containing vial was connected to the 35 L min^{-1} (STP) sheath flow without overflowing the nitric acid sample. HNO_3 diffusion from the vial into the N_2 flow was sufficient to form the reagent ions $(HNO_3)_xNO_3^-$, x = 0, 1, 2, ions with the needed signal strength after ionization by the ^{241}Am source. The ions from the sheath flow are guided into the sample flow by an electric field without mixing of both gas streams.

RO_2 radicals and closed-shell products were detected as a cluster with the respective reagent ions, i.e., $(product)I^-$ or $(product)NO_3^-$. Stated normalized product signals were determined according to equation (SIa) or (SIb) using either iodide (I^-) or nitrate (NO_3^-), respectively:

$$\text{Normalized signal} = \frac{[(\text{product})\text{I}^-]}{[\text{I}^-]} \quad \text{(SIa)}$$

$$\text{Normalized signal} = \frac{[(\text{product})\text{NO}_3^-]}{[\text{NO}_3^-] + [(\text{HNO}_3)\text{NO}_3^-] + [(\text{HNO}_3)_2\text{NO}_3^-]} \quad \text{(SIb)}$$

The quantities in equations (SIa) and (SIb), i.e. $[(product)I^-]$ etc., are the measured signal intensities. Duty cycle correction is applied in order to compensate for the mass-dependent transmission of the mass spectrometer, i.e. the normalized product signals were corrected with respect to I^- at nominal 127 Th or with respect to NO_3^- at nominal 62 Th depending on the ionization scheme used. (*35, 36*) If not otherwise specified, stated measurement results were obtained from 10 min data accumulation. Statistical uncertainty of signal intensities was less than 20 %, in most cases less than 10 %.

The detection of SO_3 was carried out by means of nitrate ionization monitoring the signals of $(SO_3)NO_3^-$ and SO_4^-. (*37*) SO_3 concentrations were calculated according to equations (SIIa) and (SIIb) for both measured signals.

$$[\text{SO}_3] = \text{f}_{(\text{SO}_3)\text{NO}_3^-} \frac{[(\text{SO}_3)\text{NO}_3^-]}{[\text{NO}_3^-] + [(\text{HNO}_3)\text{NO}_3^-] + [(\text{HNO}_3)_2\text{NO}_3^-]} \quad \text{(SIIa)}$$

$$[SO_3] = f_{SO_4^-} \frac{[SO_4^-]}{[NO_3^-] + [(HNO_3)NO_3^-] + [(HNO_3)_2NO_3^-]} \quad \text{(SIIb)}$$

The needed calibration factors $f_{(SO_3)NO_3^-}$ and $f_{SO_4^-}$ were experimentally determined as described in the previous work. (*38*) Also here, measured data were obtained from 10 min data accumulation.

S1.3. Product concentrations in the OH + isoprene reaction

Lower limit calibration factors with an expected uncertainty by a factor of 2 have been used in a previous study on OH + isoprene from our laboratory to determine lower limit product concentrations (also affected with an uncertainty by a factor of 2). (*11*) A suite of reagent ions was applied, i.e., hydrazinium ($H_2NNH_3^+$), methylaminuim ($CH_3NH_3^+$), ethylaminium ($C_2H_5NH_3^+$), n-propylaminium ($n\text{-}C_3H_7NH_3^+$), acetate (CH_3COO^-) and iodide (I^-), measuring the product formation in each case for identical reaction conditions. Comparison of the results, supported by theoretical calculations on the cluster stability of "(product)reagent-ion", allowed us to conclude that products of the OH + isoprene reaction bearing at least 2 OH or OOH groups are detectable with close to maximum sensitivity (in most cases) using either hydrazinium or methylaminuim, i.e., the lower limit concentrations should be close to the "real" concentration. (*11*) The comparison for the different reagent ions allows an estimate of calibration factors for product measurements by iodide in the OH + isoprene reaction, as carried out in this study.

$\underline{HO\text{-}C_5H_8O_2}$: While hydrazinium showed the best sensitivity for the initially formed RO_2 radicals (for all isomers in total), their concentrations were distinctly underestimated by all reagent ions applied. The calibration factor $f(I^-, HO\text{-}C_5H_8O_2)$ is accessible by comparing the measurements with modelling results of $HO\text{-}C_5H_8O_2$ concentrations, see Fig. 4a and Fig.S8 in reference (*11*), leading to $f(I^-, HO\text{-}C_5H_8O_2) = 1.5 \times 10^{12}$ molecules cm^{-3} with an uncertainty of a factor of 2.

$\underline{HO\text{-}C_5H_8(O_2)O_2}$: Ionization by iodide showed almost identical results as observed by hydrazinium, see Fig. 4b in reference (*11*). This RO_2 radical is bearing an OH and an OOH group, and ionization by hydrazinium should be very efficient with close to maximum sensitivity. Thus, the lower limit calibration factor can be used, $f(I^-, HO\text{-}C_5H_8(O_2)O_2) = 1.85 \times 10^9$ molecules cm^{-3} with an uncertainty of a factor of 2.

$\underline{HO\text{-}C_5H_8(O_2)_2O_2}$: This RO_2 radical has most likely one additional OOH group compared to $HO\text{-}C_5H_8(O_2)O_2$ and should be as detectable as the $HO\text{-}C_5H_8(O_2)O_2$ radical, see also Fig. S3 in reference (*11*). Consequently, also $f(I^-, HO\text{-}C_5H_8(O_2)_2O_2) = 1.85 \times 10^9$ molecules cm^{-3} with an uncertainty of a factor of 2 can be expected.

$\underline{HO\text{-}C_5H_8OOOH}$: Here we used the findings for the signal of the hydroxy hydroperoxide, $HO\text{-}C_5H_8OOH$, assuming a similar behavior of OOH and OOOH groups in the binding with the reagent ions. Ionization by iodide was about a factor of 3.5 less efficient than ionization by hydrazinium, see Fig. S6 in reference (*11*). Assuming again close to maximum sensitivity using hydrazinium ionization, $f(I^-, HO\text{-}C_5H_8OOOH) = 6.5 \times 10^9$ molecules cm^{-3} follows with an uncertainty of a factor of 2.

$\underline{HO\text{-}C_5H_8(O_2)OOOH}$: This hydrotrioxide has most likely an OOH group more than $HO\text{-}C_5H_8OOOH$ and should be detectable with close to maximum sensitivity also by iodide, i.e., $f(I^-, HO\text{-}C_5H_8(O_2)OOOH) = 1.85 \times 10^9$ molecules cm^{-3} with an uncertainty of a factor of 2.

The product concentrations [product] can be calculated from the normalized product signals, equation (SIa), multiplied by the estimated calibration factor via equation (SIII).

$$[\text{Product}] = f(I^-, \text{product}) \frac{[(\text{product})I^-]}{[I^-]} \quad \text{(SIII)}$$

S1.4. Kinetic analysis

<u>OH radical concentration measured by SO_3 formation:</u>

The amount of formed SO_3 from the OH + SO_2 reaction is described by

$$[SO_3]_t = k_{OH+SO_2} \times [OH] \times [SO_2]_0 \times t \quad \text{(SIV)}$$

based on the rate law

$$\frac{d[SO_3]}{dt} = k_{OH+SO_2} \times [OH] \times [SO_2] \quad \text{(SV)}$$

assuming time-independent concentrations of OH radicals and SO_2. This assumption is justified for SO_2 because its conversion is clearly smaller than 0.001 in each case and the initial concentration $[SO_2]_0$ can be applied in the equations. For OH, it means that we have to assume an average (time-independent) OH concentration, $[OH]^{av}$, for the whole reaction time t (7.5 s).

$[OH]^{av}$ follows from the experimentally obtained amount of formed SO_3, $[SO_3]_t$, based on equation (SIV):

$$[OH]^{av} = \frac{[SO_3]_t}{(k_{OH+SO_2} \times [SO_2]_0 \times t)} \quad \text{(SVI)}$$

The rate coefficient $k_{OH+SO2} = 5.8 \times 10^{-13}$ cm^3 $molecule^{-1}$ s^{-1} determined for 1 bar N_2 at 298 K was taken from the literature (*39*) and an uncertainty of 20 % in k_{OH+SO2} is assumed. The resulting uncertainty (Gauß´s propagation of uncertainty) in $[OH]^{av}$ is calculated to be about 30 % considering the uncertainty in k_{OH+SO2} and the uncertainty of the SO_3 calibration of 20 %. (*38*)

Rate coefficient of ROOOH formation in the OH + isoprene reaction:

The rate law of ROOOH formation is given by:

$$\frac{d[ROOOH]}{dt} = k_{RO_2+OH} \times [OH] \times [RO_2] \quad \text{(SVII)}$$

Experiments in the free-jet flow system confirmed the linear rise of RO_2 radical concentrations with time, for HO-$C_5H_8O_2$ and HO-$C_5H_8(O_2)O_2$ radicals see Fig. 3 in reference (*11*). Thus, the RO_2 concentrations can be written as follows:

$$[RO_2] = f(t) = a \times t, \; a = \text{constant} \quad \text{(SVIII)}$$

The differential equation (SVII) can be given in the following way:

$$\frac{d[ROOOH]}{dt} = k_{RO_2+OH} \times [OH] \times a \times t \quad \text{(SIX)}$$

Integration of equation (SIX) using the time-independent OH concentration, $[OH]^{av}$, leads to:

$$[ROOOH]_t = k_{RO2+OH} \times [OH]^{av} \times a \times \frac{t^2}{2} \quad \text{(SX)}$$

The value "a" from equation (SVIII) is the slope of $[RO_2]$ vs. t and is given by the measured RO_2 radical concentration at the specific time t, i.e., $a = [RO_2]_t / t$.

$$[ROOOH]_t = 0.5 \times k_{RO_2+OH} \times [OH]^{av} \times [RO_2]_t \times t \quad \text{(SXI)}$$

The slope of $[ROOOH]_t$ vs. $[OH]^{av} \times [RO_2]_t$ yields the rate coefficient k_{RO2+OH} multiplied with 0.5 × t, t = 7.5 s in all experiments, where the concentrations of ROOOH and RO_2 have been measured. The concentrations of the hydrotrioxides and RO_2 radicals are affected with an expected uncertainty by a factor of 2 ($^{+100}_{-50}$ %), while

for OH radicals an uncertainty of about 30 % has been estimated. The resulting uncertainty in k_{RO2+OH} is $^{+144}_{-76}$ % according to Gauß´s propagation of uncertainty.

Rate coefficient of ROOOH formation in the reactions OH + trimethylamine and OH + α-pinene:

The needed calibration factors $f(I^-, RO_2)$ and $f(I^-, ROOOH)$ are not available for these reaction systems. However, close to maximum detection sensitivity can be assumed for the highly oxidized RO_2 radicals $(HOOCH_2)_2NCH_2O_2$, $HO\text{-}C_{10}H_{16}(O_2)_2O_2$ and the corresponding hydrotrioxides due to their high degree of functionalization (especially -OH, -OOH and -OOOH groups) as well as their large polarizability. (*40, 41*) Thus, setting $f(I^-, RO_2) \sim f(I^-, ROOOH)$, equation (SXI) can be written using the measured normalized signals:

$$\text{signal}(\text{ROOOH})_t = 0.5 \times k_{RO_2+OH} \times [OH]^{av} \times \text{signal}(RO_2)_t \times t \qquad \text{(SXII)}$$

OH radical measurements, $[OH]^{av}$, were not possible in the OH + trimethylamine system. Here, modelled average OH concentrations, $[OH]_{model}$, were used instead of $[OH]^{av}$. An uncertainty of a factor of 2 in $[OH]_{model}$ is estimated. The overall uncertainty in k_{RO2+OH} based on data analysis via equation (SXII) depends on the accuracy of $f(I^-, RO_2) \sim f(I^-, ROOOH)$. We assume an uncertainty in k_{RO2+OH} being not higher than a factor of 5 in the case of these highly oxidized RO_2 radicals.

S1.5. Reaction mechanism OH + trimethylamine

Table S1: Reaction mechanism used for modeling of OH radical concentrations in the OH + TMA reaction. Rate coefficients at ~295 K were taken from the literature. (*12, 17, 42-45*)

reaction	rate coefficient (cm^3 $molecule^{-1}$ s^{-1} or s^{-1})
IPN $(+O_2) \rightarrow NO + HO_2 +$ acetone	0.0016 this study
$NO + HO_2 \rightarrow OH + NO_2$	8.9×10^{-12}, (*43*)
$OH + HO_2 \rightarrow H_2O + O_2$	1.1×10^{-10}, (*43*)
$HO_2 + HO_2 \rightarrow H_2O_2 + O_2$	1.65×10^{-12}, (*43*)
$OH + NO \rightarrow HNO_2$	1.0×10^{-11}, (*43*)
$OH + NO_2 \rightarrow HNO_3$	1.2×10^{-11}, (*43*)
$O_3 + NO \rightarrow NO_2 + O_2$	1.8×10^{-14}, (*43*)
$O_3 + NO_2 \rightarrow NO_3 + O_2$	3.5×10^{-17}, (*43*)
$O_3 + HO_2 \rightarrow OH + 2\times O_2$	2.0×10^{-15}, (*43*)
$OH + TMA (+ O_2) \rightarrow (CH_3)_2NCH_2O_2 + H_2O$	6.1×10^{-11}, (*44*)
$(CH_3)_2NCH_2O_2 (+ O_2) \rightarrow (HOOCH_2)(CH_3)NCH_2O_2$	2.3 (*17*)
$(HOOCH_2)(CH_3)NCH_2O_2 \rightarrow (HOOCH_2)(CH_3)NCHO + OH$	0.088 (*17*)
$(HOOCH_2)(CH_3)NCH_2O_2 (+ O_2) \rightarrow (HOOCH_2)_2NCH_2O_2$	0.42 (*17*)
$(HOOCH_2)_2NCH_2O_2 \rightarrow (HOOCH_2)_2NCHO + OH$	0.041 (*17*)
$CH_3C(O)CH_2O_2 + NO \rightarrow 0.93\times NO_2 + 0.93\times HO_2 +$ products	8.8×10^{-12}, (*12*)
$HO\text{-}TMEO_2 + NO \rightarrow 0.9\times NO_2 + 0.9\times HO_2 +$ products	8.8×10^{-12}, (*12*)
$(CH_3)_2NCH_2O_2 + NO \rightarrow 0.93\times(CH_3)_2NCH_2O + 0.93\times NO_2 + 0.07\times(CH_3)_2NCH_2ONO_2$	8.8×10^{-12}, (*12*)
$(HOOCH_2)(CH_3)NCH_2O_2 + NO \rightarrow 0.93\times(HOOCH_2)(CH_3)NCH_2O + 0.93\times NO_2 + 0.07\times(HOOCH_2)(CH_3)NCH_2ONO_2$	8.8×10^{-12}, (*12*)

$(HOOCH_2)_2NCH_2O_2 + NO \rightarrow 0.93\times(HOOCH_2)_2NCH_2O + 0.93\times NO_2 + 0.07\times(HOOCH_2)_2NCH_2ONO_2$	8.8×10^{-12}, *(12)*
$(CH_3)_2NCH_2O \rightarrow (CH_3)_2NCH_2O\_decomp$	2.0×10^{6}, *(17)*
$(HOOCH_2)(CH_3)NCH_2O \rightarrow (HOCH_2)(CH_3)NCH_2O_2$	1.0×10^{10}, *(17)*
$(HOOCH_2)_2NCH_2O \rightarrow (HOOCH_2)(HOCH_2)NCH_2O_2$	6.0×10^{9}, *(17)*
$(HOCH_2)(CH_3)NCH_2O_2 (+ O_2) \rightarrow (HOOCH_2)(HOCH_2)NCH_2O_2$	0.41 *(17)*
$(HOCH_2)(CH_3)NCH_2O_2 (+ O_2) \rightarrow (HOOCH_2)(CH_3)NCHO + HO_2$	0.13 *(17)*
$(HOCH_2)(CH_3)NCH_2O_2 + NO \rightarrow 0.93\times(HOCH_2)(CH_3)NCH_2O + 0.93\times NO_2 + 0.07\times(HOCH_2)(CH_3)NCH_2ONO_2$	8.8×10^{-12}, *(12)*
$(HOCH_2)(CH_3)NCH_2O \rightarrow (HOCH_2)(CH_3)NCH_2O\_decomp$	3.0×10^{5}, *(17)*
$(HOOCH_2)(HOCH_2)NCH_2O_2 \rightarrow (HOOCH_2)(HOCH_2)NCHO + OH$	0.0060 *(17)*
$(HOOCH_2)(HOCH_2)NCH_2O_2 (+ O_2) \rightarrow (HOOCH_2)_2NCHO + HO_2$	0.13 *(17)*
$(HOOCH_2)(HOCH_2)NCH_2O_2 + NO \rightarrow 0.93\times(HOOCH_2)(HOCH_2)NCH_2O + 0.93\times NO_2 + 0.07\times(HOOCH_2)(HOCH_2)NCH_2ONO_2$	8.8×10^{-12}, *(12)*
$(HOOCH_2)(HOCH_2)NCH_2O \rightarrow (HOCH_2)_2NCH_2O_2$	3.0×10^{8}, *(17)*
$(HOCH_2)_2NCH_2O_2 (+ O_2) \rightarrow (HOOCH_2)(HOCH_2)NCHO + HO_2$	0.22 *(17)*
$(HOCH_2)_2NCH_2O_2 + NO \rightarrow 0.93\times(HOCH_2)_2NCH_2O + 0.93\times NO_2 + 0.07\times(HOCH_2)_2NCH_2ONO_2$	8.8×10^{-12}, *(12)*
$(HOCH_2)_2NCH_2O (+ O_2) \rightarrow (HOCH_2)_2NCHO + HO_2$	5.4×10^{4}, *(17)*
$OH + CH_4 (+O_2) \rightarrow CH_3O_2 + H_2O$	$6.28\text{x}10^{-15}$, *(42)*
$CH_3O_2 + NO (+O_2) \rightarrow HCHO + HO_2 + NO_2$	$7.7\text{x}10^{-12}$, *(42)*
$OH + CO (+O_2) \rightarrow CO_2 + HO_2$	$1.66\text{x}10^{-13}$, *(45)*

Background concentrations of CH_4 and CO in the reaction gas (air) were set at 4.6×10^{13} and 3.4×10^{12} molecules cm^{-3}, respectively, representing average concentrations in the northern hemisphere. It is to be noted, that the reaction gas air is taken from a PSA (Pressure Swing Adsorption) unit with further purification by a series of absorbers not changing the CH_4 and CO content significantly.

S1.6. Additional information from TROPOS experiments

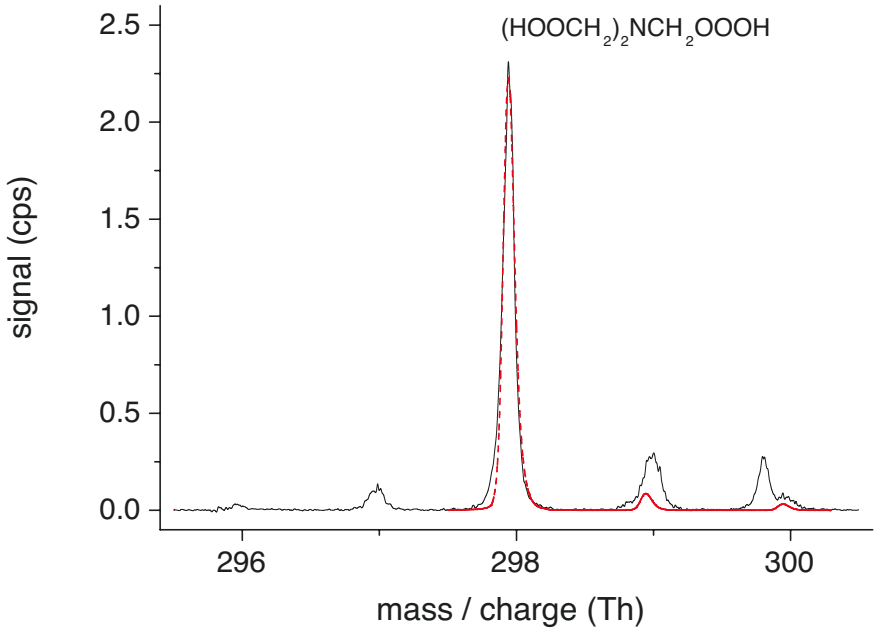

Fig. S 1 Product spectrum from OH + trimethylamine measured by iodide ionization. The product signal appears as an adduct with iodide I^- and is shifted by 126.9 Th. The spectrum represents the measured raw spectrum obtained from 10 min data accumulation. The red trace is the signal of $((HOOCH_2)_2NCH_2OOOH)I^-$ from peak fitting. Reactant concentrations were: [trimethylamine] = 2.6×10^{10}, [IPN] = 1.5×10^{11} and [NO] = 1.0×10^{10} molecules cm^{-3}.

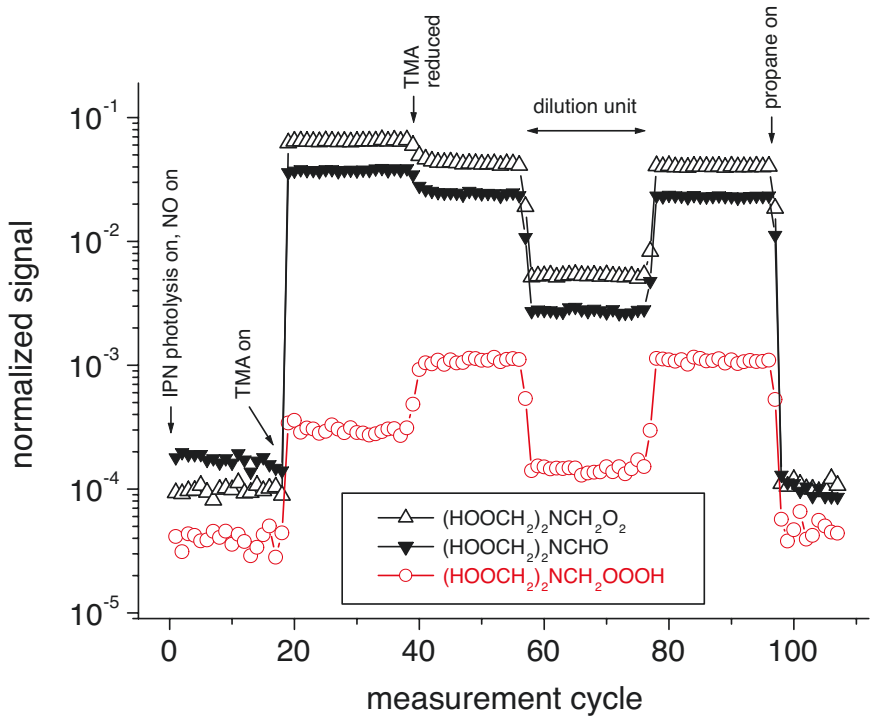

Fig. S2: Product traces from OH + trimethylamine for different reaction conditions. Product ionization was carried out by iodide. Reactant concentrations were: [trimethylamine] = 1.5×10^{10} or 1.5×10^{11}, [IPN] = 1.5×10^{11} and [NO] = 1.0×10^{10} molecules cm^{-3}. IPN photolysis with NO addition was running during the whole time period. One measurement cycle comprises 60 s data accumulation. Trimethylamine (TMA), 1.5×10^{11} molecules cm^{-3}, was added to the reaction gas at measurement cycle 19. TMA was lowered to 1.5×10^{10} molecules cm^{-3} at measurement cycle 38. Reducing the TMA concentration leads to lowering of the production of $(HOOCH_2)_2NCH_2O_2$ radicals and the corresponding isomerization product $(HOOCH_2)_2NCHO$ while the $(HOOCH_2)_2NCH_2OOOH$ production increases, see also Fig. 1B and explanations in the main text. A sampling device including a dilution unit (dilution factor: ~7/1, dilution gas: N_2) was inserted instead of the commonly used sampling tube in the range of measurement cycles 57 to 77. All measured product signals decreased according to the dilution in a parallel way. This indicates that product formation is not distinctly influenced by any unwanted processes during the ionization process in the ion-molecule reaction zone. Otherwise, the signals would not follow the dilution factor. At measurement cycle 97, propane with a concentration of 4.9×10^{15} molecules cm^{-3} was added to the reaction gas consuming the OH radicals almost completely. All product signals dropped down close to the background level. That demonstrates that all products solely originate from OH radical reactions.

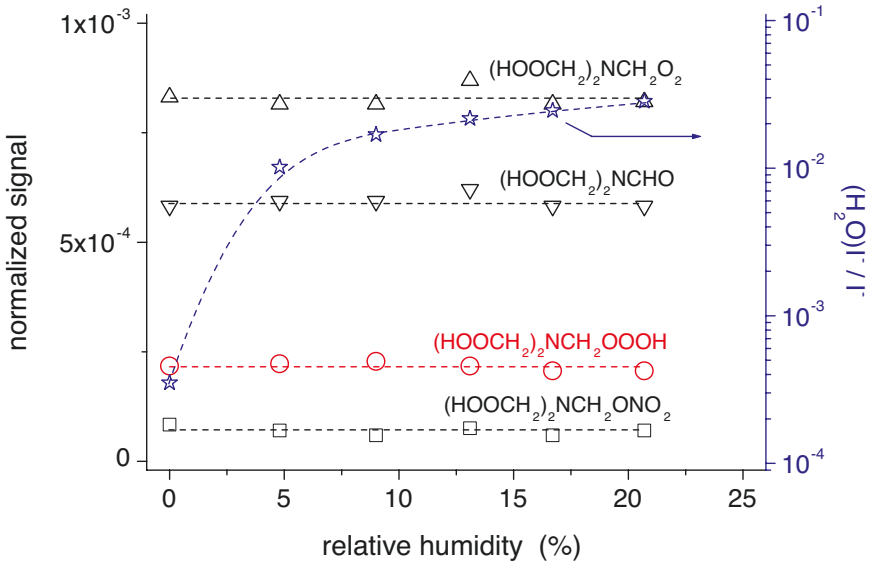

Fig. S3: Product formation from OH + trimethylamine as a function of relative humidity, < 0.1 - 21 %. Product ionization was carried out by iodide. Reactant concentrations were: [trimethylamine] = 4.0×10^{10}, [IPN] = 1.6×10^{12} and [NO] = 2.0×10^{10} molecules cm^{-3}. Product sampling was carried out by means of a two-stage dilution unit (dilution factor of ~150) in order to keep the water vapor content in the IMR zone small. The dilution gas was high-grade nitrogen. Rising water content was monitored by means of the $(H_2O)I^-$ signal. The blue stars show the signal ratio $(H_2O)I^-/ I^-$. The measured (normalized) signals had an uncertainty of < 20 %.

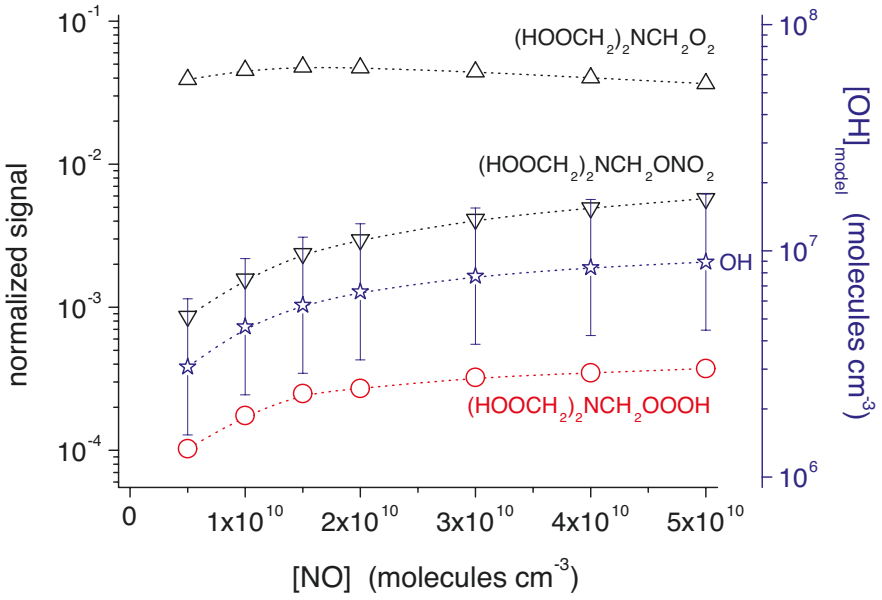

Fig. S4: Product formation from OH + trimethylamine as a function of NO. Product ionization was carried out by iodide. Stated OH concentrations are the result from modelling with an assumed uncertainty of a factor of 2 as shown by the error bars. The signal of the organic nitrate $(HOOCH_2)_2NCH_2ONO_2$, formed via NO + RO_2 → $RONO_2$, increased with rising NO almost parallel to the calculated OH concentration formed via NO + HO_2 → OH + NO_2. The signal of the RO_2 radical $(HOOCH_2)_2NCH_2O_2$ (compound **I** in the main text) first increased due to the relatively strong increase in OH and then slightly declined according to rising importance of NO + RO_2 reactions. The signal of the hydrotrioxide $(HOOCH_2)_2NCH_2OOOH$ (**III**) followed the product signal(RO_2) × $[OH]_{model}$ as expected from ROOOH´s formation kinetics, see Fig. S5. Reactant concentrations were: [trimethylamine] = 5.2×10^{11}, [IPN] = 1.5×10^{11} and [NO] = $(5.0 - 50) \times 10^9$ molecules cm^{-3}.

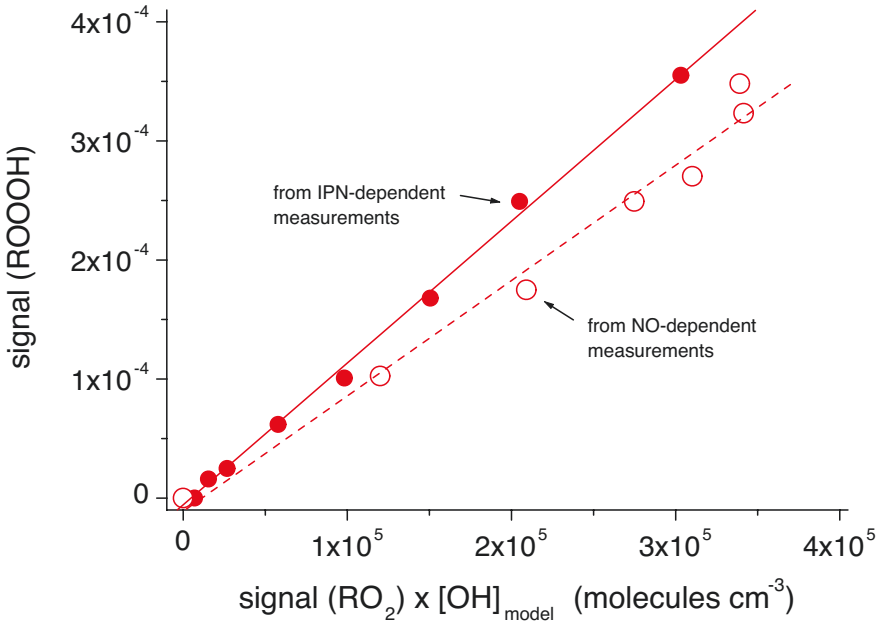

Fig. S5: OH + trimethylamine: Relation of signal(ROOOH) vs. signal(RO_2) × $[OH]_{model}$. The given normalized signals of ROOOH, $(HOOCH_2)_2NCH_2OOOH$, and RO_2 radicals, $(HOOCH_2)_2NCH_2O_2$, as well as the OH concentrations from modelling were taken from the experiments as shown in Fig. 1A and Fig. S4. The measured (normalized) product signals had an uncertainty of < 20%. An uncertainty of a factor of 2 in $[OH]_{model}$ is estimated. Error bars are not shown. Assuming close to maximum detection sensitivity for this highly oxidized RO_2 radical and the corresponding ROOOH, data analysis according to equation (SXII) yielded $k((HOOCH_2)_2NCH_2O_2+OH) = (3.2 \pm 0.1) \times 10^{-10}$ cm^3 molecule^{-1} s^{-1} from the IPN-dependent measurements, see Fig. 1A, and $(2.6 \pm 0.3) \times 10^{-10}$ cm^3 molecule^{-1} s^{-1} from the NO-dependent measurements, see Fig. S4. Stated error range considers the statistical error only. The overall uncertainty in $k((HOOCH_2)_2NCH_2O_2+OH)$ is assumed to be not higher than a factor of 5.

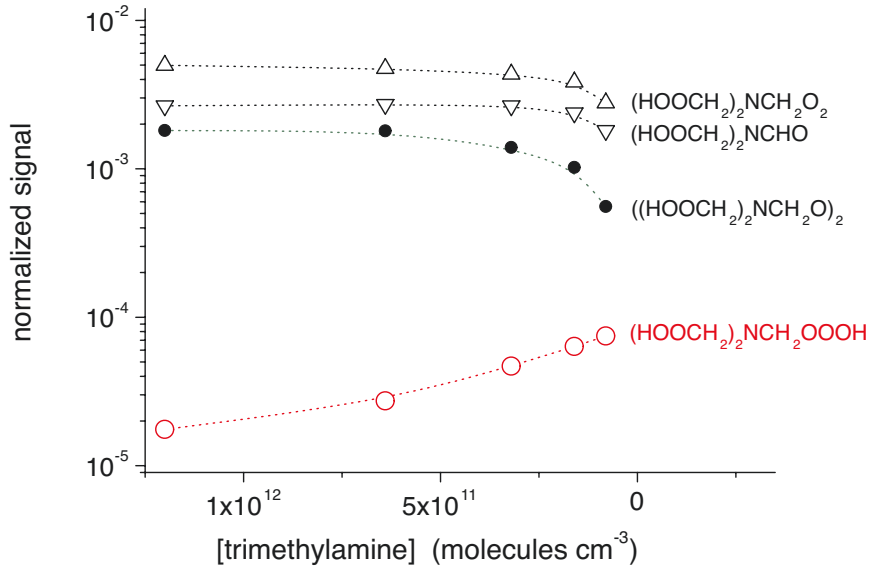

Fig. S6: Product formation from OH + trimethylamine measured by nitrate ionization. Rising OH levels in the measurement series result from a constant OH production rate with constant photolysis conditions, i.e., constant IPN and NO concentrations, and lowering of the OH loss rate by reducing the main OH consumer trimethylamine. $(HOOCH_2)_2NCH_2O_2$ (compound **I** in the main text) is the highest oxidized RO_2 radical in this system, $(HOOCH_2)_2NCHO$ (**II**) the amide formed from RO_2 isomerization, $((HOOCH_2)_2NCH_2O)_2$ (**IV**) the accretion product from the reaction $RO_2 + RO_2 \rightarrow ROOR + O_2$, and $(HOOCH_2)_2NCH_2OOOH$ (**III**) the hydrotrioxide formed via RO_2 + OH. Reactant concentrations were: [trimethylamine] = (8.0 - 120) × 10^{10}, [IPN] = 1.56 × 10^{12} and [NO] = 2.0 × 10^{10} molecules cm^{-3}.

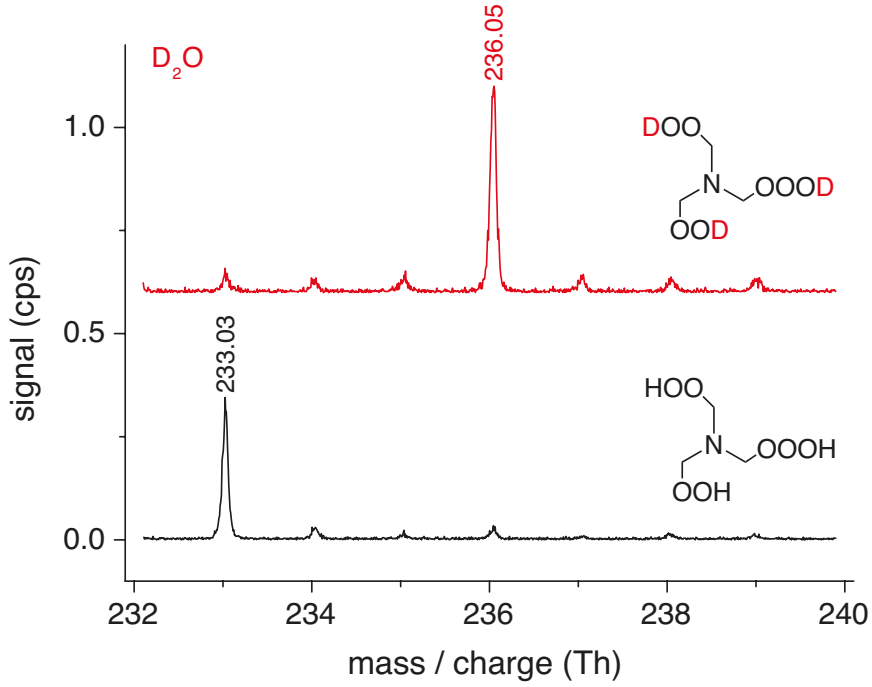

Fig. S7: Results of the H/D exchange experiment in the OH + trimethylamine reaction. Signals attributed to the hydrotrioxide $(HOOCH_2)_2NCH_2OOOH$ were measured in the absence and presence of heavy water (D_2O), product ionization by nitrate. In the latter case, a stream of N_2 saturated with D_2O was added to the sample gas just before the entrance to the ion-molecule reaction zone. The products appear as the adduct with nitrate. The process of H/D exchange is likely due to reactions of $(DNO_3)NO_3^-$ and $(DNO_3)_2NO_3^-$ during ionization. The calculated adduct masses are in very good agreement with the measurements as given in the spectra, $((HOOCH_2)_2NCH_2OOOH)NO_3^-$: 233.026 Th and $((DOOCH_2)_2NCH_2OOOD)NO_3^-$: 236.045 Th. Reactant concentrations were: [trimethylamine] = 8.0×10^{10}, [IPN] = 1.56×10^{12} and [NO] = 2.0×10^{10} molecules cm^{-3}.

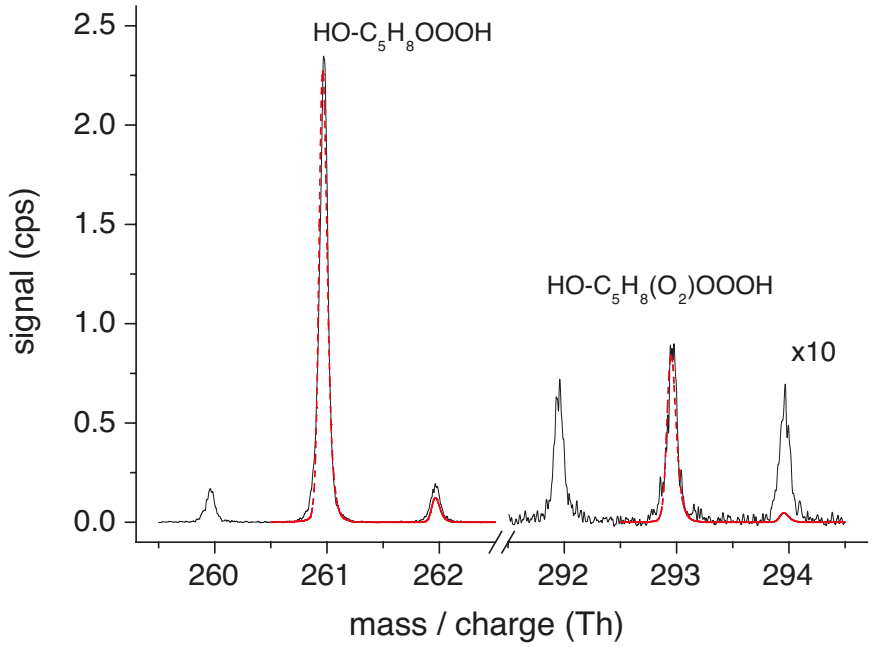

Fig. S8: Product spectrum from OH + isoprene measured by iodide ionization. The product signals appear as an adduct with iodide I^- and are shifted by 126.9 Th. The spectrum represents the measured raw spectrum obtained from 10 min data accumulation. The red traces are the signals of $(HO\text{-}C_5H_8OOOH)I^-$ and $(HO\text{-}C_5H_8(O_2)OOOH)I^-$ from peak fitting. Reactant concentrations were: [isoprene] = 1.02×10^{10}, [IPN] = 2.15×10^{11} and [NO] = 1.0×10^{10} molecules cm^{-3}.

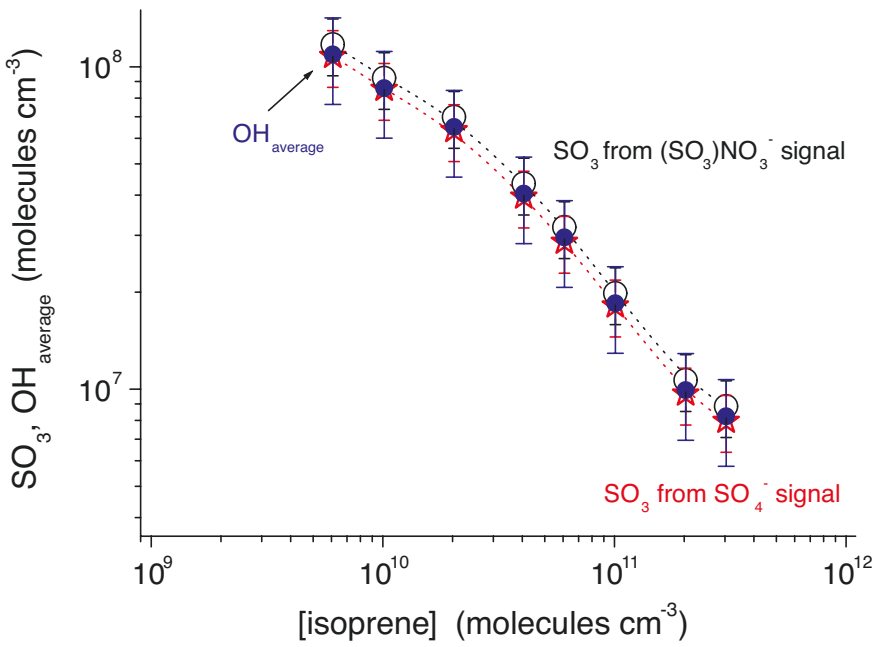

Fig. S9: Average OH radical concentrations derived from SO_3 measurements, OH + isoprene reaction. SO_3 formation has been followed from the OH + SO_2 reaction conducted in parallel to the OH + isoprene reaction. SO_3 detection was carried out by means of nitrate ionization monitoring the signals of $(SO_3)NO_3^-$ and SO_4^-. (*37*) The uncertainty of the SO_3 calibration is estimated to be less than ± 20 % as shown by the error bars. (*38*) The average OH radical concentration was calculated from the mean value of the resulting SO_3 concentrations according to equation (SVI). The SO_2 addition was kept small in order to prevent disturbance of the OH + isoprene reaction, $[SO_2] = 2.47 \times 10^{11}$ and [isoprene] = (6.08 - 304) × 10^9 molecules cm^{-3}. The ratio of the OH reactivity $k_{OH+isoprene} \times$ [isoprene] / $k_{OH+SO2} \times [SO_2]$ is in the range 4.3 - 213. The resulting uncertainty (Gauß´s propagation of uncertainty) of the average OH radical concentrations is calculated to be about 30 % assuming an uncertainty of ± 20 % in k_{OH+SO2} (*39*) and the uncertainty of the SO_3 calibration of 20 %.

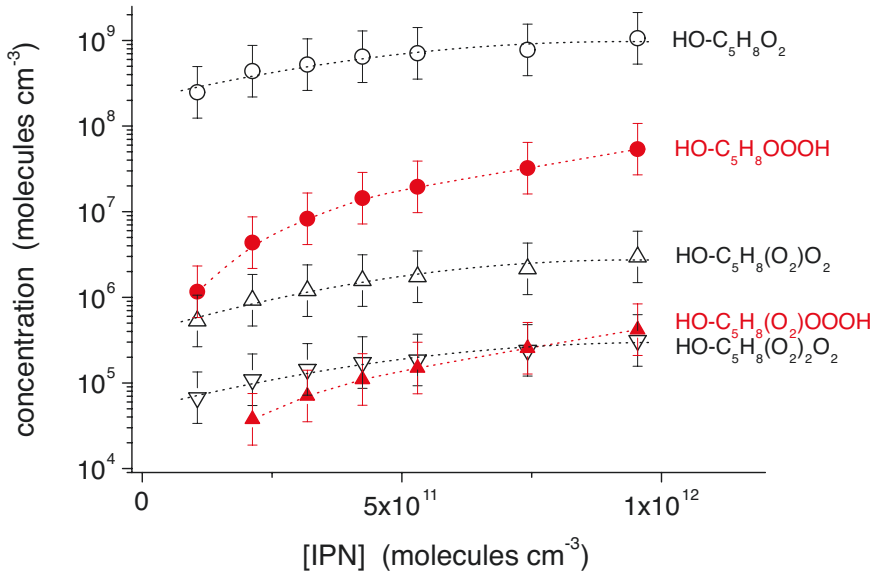

Fig. S10: Formation of RO_2 radicals and hydrotrioxides from OH + isoprene. Product concentrations were obtained using calibration factors based on former investigations, see explanations in Section S1.3. OH and RO_2 radical concentrations increased in the experiment with rising IPN concentrations, [IPN] = (1.06 - 9.54) × 10^{11}, [NO] = 1.0 × 10^{10} and [isoprene] = 2.03 × 10^{10} molecules cm^{-3}. Product ionization was carried out by iodide. The HO-$C_5H_8(O_2)_2OOOH$ signal is expected to be below the detection limit. Product concentrations had an expected uncertainty of a factor of 2 as shown by the error bars.

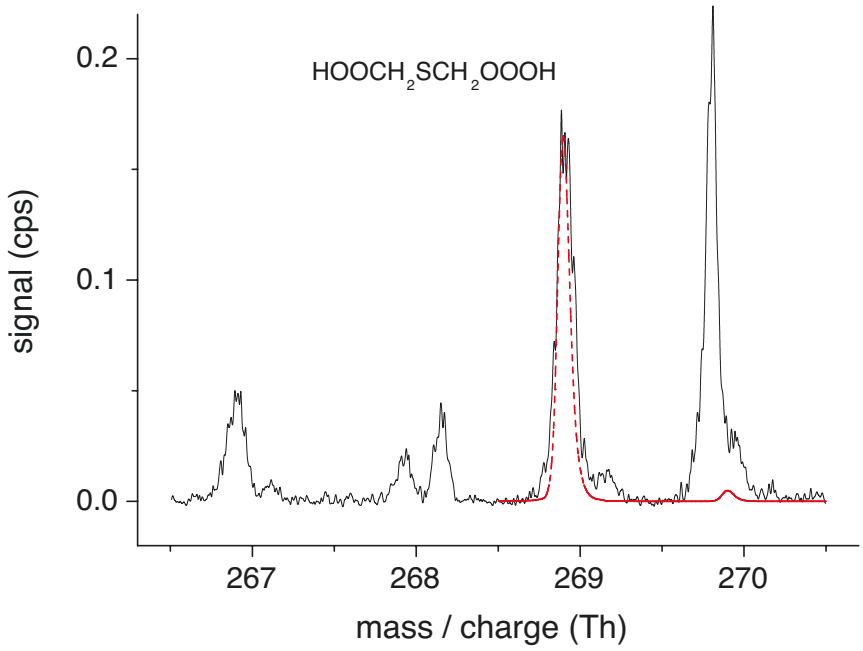

Fig. S11: Product spectrum from OH + dimethyl sulfide (DMS) measured by iodide ionization. The product signal appears as an adduct with iodide I^- and is shifted by 126.9 Th. The spectrum represents the measured raw spectrum obtained from 10 min data accumulation. The red trace is the signal of $(HOOCH_2SCH_2OOOH)I^-$ from peak fitting. Reactant concentrations were: [DMS] = 2.5×10^{11}, [IPN] = 2.12×10^{11} and [NO] = 1.0×10^{10} molecules cm^{-3}.

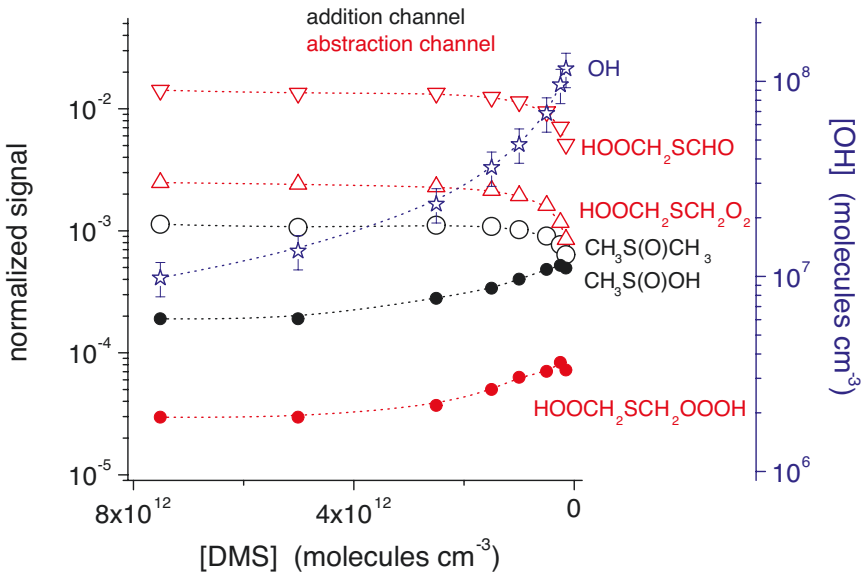

Fig. S12: Product formation, including the hydrotrioxide, from OH + DMS. Products from the addition channel are given in black and those from the abstraction channel in red. (*46-48*) Product measurements were carried out by iodide ionization. The OH level increased in the experiment due to lowering of the DMS concentration in the reaction gas for constant photolysis conditions, [IPN] = 2.12×10^{11}, [NO] = 1.0×10^{10} and [DMS] = $(1.5 - 75.1) \times 10^{11}$ molecules cm^{-3}. In an additional experiment in the presence of SO_2 for otherwise identical reaction conditions, the OH concentration was determined indirectly by monitoring SO_3 formation from OH + SO_2 identical to the approach as described for OH + isoprene, see Fig. S9. The average OH radical concentration was calculated from the mean value of the resulting SO_3 concentrations according to equation (SVI). The SO_2 addition was kept small in order to prevent disturbance of the OH + DMS reaction, [SO_2] = 2.47×10^{11} molecules cm^{-3}. Resulting uncertainty of the average OH radical concentrations is calculated to be about 30 %, shown by the error bars. $CH_3S(O)CH_3$ (DMSO) is a main product from the addition channel of the OH + DMS reaction. (*46*) $CH_3S(O)OH$ (MSIA) is produced from OH + DMSO, i.e., it represents a product of a secondary OH reaction. $HOOCH_2SCH_2O_2$ radicals are generated via RO_2 isomerization of the primarily formed $CH_3SCH_2O_2$ radicals from the abstraction channel of OH + DMS. $HOOCH_2SCHO$ results from the rapid $HOOCH_2SCH_2O_2$ isomerization. (*47, 48*) The signal of the hydrotrioxide $HOOCH_2SCH_2OOOH$, formed via $HOOCH_2SCH_2O_2$ + OH, increases with rising OH level in the experiment in an almost parallel way as MSIA that is also formed in a secondary OH reaction.

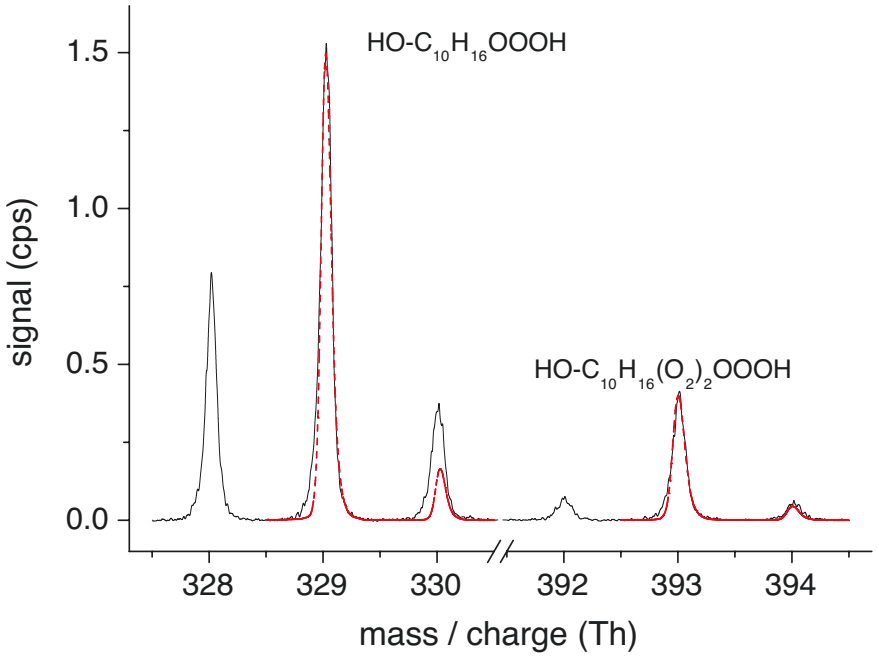

Fig. S13: Product spectrum from OH + α-pinene measured by iodide ionization. The product signals appear as an adduct with iodide I^- and are shifted by 126.9 Th. The spectrum represents the measured raw spectrum obtained from 10 min data accumulation. The red traces are the signals of $(HO\text{-}C_{10}H_{16}OOOH)I^-$ and $(HO\text{-}C_{10}H_{16}(O_2)_2OOOH)I^-$ from peak fitting. Reactant concentrations were: [α-pinene] = 2.0×10^{10}, [IPN] = 2.15×10^{11} and [NO] = 1.0×10^{10} molecules cm^{-3}.

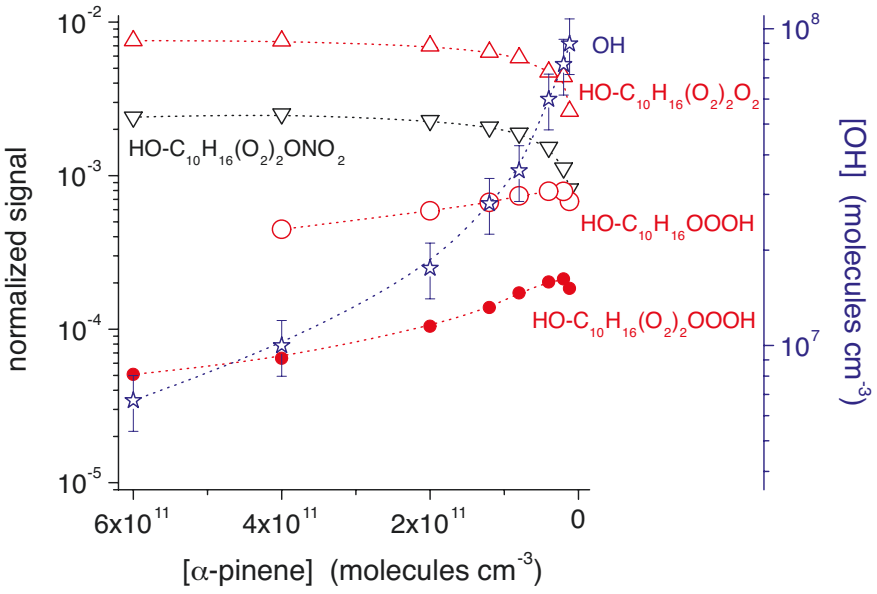

Fig. S14: Product formation, including the hydrotrioxides, from OH + α-pinene. Product measurements were carried out by iodide ionization. The OH level increased in the experiment due to lowering of the α-pinene concentration in the reaction gas for constant photolysis conditions, [IPN] = 2.15×10^{11}, [NO] = 1.0×10^{10} and [α-pinene] = $(1.2 - 60) \times 10^{10}$ molecules cm^{-3}. In an additional experiment in the presence of SO_2 for otherwise identical reaction conditions, the OH concentration was determined indirectly by monitoring SO_3 formation from OH + SO_2 identical to the approach as described for OH + isoprene, see Fig. S9. The average OH radical concentration was calculated from the mean value of the resulting SO_3 concentrations according to equation (SVI). The SO_2 addition was kept small in order to prevent disturbance of the OH + α-pinene reaction, [SO_2] = 2.47×10^{11} molecules cm^{-3}. Resulting uncertainty of the average OH radical concentrations is calculated to be about 30 %, shown by the error bars. HO-$C_{10}H_{16}(O_2)_2O_2$ represents the highest oxidized RO_2 radical in this reaction system (*10, 38*) and HO-$C_{10}H_{16}(O_2)_2ONO_2$ the corresponding organic nitrate formed via $RO_2 + NO \rightarrow RONO_2$ with a practically constant NO level in the experiment. The observed hydrotrioxides HO-$C_{10}H_{16}OOOH$ and HO-$C_{10}H_{16}(O_2)_2OOOH$ are formed from the OH reaction of the least and highest oxidized RO_2 radicals, respectively.

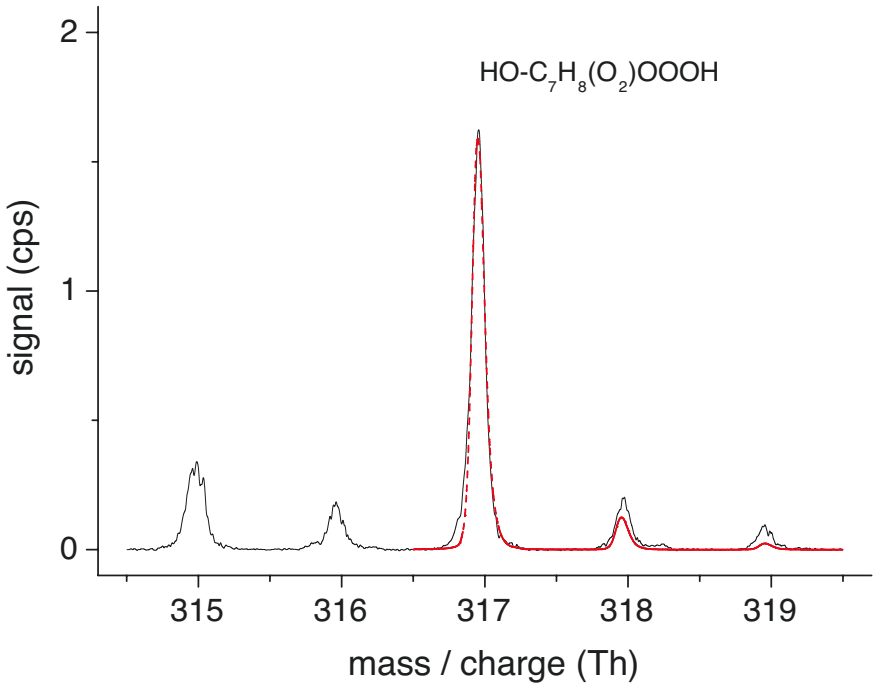

Fig. S15: Product spectrum from OH + toluene measured by iodide ionization. The product signal appears as an adduct with iodide I^- and is shifted by 126.9 Th. The spectrum represents the measured raw spectrum obtained from 10 min data accumulation. The red trace is the signals of $(HO\text{-}C_7H_8(O_2)OOOH)I^-$ from peak fitting. The reactant concentrations were: [toluene] = 1.65×10^{11}, [IPN] = 2.15×10^{11} and [NO] = 1.0×10^{10} molecules cm^{-3}.

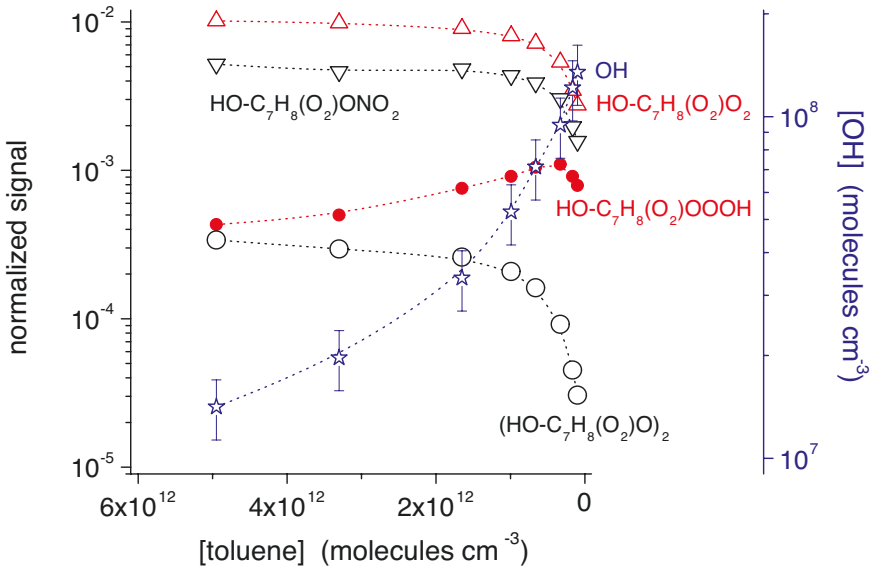

Fig. S16: Product formation, including the hydrotrioxide, from OH + toluene. Product measurements were carried out by iodide ionization. The OH level increased in the experiment due to lowering of the toluene concentration in the reaction gas for constant photolysis conditions, [IPN] = 2.15×10^{11}, [NO] = 1.0×10^{10} and [toluene] = $(9.9 - 495) \times 10^{10}$ molecules cm^{-3}. In an additional experiment in the presence of SO_2 for otherwise identical reaction conditions, the OH concentration was determined indirectly by monitoring SO_3 formation from OH + SO_2 identical to the approach as described for OH + isoprene, see Fig. S9. The average OH radical concentration was calculated from the mean value of the resulting SO_3 concentrations according to equation (SVI). The SO_2 addition was kept small in order to prevent disturbance of the OH + toluene reaction, [SO_2] = 2.47×10^{11} molecules cm^{-3}. Resulting uncertainty of the average OH radical concentrations is calculated to be about 30 %, shown by the error bars. HO-$C_7H_8(O_2)O_2$ represents the first detectable RO_2 radical in this reaction system likely formed after the rapid endo-cyclization of the primarily produced HO-$C_7H_8O_2$ radical. (*49*) HO-$C_7H_8(O_2)ONO_2$ is the corresponding organic nitrate and $(HO\text{-}C_7H_8(O_2)O)_2$ is the accretion product from the $RO_2 + RO_2 \rightarrow ROOR + O_2$ reaction. The signal of the hydrotrioxide HO-$C_7H_8(O_2)OOOH$, formed via HO-$C_7H_8(O_2)O_2$ + OH, follows the product [HO-$C_7H_8(O_2)O_2$] × [OH].

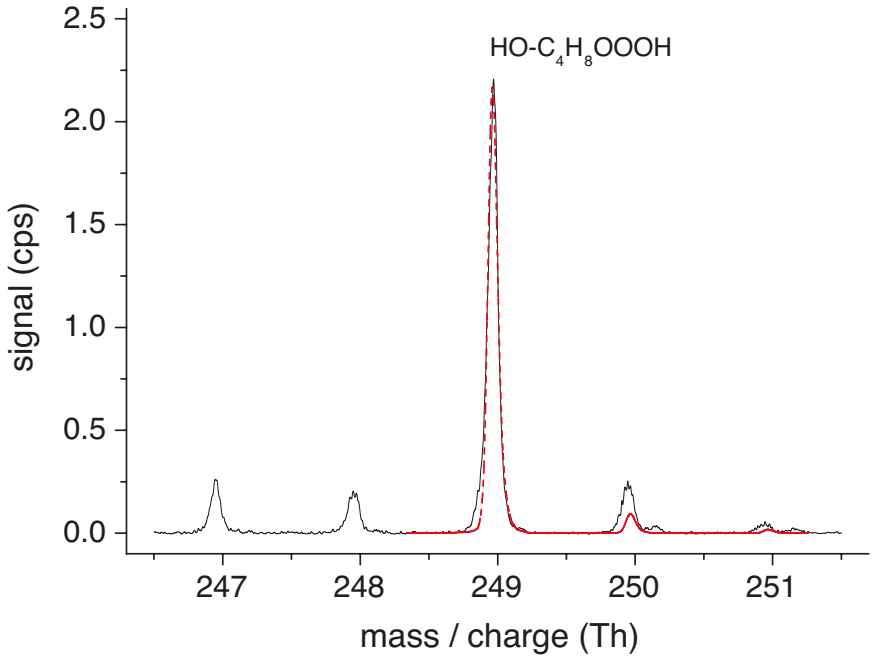

Fig. S17: Product spectrum from OH + 1-butene measured by iodide ionization. The product signal appears as an adduct with iodide I^- and is shifted by 126.9 Th. The spectrum represents the measured raw spectrum obtained from 10 min data accumulation. The red trace is the signals of $(HO\text{-}C_4H_8OOOH)I^-$ from peak fitting. The reactant concentrations were: [1-butene] = 3.0×10^{10}, [IPN] = 2.15×10^{11} and [NO] = 1.0×10^{10} molecules cm^{-3}.

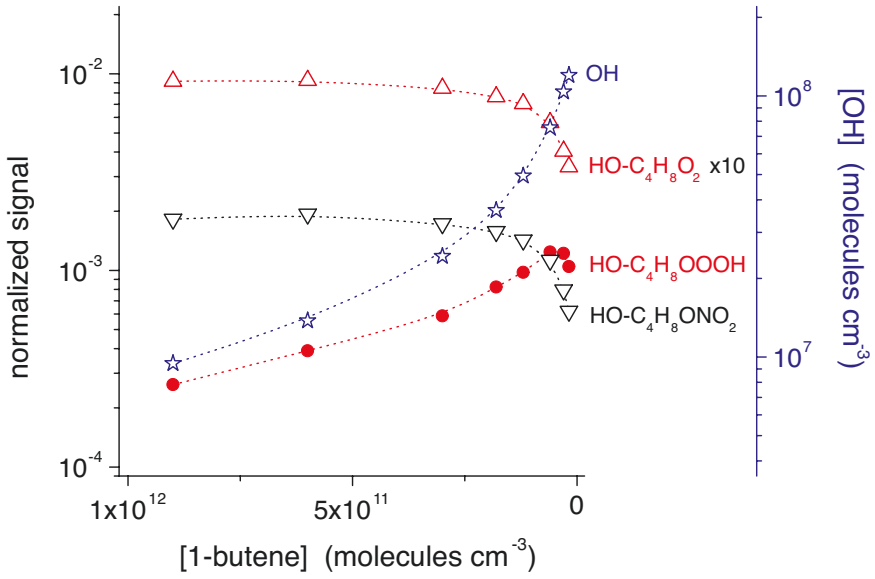

Fig. S18: Product formation, including the hydrotrioxide, from OH + 1-butene. Product measurements were carried out by iodide ionization. The OH level increased in the experiment due to lowering of the 1-butene concentration in the reaction gas for constant photolysis conditions, [IPN] = 2.15 × 10^{11}, [NO] = 1.0 × 10^{10} and [1-butene] = (1.8 - 90) × 10^{10} molecules cm^{-3}. In an additional experiment in the presence of SO_2 for otherwise identical reaction conditions, the OH concentration was determined indirectly by monitoring SO_3 formation from OH + SO_2 identical to the approach as described for OH + isoprene, see Fig. S9. The average OH radical concentration was calculated from the mean value of the resulting SO_3 concentrations according to equation (SVI). The SO_2 addition was kept small in order to prevent disturbance of the OH + 1-butene, [SO_2] = 2.47 × 10^{11} molecules cm^{-3}. Resulting uncertainty of the average OH radical concentrations is calculated to be about 30 %, shown by the error bars. HO-$C_4H_8O_2$ is the formed RO_2 radical from the OH addition to 1-butene and HO-$C_4H_8ONO_2$ the corresponding organic nitrate.

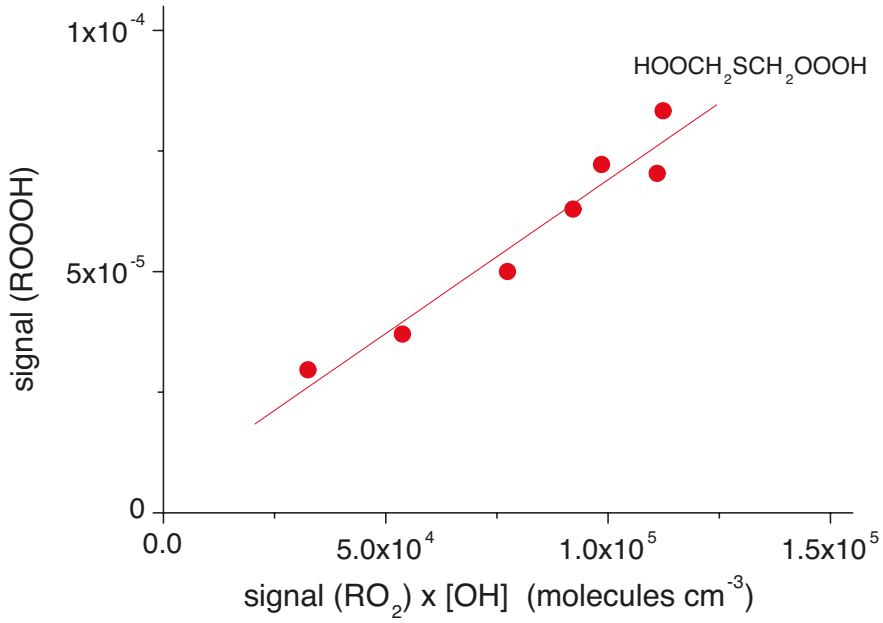

Fig. S19: OH + DMS: Relation of signal(ROOOH) vs. signal(RO_2) × [OH]. The given normalized signals of ROOOH, $HOOCH_2SCH_2OOOH$, and RO_2 radicals, $HOOCH_2SCH_2O_2$, as well as the measured average OH concentrations were taken from the experiments as given in Fig. S12. Error bars are not shown. Determination of the rate coefficient k(RO_2+OH) seems to be impossible because we cannot ensure close to maximum (or similar) detection sensitivity for ROOOH and the RO_2 radical in this reaction system.

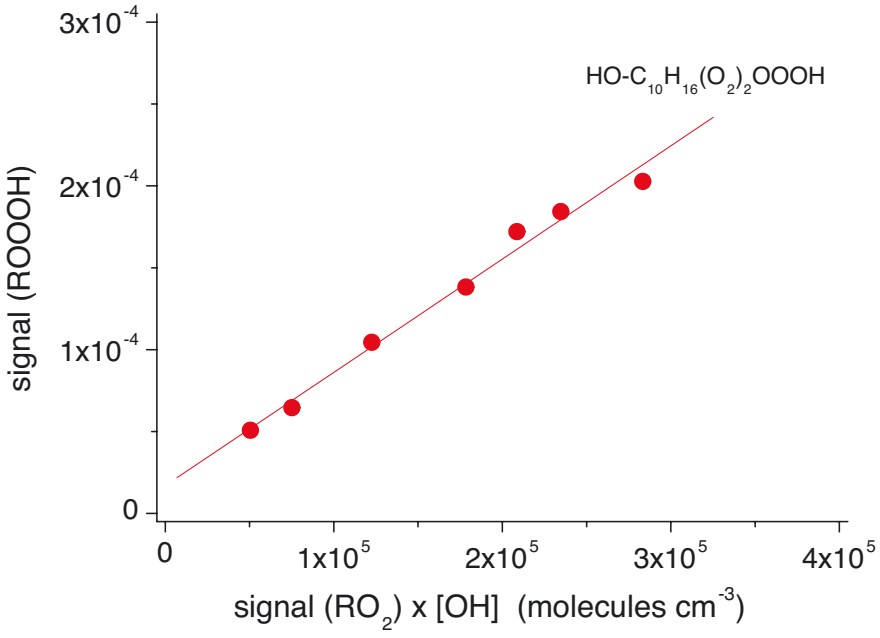

Fig. S20: OH + α-pinene: Relation of signal(ROOOH) vs. signal(RO_2) × [OH]. The given normalized signals of ROOOH, HO-$C_{10}H_{16}(O_2)_2OOOH$, and RO_2 radicals, HO-$C_{10}H_{16}(O_2)_2O_2$, as well as the measured average OH concentrations were taken from the experiments as given in Fig. S14. An uncertainty of ± 29 % in [OH] is calculated. Error bars are not shown. Assuming close to maximum detection sensitivity for this highly oxidized RO_2 radical and the corresponding ROOOH, data analysis according to equation (SXII) yielded a value k(HO-$C_{10}H_{16}(O_2)_2O_2$+OH) = (1.8 ± 0.2) × 10^{-10} cm^3 $molecule^{-1}$ s^{-1}. Stated error range considers the statistical error only. The overall uncertainty in k(HO-$C_{10}H_{16}(O_2)_2O_2$+OH) is assumed to be not higher than a factor of 5.

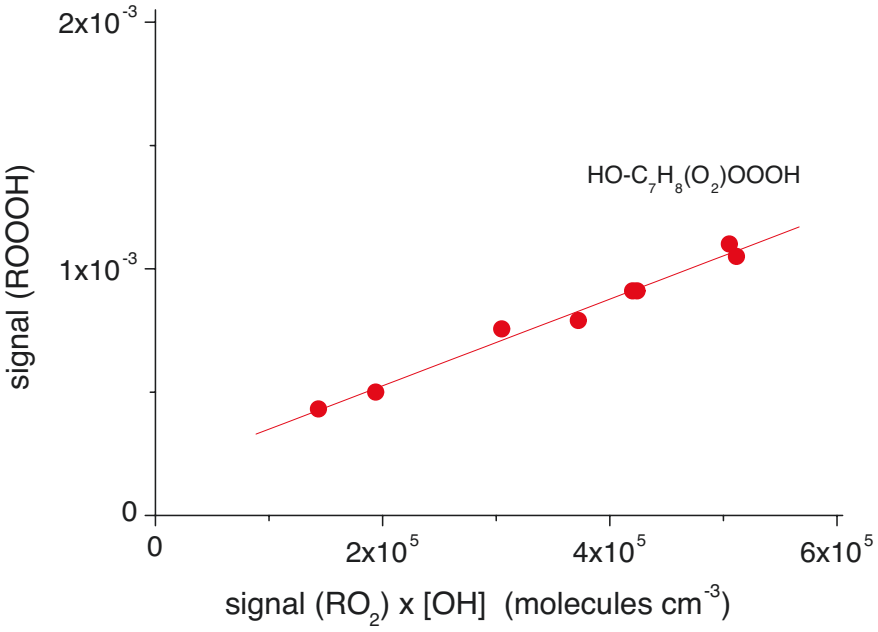

Fig. S21: OH + toluene: Relation of signal(ROOOH) vs. signal(RO_2) × [OH]. The given normalized signals of ROOOH, HO-$C_7H_8(O_2)$OOOH, and RO_2 radicals, HO-$C_7H_8(O_2)O_2$, as well as the measured average OH concentrations were taken from the experiments as given in Fig. S16. Error bars are not shown. Determination of the rate coefficient k(RO_2+OH) seems to be impossible because we cannot ensure close to maximum (or similar) detection sensitivity for ROOOH and the RO_2 radical.

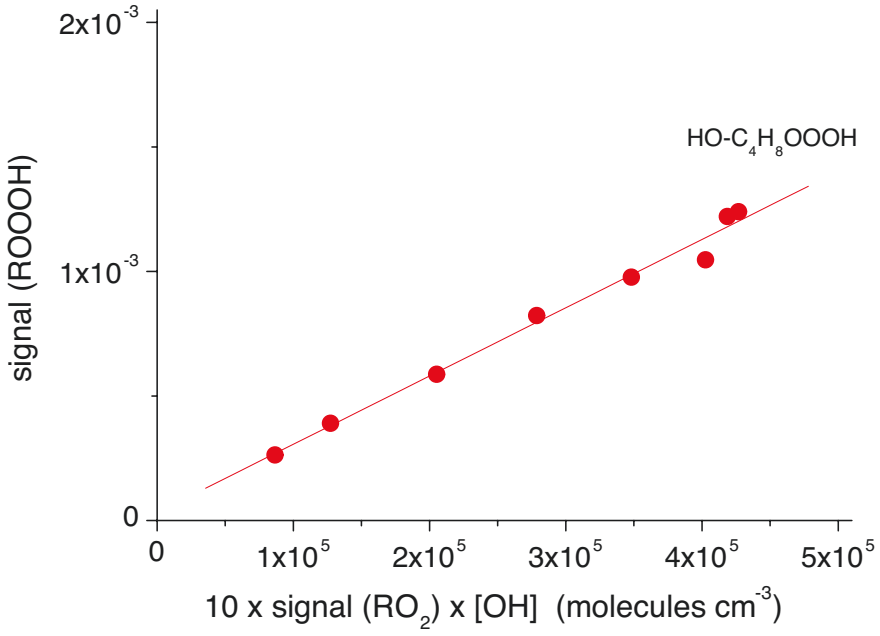

Fig. S22: OH + 1-butene: Relation of signal(ROOOH) vs. signal(RO_2) × [OH]. The given normalized signals of ROOOH, HO-C_4H_8OOOH, and RO_2 radicals, HO-$C_4H_8O_2$, as well as the measured average OH concentrations were taken from the experiments as given in Fig. S18. Error bars are not shown. Determination of the rate coefficient k(RO_2+OH) seems to be impossible because we cannot ensure close to maximum (or similar) detection sensitivity for ROOOH and the RO_2 radical.

S1.7. Caltech experiments on 2-methylpropene

Signals using CF_3O^- chemical ionization mass spectrometry consistent with a hydrotrioxide were observed following the reaction of 2-methylpropene with OH (and O_2) in experiments conducted in a 1 m^3 Teflon (FEP) chamber at Caltech at RH < 0.3 %. Here, 2-methylpropene and H_2O_2 were introduced into the bag with clean air. The experiments were conducted as batch mode reactions at 296 K and 745 torr with contents being sampled and analyzed as a function of time using the Caltech CF_3O^- Chemical Ionization Mass Spectrometer (CIT-CIMS) operating with a resolving power of about 1000. (*50*) The contents from the experiment bag were sampled by the CIMS through a 2 m length of 4 mm ID Teflon (PFA) tubing. The flow rate to the instrumentation was ~2 standard (273K, 1 atm) liters per minute (slm). Approximately 0.120 slm was sub-sampled and diluted with 1.6 slm N_2 within the CIMS instrument.

Eight 48 inch, ozone-free 254 nm mercury vapor UV lamps (G40T10) illuminated the bag ($J_{H2O2} \sim 5\times10^{-4}$ s^{-1}), initiating the chemistry by generating OH radicals from H_2O_2 photolysis:

$$H_2O_2 + h\nu\ (254\text{nm}) \rightarrow 2\ OH$$

The initial concentrations of alkene and H_2O_2 (400 ppbv and 1000 ppbv, respectively) were such that, initially, most (> 90 %) of the OH reacted with the alkene as compared with H_2O_2, as estimated using recommended rate coefficients from the literature (IUPAC). From initial OH production and loss rate calculations, OH is estimated to reach some 10^7 molecules cm^{-3}. Under these conditions, fast RO_2 + OH reactions may be expected to occur, particularly for RO_2 species which react slowly by RO_2 + RO_2 reactions, and thus accumulate in the system. This appears to be the case for the dominant RO_2 (tertiary) initially formed in the OH + 2-methylpropene system. Upon UV illumination, products arising from the radical chemistry occurring in the bag were observed in the CIMS. These included signals with m/z 190, 207, 173, 175, and 191 which are consistent with CF_3O^- cluster ions formed from CF_3O^- reacting with 2-methylpropene derived hydroxy peroxy radical (RO_2), hydroxy hydrotrioxide, hydroxy carbonyl, diol, and ROOH, respectively. Ion signals are normalized by the sum of ^{13}C isotopes of reagent ions ($^{13}CF_3O^-$, $^{13}CF_3O^-{\bullet}H_2O$, and $^{13}CF_3O^-{\bullet}H_2O_2$). Significant levels of hydroxy hydroperoxide (ROOH) are observed (Fig. S23 panel A), despite initial conditions set to limit HO_2 production from OH + H_2O_2 reactions. We attribute the formation of ROOH to arise in large part from secondary HO_2 produced from RO_2 + RO_2 reactions (via reactions of alkoxy radicals from the alkoxy channel), subsequently reacting with additional RO_2 radicals. High levels of RO_2 are inferred to build up in the system (~3.4 ppbv, assuming RO_2 cluster sensitivity equivalent to ROOH cluster, and not correcting for any losses in the sampling line). The signal attributed to RO_2 appears to peak and begin decreasing just before the lights are turned off. A signal attributed to the hydroxy hydrotrioxide of methylpropene accumulates during the lights on period and achieves a maximum mixing ratio of approximately 420 pptv (assuming same sensitivity as ROOH) at the time the lights were turned off.

After the UV lights were turned off, the signals corresponding to RO_2 and methylpropene hydroxy hydrotrioxide species were observed to decay exponentially in the dark with lifetimes of approximately 4 and 20 minutes, respectively (Fig. S23 panel B and C). We note that these lifetimes represent the total loss rate for these species in the environmental chamber, which may include multiple important pathways, in particular wall reactions, possibly water-catalyzed reactions analogously to the liquid phase.(*51, 52*)

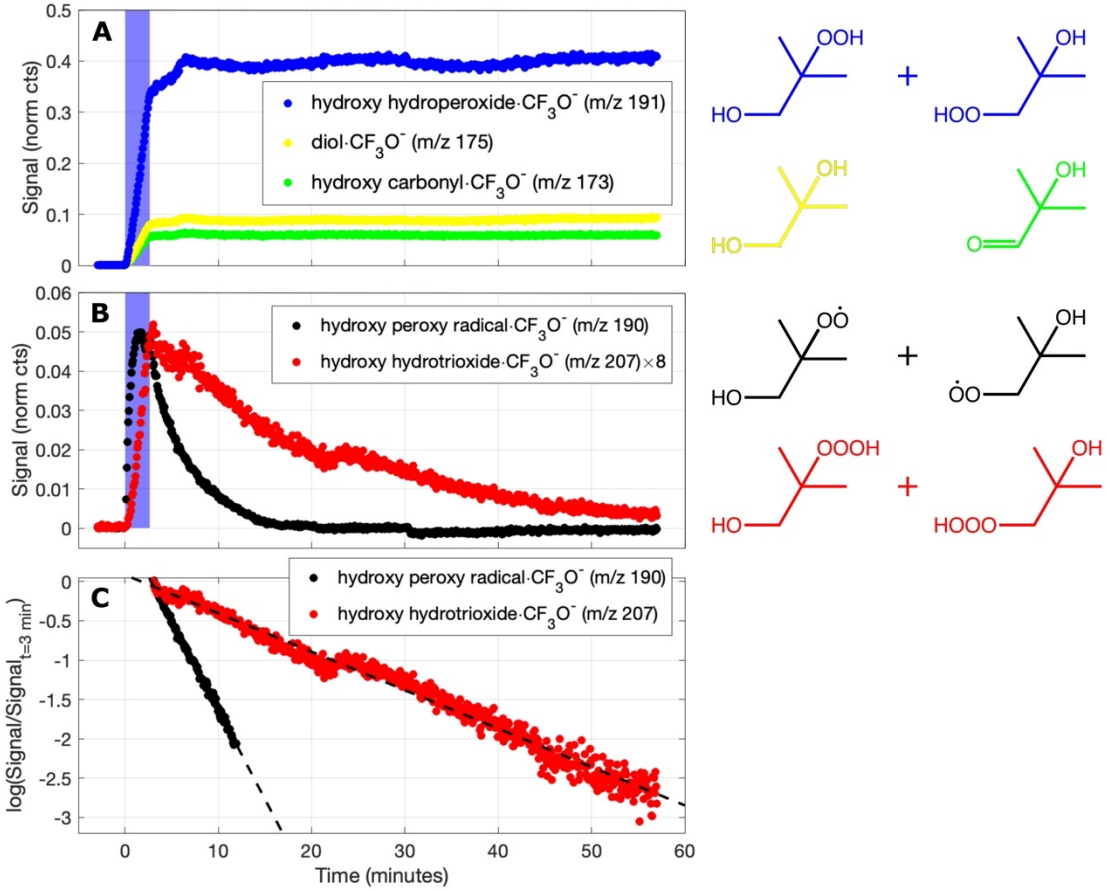

Fig. S23: CF_3O^--CIMS ion signal traces as a function of time for 2-methylpropene OH oxidation experiment in the presence of O_2. 254 nm UV lights were illuminated at t = 0 minutes generating OH from H_2O_2 photolysis and turned off at t = 2.8 minutes (blue shaded area panel A and B). Panel A shows several ion signals consistent with arising from the 2-methylpropene products, including hydroxy hydroperoxide (blue), diol (yellow), and hydroxy carbonyl (green). Panel B shows transient ion signals consistent with arising from hydroxy peroxy radical (black) and hydroxy hydrotrioxide (red) species. Panel C shows the log-linear dark decay of signals in panel B, and fitting yields lifetimes of 4.4 and 20.5 minutes for the RO_2 and the hydrotrioxide, respectively, at 296 K and 1 atm.

S2.Global modeling

S2.1. Model Setup

The simulations were performed using the chemistry-climate model ECHAM-HAMMOZ, version ECHAM6.3-HAM2.3-MOZ1.0. (*28*) The spatial configuration of the simulations is 1.875° × 1.875° horizontal resolution and 47 vertical layers up to 0.01 hPa height. The model was tested and compared for methane lifetime and the concentration budgets of key oxidants (O_3 and OH) in previous studies. The lifetime of methane was calculated to be 9.87 years and the average OH concentration 1.06×10^6 molecules cm^{-3} in the base case, which is in the range of estimates from other recent models and model inter-comparisons. (*28*)

The simulations performed in this study were carried out for the year 2017 (plus a one year model spin-up) using prescribed sea surface temperatures and sea ice cover according to the Coupled Model Intercomparison Project Phase 5 (CMIP5) AMIP simulation protocol. (*53*) The model is run in nudged mode using the ERA-Interim reanalysis from the European Center for Medium-Range Weather Forecasts (ECMWF). The global emission data of aerosols and gaseous compounds were taken from Atmospheric Chemistry and Climate Model Intercomparison Project (ACCMIP). (*54*) Emission of BVOCs are calculated online by Model of Emissions of Gases and Aerosols from Nature version 2.1 (MEGAN2.1). (*55*) Data output was every 6 hours.

S2.2. Mechanism development

Within ECHAM-HAMMOZ, the RO_2 radical chemistry is described via the common reactions with HO_2, NO, NO_3, CH_3O_2 and $CH_3C(O)O_2$ radicals. For the isoprene-derived RO_2 radicals, additionally the RO_2 isomerization step leading to the lumped species HPALD is realized. (*56*) A detailed description of the isoprene oxidation scheme and its application in ECHAM-HAMMOZ is given by Stadtler *et al.* (*57*) To study the importance of isoprene-related ROOOH formation, its formation by the reaction of RO_2 radicals with OH has been implemented. The reaction rate coefficient implemented in the chemistry mechanism is k(SXIII) = 5.1×10^{-11} cm^3 $molecules^{-1}$ s^{-1} as measured for HO-$C_5H_8O_2$ + OH, see main manuscript. Another sensitivity run was carried out with the other experimentally observed rate coefficient of k(SXIII) = 1.1×10^{-10} cm^3 $molecules^{-1}$ s^{-1}, (considered as upper limit value) to investigate the range of overall ROOOH formation potential. To investigate the role of the different ROOOH degradation pathways, the applied mechanism considers (i) the reaction with OH (SXIV), (ii) the thermal decomposition (SXV) and (iii) the photolysis yielding the corresponding alkoxy radical (SXVI). The reaction rate coefficient of the OH + ROOOH reaction is assumed to be k(SXIV) = 7.5×10^{-11} cm^3 $molecules^{-1}$ s^{-1} as measured for the corresponding hydroperoxide, ISOPOOH + OH (*26*), which is a factor of 7.5 higher as used by Fittschen *et al.* (*27*) The implemented reaction rate coefficient for the thermal decomposition of ROOOH is k(SXV) = 8.0×10^{-4} s^{-1} according to the lower limit life time derived

from the Caltech chamber experiments. To study the sensitivity of the thermal ROOOH decomposition, a further run was performed without thermal decomposition. The photolysis rate of ROOOH (J_{ROOOH}, reaction SXVI) was scaled to the photolysis rate of CH_3OOH calculated with the TUV model 5.4 (*58*) using the setup for the Master Chemical Mechanism descripted in (*59*). The theoretical calculated photolysis rate J_{ROOOH} at 0 km altitude (see Section S4.3) is about a factor of 2.6 higher than that calculated for CH_3OOH. In the ECHAM-HAMMOZ model, J_{ROOOH} is calculated as the product of the absorption cross section and the quantum yield of CH_3OOH, together with the extra-atmospheric solar flux and the atmospheric transmission function multiplied with the factor 2.6. (*60*) To assess the total ROOOH production during the simulation, a counter species (SROOOH) was added in the reaction scheme (see SXIII) that is not further oxidized or deposited.

$$RO_2 + OH \rightarrow ROOOH + SROOOH \quad \text{(SXIII)}$$

$$ROOOH + OH \rightarrow IEPOX + HO_2 + H_2O \quad \text{(SXIV)}$$

$$ROOOH + \Delta \rightarrow RO + HO_2 \quad \text{(SXV)}$$

$$ROOOH + h\nu \rightarrow RO + HO_2 \quad \text{(SXVI)}$$

S2.3. Discussion of the modeling results

The modeled annual vertical average concentrations of isoprene, OH radicals and ROOOH within the lowest 5 model layers along with the modeled emission of isoprene is shown in Fig. S24. The simulation shows that the consideration of the thermal decomposition ROOOH has almost no effect on the modelled OH concentrations (Fig. S24 C and D). However, the modelled concentration of ROOOH is strongly dependent on the thermal decomposition, resulting in about an order of magnitude lower ROOOH concentrations when this reaction pathways is considered (Fig. S24 E and F). Furthermore, the simulations with $k_{RO2+OH} = 5.1 \times 10^{-11}$ cm^3 $molecules^{-1}$ s^{-1} indicate that the reaction of RO_2 with OH radicals accounts globally for about 0.57 % of the fate of RO_2 radicals derived from isoprene oxidation (Fig. S25). With the higher reaction rate coefficient of $k_{RO2+OH} = 1.1 \times 10^{-10}$ cm^3 $molecules^{-1}$ s^{-1} (see main text) the contribution increases to about 1%.

In accordance to some other global chemistry models (*61*), low OH radical concentrations are modeled in the Amazon Basin. Performed comparisons with OH radical measurements revealed that the model predictions can be realistic there. The modeled monthly maximum values of the OH radical are about 1×10^6 molecules cm^{-3} for February and March which agrees with previously reported observations in 2014 by Jeong *et al.* (*62*).

To investigate the effect of the new reaction pathways on the atmospheric chemical composition, a simulation with the original mechanism (DEFAULT) was carried out and compared with the two other performed

simulations for isoprene-related ROOOH chemistry (with and without the thermal ROOOH decomposition included). On an annual average, the newly included ROOOH chemistry has a quantitative impact on IEPOX production mainly between 30°N and 30°S (see Fig. S26 A and B). The modeled deviation in the source regions can reach up to 3 % compared to the DEFAULT simulation (Fig. S26 C and D). The global annual average IEPOX concentration decreased by -0.4 % or increased by 0.9 % within the lowest 5 model layers for the simulation with and without consideration of thermal ROOOH decomposition, respectively.

Due to the advection of ROOOH and its role as possible HO_x reservoir, the concentration budget of H_2O_2, an important atmospheric oxidant, can be affected. In Fig. S26 E and F, we show that the annual average deviations of H_2O_2 that can reach about 5 % in the trade wind regime within the lowest 5 model layers for both the simulation with and without consideration of thermal ROOOH decomposition. The calculations and comparisons with the DEFAULT simulation suggest that the added ROOOH reaction pathways can affect linked chemical subsystems. On regional scales, a contribution of the reaction between RO_2 + OH even below 1% to the overall RO_2 sinks can impact the H_2O_2 budget and the overall yields of key products such as IEPOX to a somewhat bigger extent.

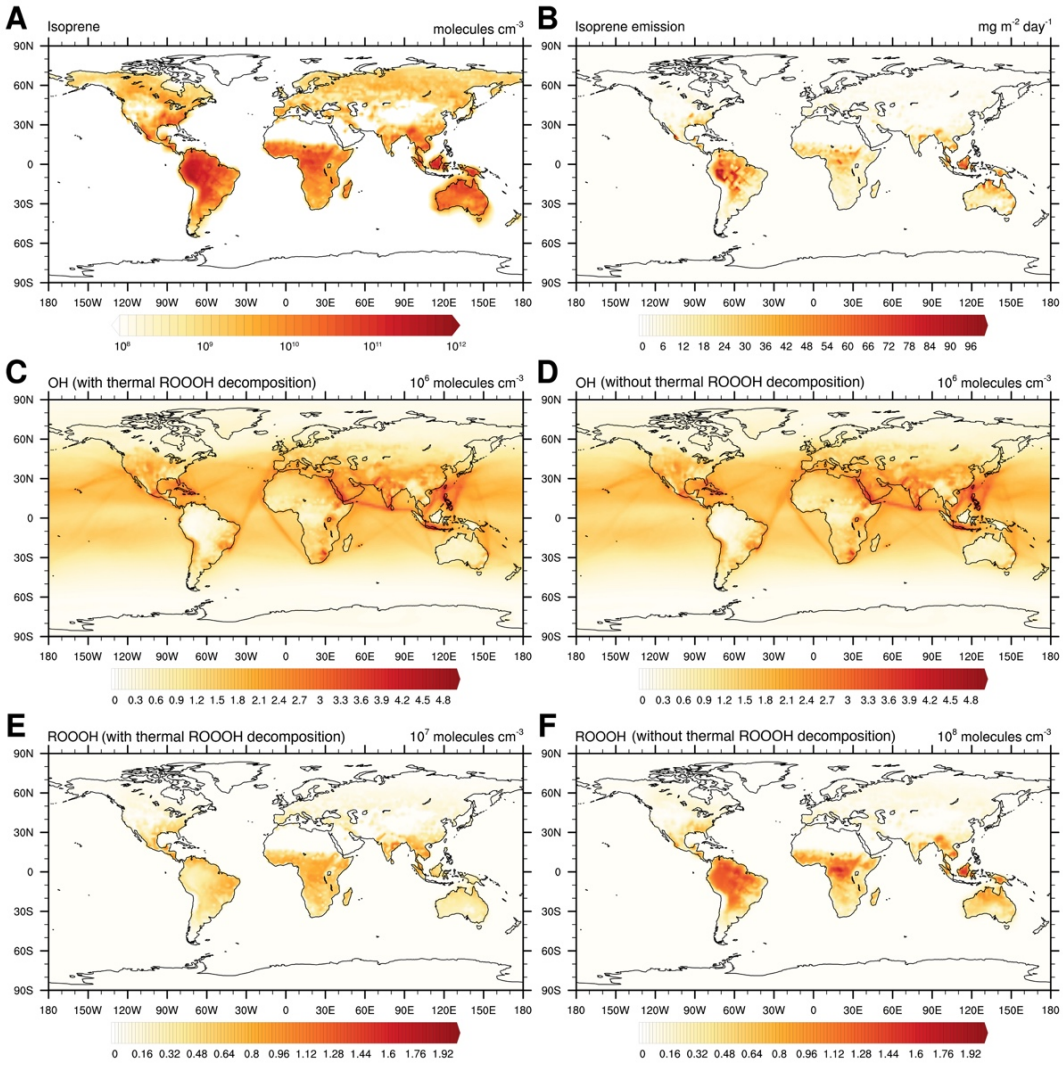

Fig. S24: Annual vertical average concentrations of isoprene, OH radicals and ROOOH in the simulation within the lowest 5 model layers (corresponds to an average altitude of about 900-1200 m above the ground). A: Modeled concentration (in molecules cm^{-3}) of isoprene. B: Modeled emission (in mg m^{-3} day^{-1}) of isoprene. C: Modeled concentration (in molecules cm^{-3}) of OH radicals for the simulation with thermal ROOOH decomposition. D: Modeled concentration (in molecules cm^{-3}) of OH radicals for the simulation without thermal ROOOH decomposition. E: Modeled concentration (in molecules cm^{-3}) of ROOOH from isoprene oxidation for the simulation with thermal ROOOH decomposition. F: Modeled concentration (in molecules cm^{-3}) of ROOOH from isoprene oxidation for the simulation without thermal ROOOH decomposition. The applied k_{RO2+OH} reaction rate coefficient in the simulations was 5.1×10^{-11} cm^3 $molecules^{-1}$ s^{-1} for reaction (S1).

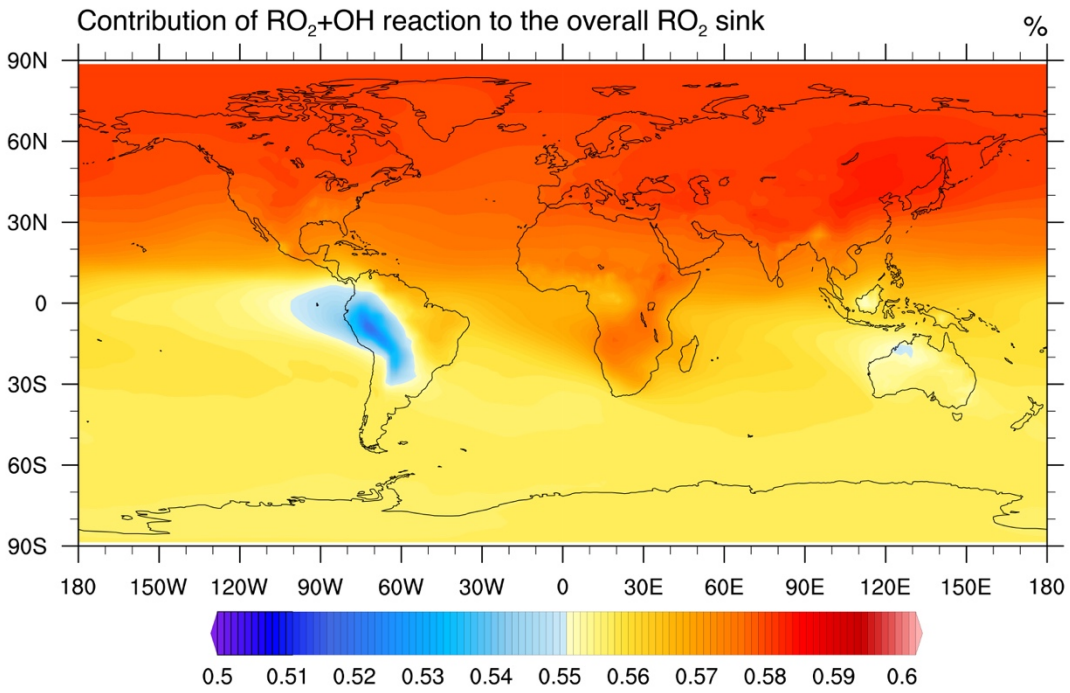

Fig. S25: Annual vertical average contribution (%) of the reaction between the isoprene-derived RO_2 radicals with the OH radical to the total RO_2 sink. Contribution was calculated for the simulation with thermal ROOOH decomposition, however similar results are obtained without thermal ROOOH decomposition. The applied k_{RO2+OH} reaction rate coefficient in the simulations was 5.1×10^{-11} cm^3 $molecule^{-1}$ s^{-1}.

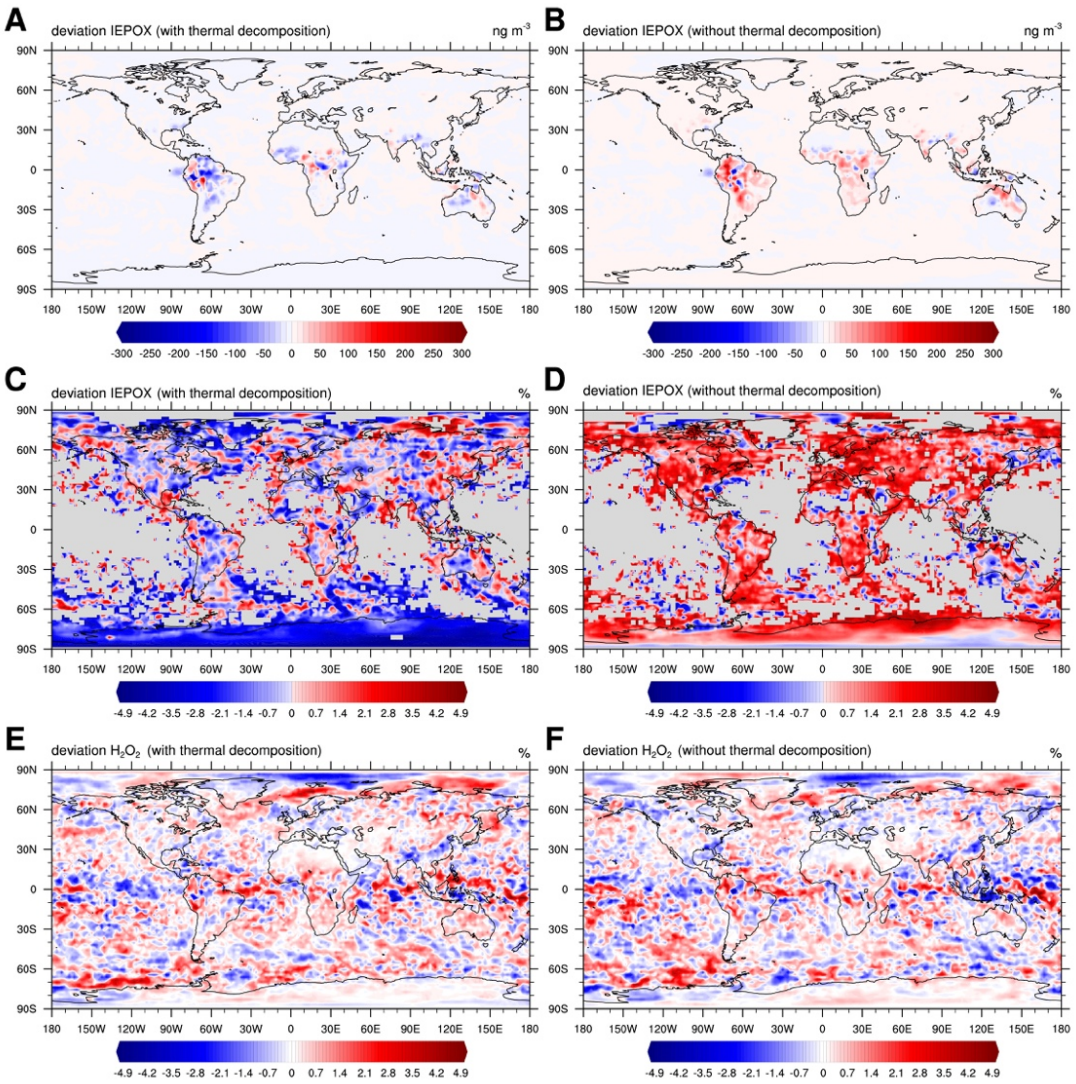

Fig. S26: Annual vertical average of the modeled IEPOX concentration difference as well as the H_2O_2 concentration difference between the DEFAULT simulation and the simulation with and without thermal ROOOH decomposition within the lowest 5 model layers (corresponds to an average altitude of about 900-1200 m above the ground). A: Modeled deviation in concentration (in ng m^{-3}) of IEPOX between the simulation with thermal ROOOH decomposition and the DEFAULT simulation. B: Modeled deviation in concentration (in ng m^{-3}) of IEPOX between the simulation without thermal ROOOH decomposition and the DEFAULT simulation. C: Modeled percentage difference in the concentration of IEPOX for the simulation with thermal ROOOH decomposition and the DEFAULT simulation. D: Modeled percentage difference in the concentration of IEPOX for the simulation without thermal ROOOH decomposition and the DEFAULT simulation. In panel C and D, values below or above 5 % are shaded by gray color for clarity. E: Modeled percentage difference in concentration of H_2O_2 for the simulation with thermal ROOOH decomposition and the DEFAULT simulation. F: Modeled percentage difference in concentration of H_2O_2 for the simulation without

thermal ROOOH decomposition and the DEFAULT simulation. The applied reaction rate coefficient in the simulations was 5.1×10^{-11} cm^3 $molecules^{-1}$ s^{-1} for reaction (S1). The deviations were calculated by subtracting the modeled concentrations from the simulations with included ROOOH chemistry by the DEFAULT simulation. The percentage differences were calculated by dividing deviations by the concentration of the DEFAULT simulation.

S3. Hydrotrioxide formation mechanisms

Signals consistent with hydrotrioxide (ROOOH) formation have been observed in two different experimental setups from different parent molecules. For some, the experimentally measured mass may correspond to different isomers. In this section, we show proposed formation mechanisms of hydrotrioxides corresponding to the experimentally observed signals from the reactions of OH radicals with trimethylamine (TMA), isoprene, α-pinene, dimethyl sulfide (DMS), 1-butene, and 2-methylpropene. Most mechanisms show only the dominant oxidation pathways for simplicity. The ROOOHs match the experimentally observed masses are marked in red. The ROOOHs with a mass that was not experimentally detected are marked in light gray. The ROOOHs that have been further studied theoretically (see Section S4) are marked in a solid box. A hydrogen migration (isomerization) that spans n nonhydrogen atoms is referred to as 1,n H-shift. A cyclization reaction that forms a n-membered ring is referred to as a n-cyc.

Trimethylamine (TMA)

The hydrotrioxide formation mechanism following the OH + TMA reaction is shown in Fig. S27. The reaction rate coefficients for the three unimolecular 1,5 H-shift reactions are adopted from a previous study using multi-conformer transition state theory (MC-TST) at the ROCCSD(T)-F12a/VDZ-F12 level. (*12*) The first and second 1,5 H-shift reactions are about a factor of 60 and 10 faster than the last 1,5 H-shift. We only observed the signal corresponding to the last generation ROOOH (Fig. S27, red) in our experiments. The ROOOH formation from the first two generation RO_2 radicals (Fig. S27, gray) cannot compete with the fast H-shift reactions. With the steady-state OH radical concentrations of about $5 \times 10^6 - 7 \times 10^7$ molecules cm^{-3} under the TROPOS experimental conditions and the RO_2 + OH reaction rate coefficient of about 10^{-10} cm^3 $molecule^{-1}$ s^{-1}, we estimated the pseudo first-order rate coefficient of the RO_2 + OH reaction, $k' = k_{RO_2+OH} \times [OH]$, to be about 0.0005 – 0.007 s^{-1}.

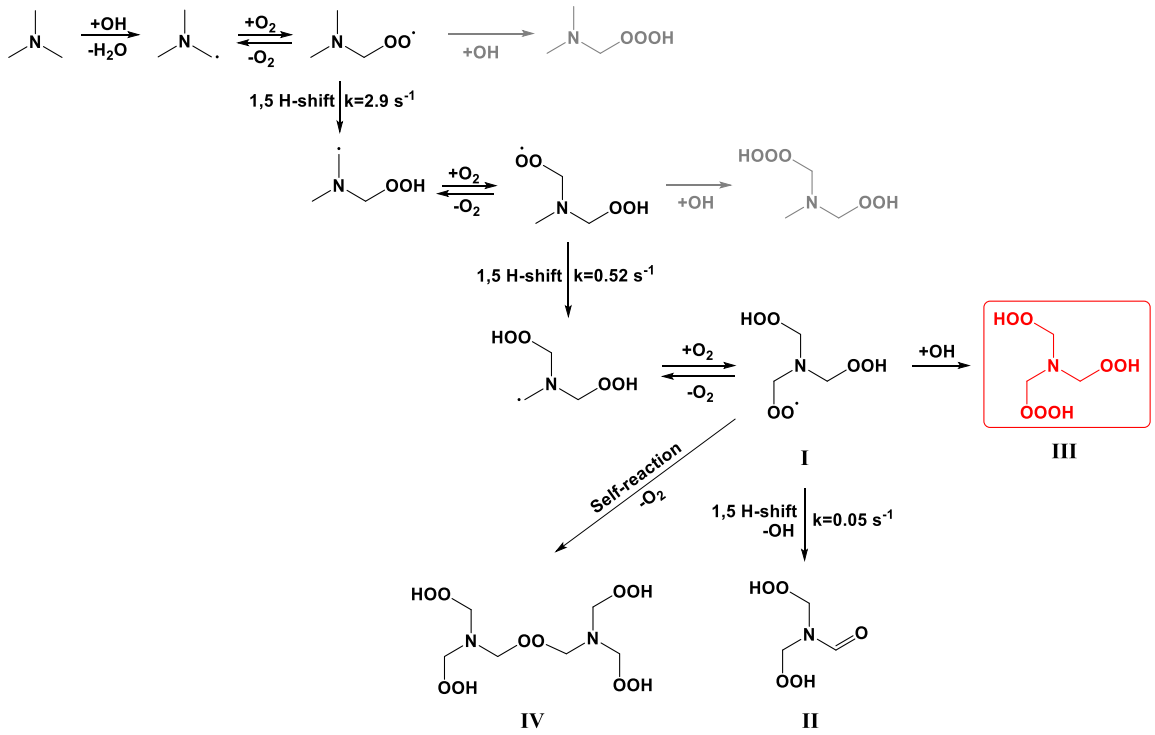

Fig. S27. Hydrotrioxide formation from the OH + TMA reaction. The ROOOH observed in our experiment is marked in red and labelled **III**. Compounds marked **I**, **II** and **IV** are also observed in the experiment (Fig. **1**).

Isoprene

The possible first-generation hydrotrioxide formation mechanism from 1,2 addition in the OH + isoprene reaction is shown in Fig. S28. The *cis* structure of 1,4 addition (Fig. S28) leads to higher oxidized RO_2 radicals after a 1,6 H-shift and subsequent reactions (Fig. S29). The 1,6 H-shift reaction rate coefficient of 0.4 s^{-1} in Fig. S28 is adopted from a previous experimental study. (*63*)

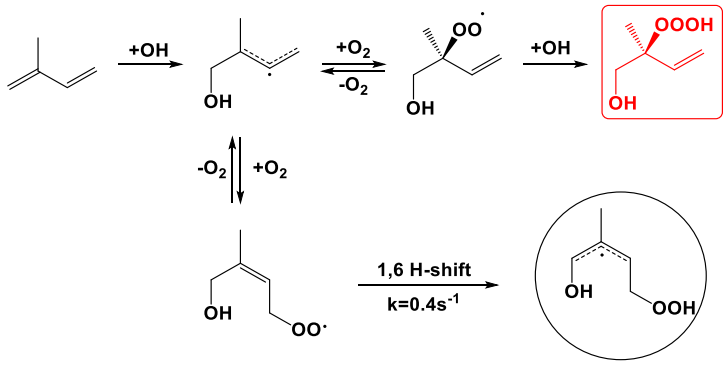

Fig. S28. First-generation hydrotrioxide ($HO\text{-}C_5H_8OOOH$) formation from OH + isoprene. A likely structure of the $HO\text{-}C_5H_8OOOH$ observed in our experiment is marked in red Fig. 2. Other competing RO_2 formations and subsequent radical reactions are not shown for simplicity. Possible subsequent reactions of the alkyl radical in the circle are shown in Fig. S29.

The possible second-generation hydrotrioxide formation mechanism following the OH + isoprene reaction is shown in Fig. S29 (*22*). The 1.6 enolic H-shift reaction rate coefficient of 10^6 s^{-1} in Fig. S29 is adopted from previous theoretical calculations (*64*) and the two rate coefficients of the 1,4 H-shift with HO_2 loss ($k > 10^2$ s^{-1}) are estimated based on existing experimental and theoretical studies. (*65, 66*) Considering these fast loss rates of the RO_2 radicals formed through the top, bottom and right O_2 addition channels, the RO_2 formed through the O_2 addition channel on the left side is likely to have the longest lifetime, thus leading to ROOOH formation. The 1,6 H-shift between the two peroxy groups (Fig. S29, green) is known to be very fast and the equilibrium is reached within 10^{-4} s. (*14*) We have performed conformer sampling (see Section S4.1) and calculated the relative energy of the two RO_2 radicals marked in green in Fig. S29 at the M06-2X/aug-cc-pVTZ level. The lowest energy conformer of the RO_2 radical on the right is about 1 kcal mol^{-1} more stable than the one on the left, thus the ROOOH formation from the RO_2 radical on the right is likely to contribute more to the experimentally observed signal of $HO\text{-}C_5H_8(O_2)OOOH$ (see Fig. 3 in the main text).

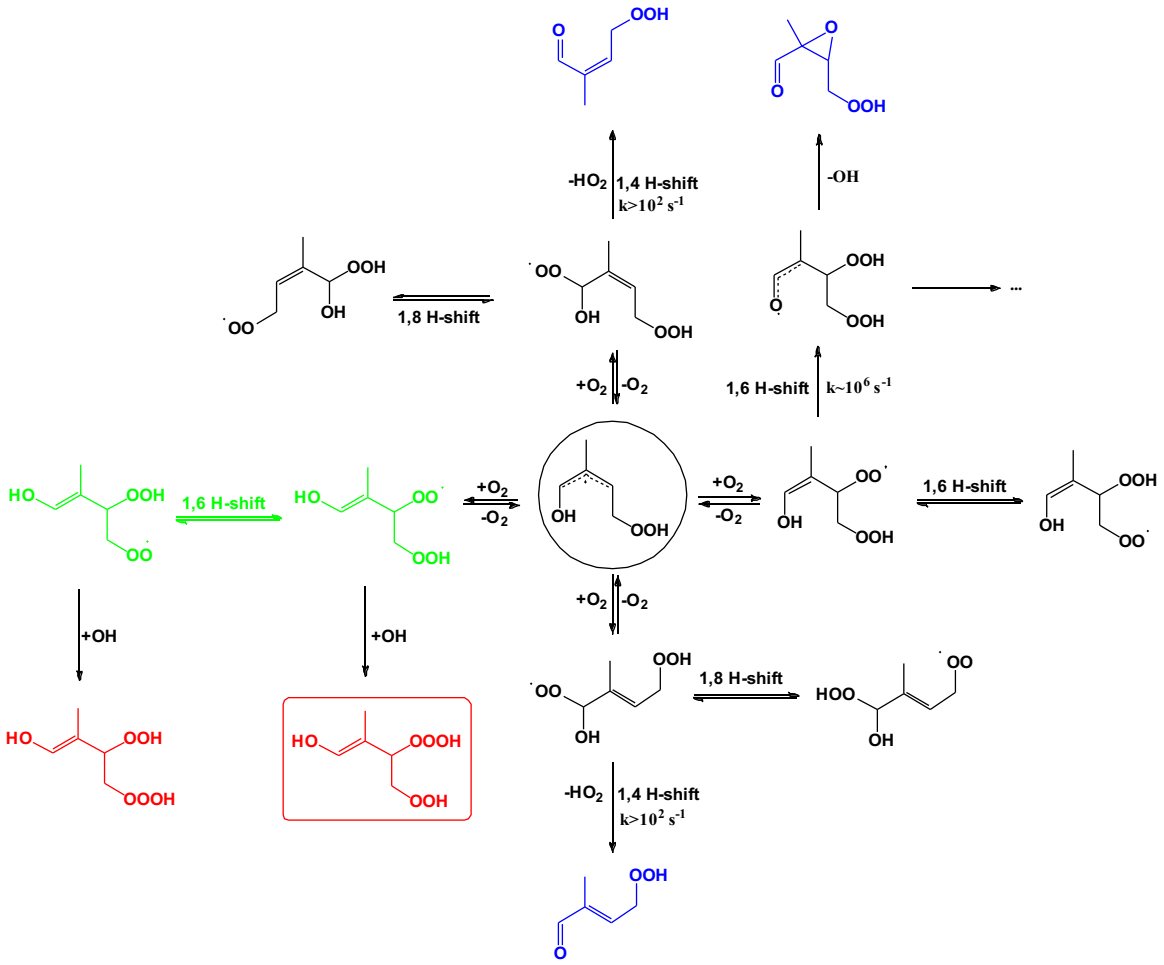

Fig. S29. Second-generation hydrotrioxide (HO-$C_5H_8(O_2)OOOH$) formation from OH + isoprene. The radical in the circle is the same radical given in Fig. S28. The closed-shell products in blue have previously been observed experimentally (*11*). The RO_2 formed through the O_2 addition channel on the left (green) likely has the longest lifetime, thus most likely forming the observed ROOOH by OH addition. The most likely structures of HO-$C_5H_8(O_2)OOOH$ observed in our experiment are marked in red. Other competing RO_2 radical reactions are not shown for simplicity.

α-Pinene

The possible hydrotrioxide formation mechanism from the OH-addition channel of the OH + α-pinene reaction is shown in Fig. S30. The 1,5 H-shift and 1,6 H-shift reaction rate coefficients are adopted from previous theoretical studies. (*67, 68*) The rate coefficient for the 6-cyclization (forming a 6-membered ring) reaction is estimated from a similar reaction. (*67*) The rate coefficient of the 1,4-H shift with HO_2 loss (Fig. S30, blue) is estimated based on previous experimental and theoretical studies. (*65, 66*) The first-generation hydrotrioxides HO-$C_{10}H_{16}$OOOH have 4 possible stereoisomers and only one of them is shown. No significant signal of the corresponding second-generation HO-$C_{10}H_{16}(O_2)$OOOH (Fig. S30, gray) is observed in our experiment due to the relatively high background at its expected mass and the generally low hydrotrioxide concentrations in the experiments. The third generation hydrotrioxides HO-$C_{10}H_{16}(O_2)_2$-OOOH have 8 possible stereoisomers and only the lowest energy isomer calculated at the B3LYP/6-31+G(d) level is shown and further studied.

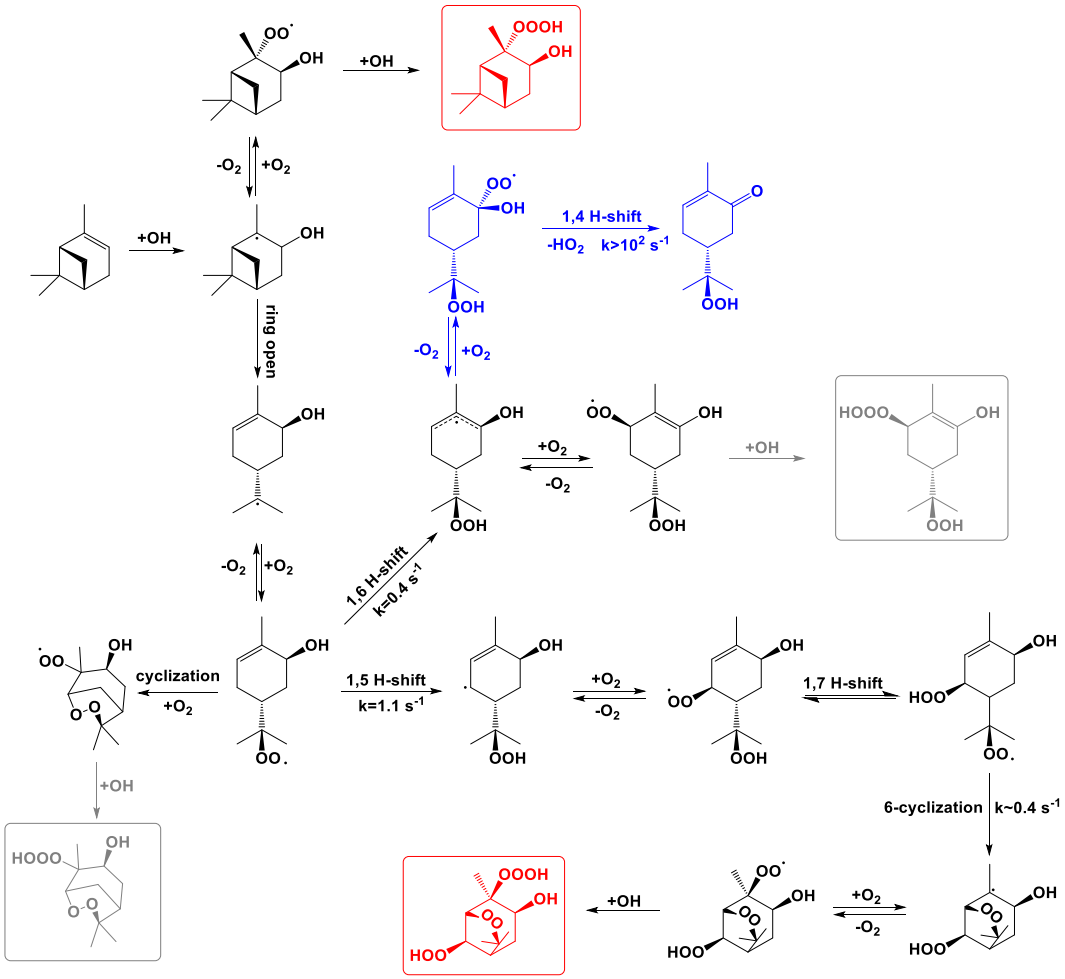

Fig. S30. Hydrotrioxide formation from OH + α-pinene. The likely structure of the first and third generation ROOOH observed in our experiment are marked in red. Other competing RO_2 radical reactions are not shown for simplicity.

Dimethyl sulfide (DMS)

The hydrotrioxide $HOOCH_2SCH_2OOOH$ formation mechanism from the OH + DMS H-abstraction channel is shown in

Fig. **S31**. The two 1,5 H-shift rate coefficients are theoretical values adopted from a previous study. (*12*) The theoretical rate coefficient of the first 1,5 H-shift reaction in $CH_3SCH_2O_2$ (0.06 s^{-1} at 298.15 K) is in reasonable agreement with the experimental values of 0.23 ± 0.12 s^{-1} at 295 ± 2 K (*48*) and about 0.09 s^{-1} (0.03 - 0.3 s^{-1}, $1\sigma_g$, geometric standard deviation) at 293 K. (*69*) The experimentally observed $HOOCH_2SCH_2OOOH$ signal strength at the highest OH radical concentration, with [OH] ~7 × 10^7 molecules cm^{-3}, is about 1/100 of the signal strength of $HOOCH_2SCHO$ representing the closed-shell product of the second 1,5 H-shift reaction, see

Fig. **S31**. This product ratio is in general agreement with the ratio between the calculated rate coefficient of the second 1,5 H-shift (0.58 s^{-1}) and the estimated pseudo-first-order ROOOH formation rate coefficient $k(RO_2+OH)$ × [OH] of ~ 0.007 s^{-1} assuming $k(RO_2+OH)$ ~10^{-10} cm^3 $molecule^{-1}$ s^{-1}. A signal of the possible CH_3SCH_2OOOH was not observed, likely due to the expected low detection sensitivity of this product.

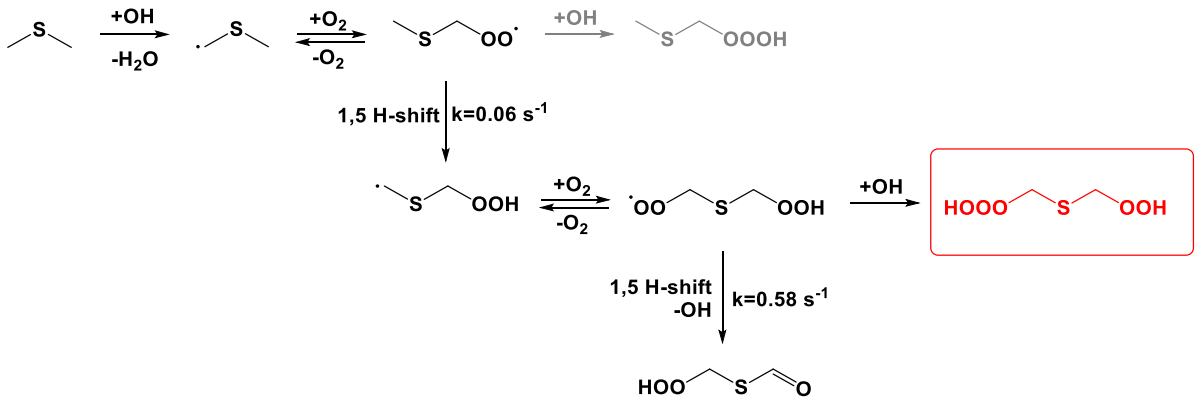

Fig. S31. Hydrotrioxide formation from the OH + DMS hydrogen abstraction channel.

1-Butene

The dominant hydrotrioxide formation mechanism of HO-C_4H_8OOOH from the OH + 1-butene addition channel is shown in Fig. S32. The corresponding signal of the hydrotrioxide HO-C_4H_8OOOH is observed in our experiment.

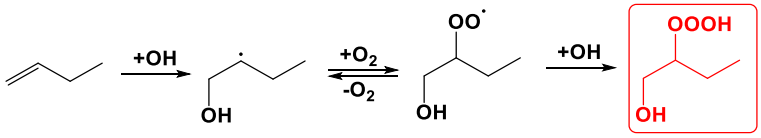

Fig. S32. Hydrotrioxide formation from the OH + 1-butene reaction.

2-Methylpropene

The hydrotrioxide formation mechanism of HO-$CH_2C(CH_3)_2OOOH$ from the OH + 2-methylpropene reaction with OH attack in terminal position is shown in Fig. S33. This ROOOH (Fig. S33, red) is observed in the Caltech experimental setup (see section S1.7). The rate coefficients for the three possible unimolecular reactions of the peroxy radical HO-$CH_2C(CH_3)_2OO$ have been calculated theoretically to be smaller than 10^{-4} s^{-1}. (*70*) Under the Caltech experimental condition with an OH concentration of about 10^7 molecule cm^{-3}, these slow unimolecular reactions cannot compete with the OH addition reaction (assuming k(RO_2+OH) ~10^{-10} cm^3 $molecule^{-1}$ s^{-1}), and the ROOOH formation route is dominant.

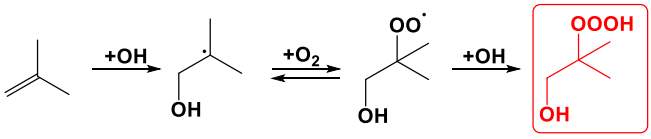

Fig. S33. Hydrotrioxide formation from the OH + 2-methylpropene reaction. The hydrotrioxide HO-$CH_2C(CH_3)_2OOOH$ was observed in the Caltech experiments as described in section S1.7.

S4. Computational details

S4.1. Conformer sampling

The formation and decomposition energy of selected hydrotrioxides is calculated from the relative energy between the reactant RO_2 + OH, the ROOOH, and the decomposition products RO + HO_2 (see Fig. 2 in the main text). A conformer sampling process has been carried out to ensure the lowest energy conformer is found for each RO, RO_2, and ROOOH for calculation of these energies.

The conformer sampling is based on the procedure described previously. (*71*) Briefly, conformers are generated by rotating each dihedral angle in the structure 3 times and 120° each time. The generated conformers are pre-optimized in Spartan'18 using MMFF. (*72, 73*) For radicals, a neutral charge was enforced on the radical atom. The obtained conformers are then optimized at the B3LYP /6-31+G(d) level in Gaussian 16, rev. C01. (*74*) Conformers with a zero-point vibrational corrected electronic energy (E+ZPVE) more than 2 kcal mol^{-1} above the lowest energy conformer were excluded from further calculations. The conformers within the 2 kcal mol^{-1} cut-off were subsequently optimized at the M06-2X /aug-cc-pVTZ level (referred to as M06-2X) and the ωB97X-D /aug-cc-pVTZ level (referred to as ωB97X-D).

The conformers with the lowest zero-point vibrational corrected electronic energies (E+ZPVE) calculated at the M06-2X level are shown in Table S2. The conformer geometries calculated at the ωB97X-D level are nearly identical to the ones obtained from the M06-2X level calculations.

Table S2. The lowest energy (electronic + ZPVE) conformers of each ROOOH and the corresponding ROO and RO radicals optimized at the M06-2X/aug-cc-pVTZ level.

Hydrotrioxide	Lowest energy conformer		
	ROO	ROOOH	RO
HOOH	-	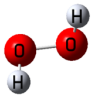	
HOOOH	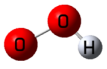	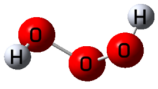	
CH_3OOOH	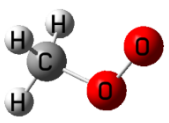	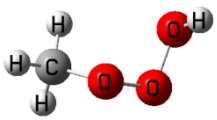	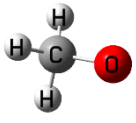

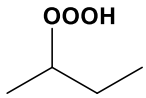 OOOH	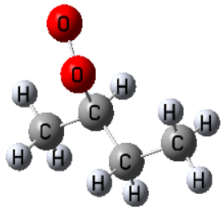	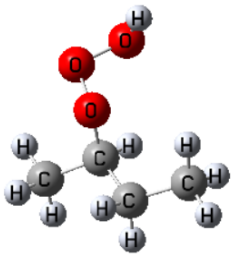	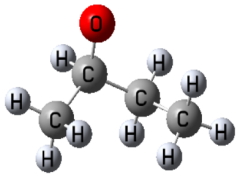
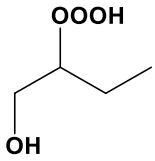 OOOH OH	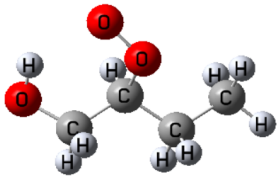	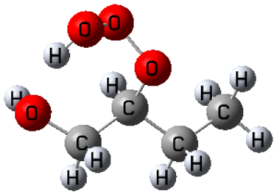	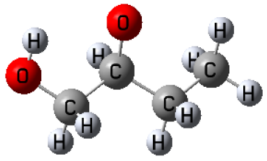
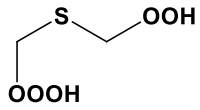 S OOH OOOH	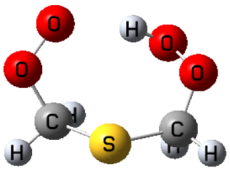	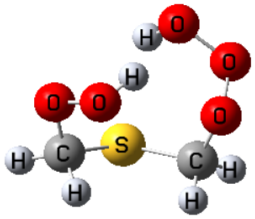	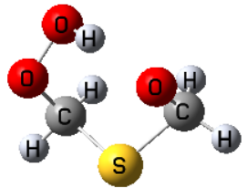
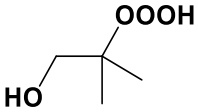 OOOH HO	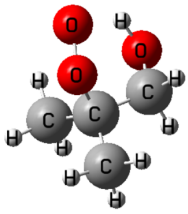	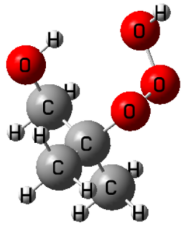	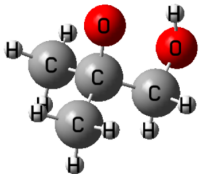
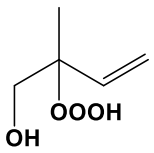 OOOH OH	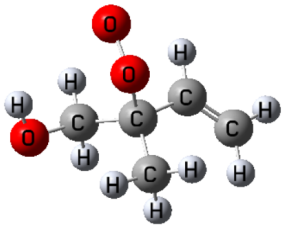	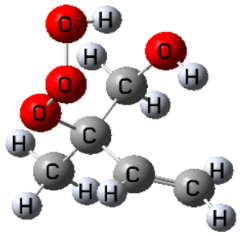	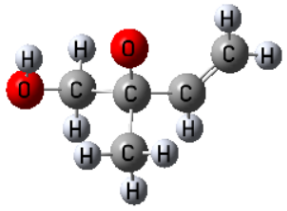
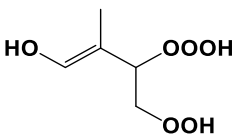 HO OOOH OOH	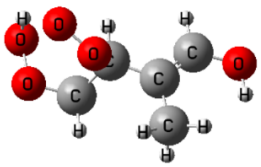	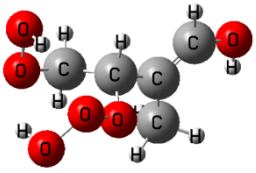	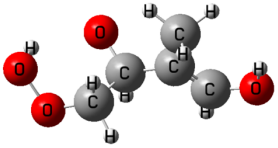

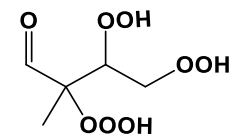 O OOH OOH OOOH	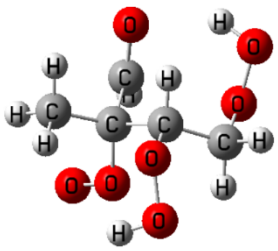	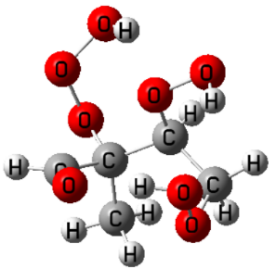	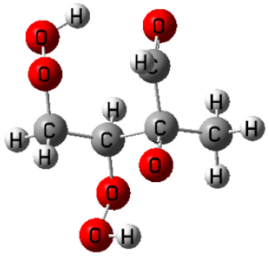
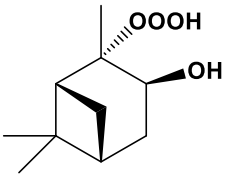 OOOH OH	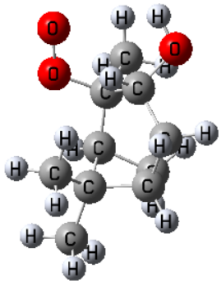	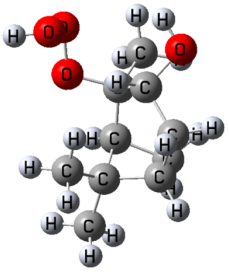	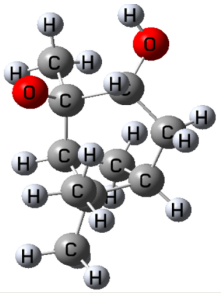
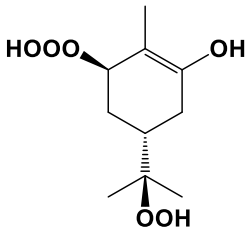 HOOO OH OOH	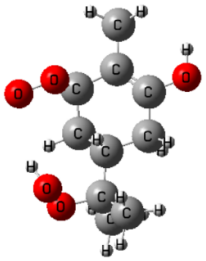	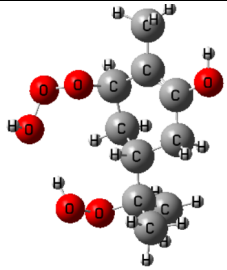	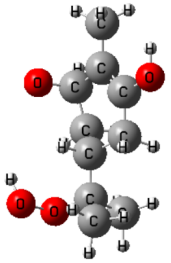
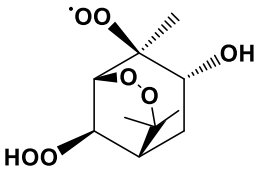 OO OH O O HOO	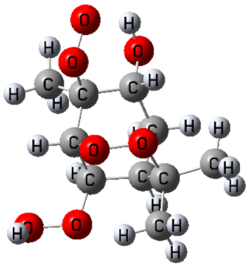	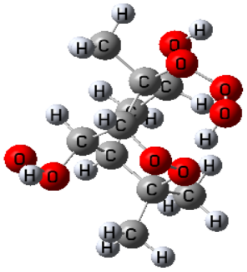	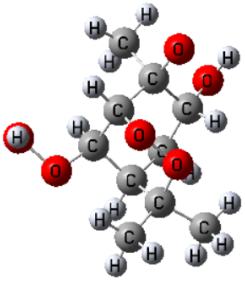
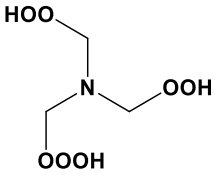 HOO N OOH OOOH	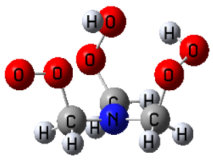	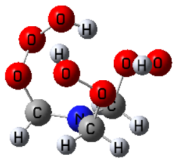	

S4.2. Thermal stability of hydrotrioxides

The accuracy of the results from a calculation depends on both the reliability of the method and the quality of the basis set. We want to calculate the formation and decomposition energies of the hydrotrioxides, which involves a peroxy radical (RO_2), the hydroxyl radical (OH), an alkoxy radical (RO), the hydroperoxyl radical (HO_2), and the hydrotrioxide (ROOOH) itself. These radical species are difficult to describe accurately at a relatively low level of theory, and no systematic computational tests have been reported for hydrotrioxides. More importantly, the formation and decomposition of the hydrotrioxide both involve two radicals. The process of two radicals combining to form a closed-shell product, or reversely, the breaking of a covalent bond in a closed-shell molecule forming two radicals is known to be spin-entangled. (*75*) For such a system, the regular single reference methods based on only one slater-determinant are known to fail and multi-reference methods are needed. (*76*) However, the multi-reference methods are generally computational-resource demanding which greatly limits the size of the systems that can be studied with those methods.

Therefore, we first tested the basis set convergence of the species involve in the formation and decomposition of CH_3OOOH and showed that the reaction energies are reasonably converged with the aug-cc-pVTZ basis set. Secondly, we studied the dissociation process of three small systems (HOOH, HOOOH, and CH_3OOOH) using the multireference configuration interaction (MRCI) (*77*) and complete active space second-order perturbation theory (CASPT2) (*78*). We found that the reaction barrier, $E_a=E_{TS}-E_{ROOOH}$, calculated from the transition state and reactant, is very close to the decomposition energy, $E_d=E_{RO}+E_{HO2}-E_{ROOOH}$, calculated from the energy difference between the reactant and the products. Subsequently, the multireference decomposition energies, E_d, are compared to those calculated with the single reference methods, e.g., density functional theory (DFT) and coupled cluster (CC), to estimate the uncertainty of these methods, which are applicable to the larger species studied here. Finally, the decomposition energies for the larger atmospheric relevant hydrotrioxides are calculated at the DFT and, when possible, CC levels.

Complete basis set limit extrapolation

We calculated the energy of the species involved in the formation and decomposition of CH_3OOOH at the UCCSD(T) level using three basis sets with increasing order of ζ (Fig. S34). From that, we have extrapolated the decomposition energy of CH_3OOOH to the complete basis set (CBS) limit (

Table **S3**). Point energies on the UCCSD(T)/aug-cc-pVTZ optimized geometry was calculated with the aug-cc-pVDZ, aug-cc-pVTZ and aug-cc-pVQZ basis set at the UCCSD(T) level of theory, and the obtained energies were fit to the equation:

$$E = E_\infty + Be^{-\alpha\zeta} \quad \text{(SXVII)}$$

Where E is the energy calculated with aug-cc-pVDZ (ζ=2), aug-cc-pVTZ (ζ=3) and aug-cc-pVQZ (ζ=4) basis sets, E_∞ obtained from the fit is the energy at CBS limit, and B and α are the fitting parameters.

As expected, the absolute energy of each species (CH_3O, CH_3OO, CH_3OOOH, OH and OOH) decreases with the increasing basis set. The energy of a larger species decreases more rapidly. The decomposition energy ($E_d=E_{OOH} + E_{CH3O} - E_{CH3OOOH}$) increases with the increasing basis set, however, the effect is minor from aug-cc-pVTZ to aug-cc-pVQZ. (Fig. S34).

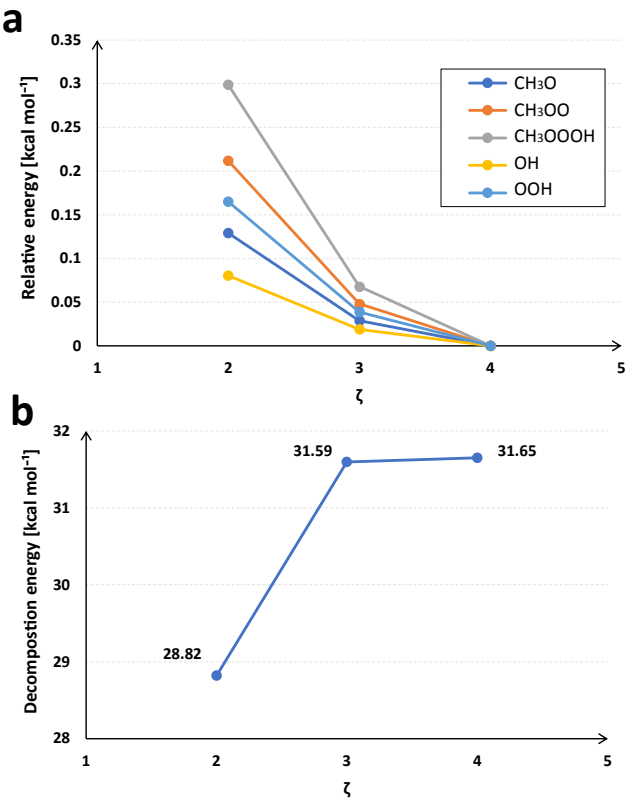

Fig. S34. Basis set convergence of (a) the energy of different species and (b) the decomposition energy for CH_3COOOH.

The CBS fitting results for the different species are shown in

Table **S3**. The decomposition energy, E_d, increases by about 2.8 kcal mol^{-1} with the increase of ζ from 2 to 3. Further increasing ζ to 4 only leads to an increase of E_d by about 0.06 kcal mol^{-1}. The E_d calculated from the CBS limit is almost identical to the ζ=4 result and thus only about 0.06 kcal mol^{-1} higher than the ζ=3 result. Therefore, the aug-cc-pVTZ (ζ=3) basis is used in the following study.

Table S3. The absolute energies (E in a.u.) and decomposition energies (E_d in kcal mol^{-1}) calculated at the UCCSD(T) level.

	CH_3O	CH_3OO	CH_3OOOH	OH	OOH	E_d
E(ζ=2)	-114.784688	-189.797525	-265.430565	-75.583974	-150.599941	28.8242
E(ζ=3)	-114.885101	-189.961205	-265.661623	-75.645537	-150.726172	31.5946
E(ζ=4)	-114.913929	-190.009271	-265.729507	-75.664450	-150.765138	31.6512
E(CBS)	-114.913948	-190.009303	-265.729552	-75.664463	-150.765166	31.6505
B (a.u.)	1.7085	2.6868	3.7910	0.9420	1.9159	-
α	1.2478	1.2253	1.2249	1.1805	1.1753	

Multireference calculations

The multireference calculations were performed using the MOLPRO2020.1 package. (*79*) The geometries were first optimized at the CASSCF level, then an MRCI or CASPT2 level single point calculation was performed on the CASSCF level geometry using the CASSCF orbitals. For the CASSCF level optimized stationary points, frequency analysis was also performed to ensure the optimized stationary points are real minima or TSs on the potential surface. During the CASSCF calculations, the orbital coefficients of the core orbitals were also optimized (no frozen core approximation). For the subsequent single point MRCI and CASPT2 calculations, the same active space as for the CASSCF calculations was used. For the MRCI calculations, the orbitals in the active space are fully correlated (full-CI) and the orbitals outside the active space are correlated by only single and double excitations (MRCISD). The RS2C keyword is used for the CASPT2 calculations. (*77*) The multireference calculations are compared with the CC calculations. The unrestricted coupled-cluster method with iterative inclusion of single and double excitations and perturbative inclusion of triple excitations [UCCSD(T)] level energies are calculated by doing both geometries optimizations and frequency analysis at the same level. All calculations were performed with the aug-cc-pVTZ basis set. Energies in this section refer to electronic energies unless otherwise stated.

The calculated dissociation potential of HOOH → 2OH is shown in Fig. S35. The geometry of HOOH was optimized at the full valence [14e,10o]-CASSCF/aug-cc-pVTZ level followed by frequency analysis. Subsequently, we performed a CASSCF level relaxed scan of the O-O bond length from the equilibrium length of 1.48 Å to 5.08 Å with a step size of 0.20 Å (Fig. S35, green line). The saddle point on the dissociation surface was found at an O-O distance of 2.88 Å, which was further optimized as a transition state (i140.5 cm^{-1}) at the same level and marked with a green square. The depression at 3.28 Å on the dissociation surface corresponds to the formation of an OH-OH hydrogen-bonded complex. The MRCI and CASPT2 calculations are single-point

calculations on the CASSCF optimized geometries with the same [14e,10o] active space (Fig. S35, gray and orange). The MRCI level reaction barrier, E_a=E_{TS}-E_{HOOH}, is 49.3 kcal mol^{-1} and the CASPT2 reaction barrier is 1.6 kcal mol^{-1} lower than the MRCI value. The decomposition energy, E_d, is 51.9 kcal mol^{-1} and 49.3 kcal mol^{-1} calculated from the O-O distance at 5.08 Å at the MRCI and CASPT2 level, respectively. The values agree well with the UCCSD(T) level decomposition energy of 52.2 kcal mol^{-1} calculated by (2 × E_{OH}) - E_{HOOH}.

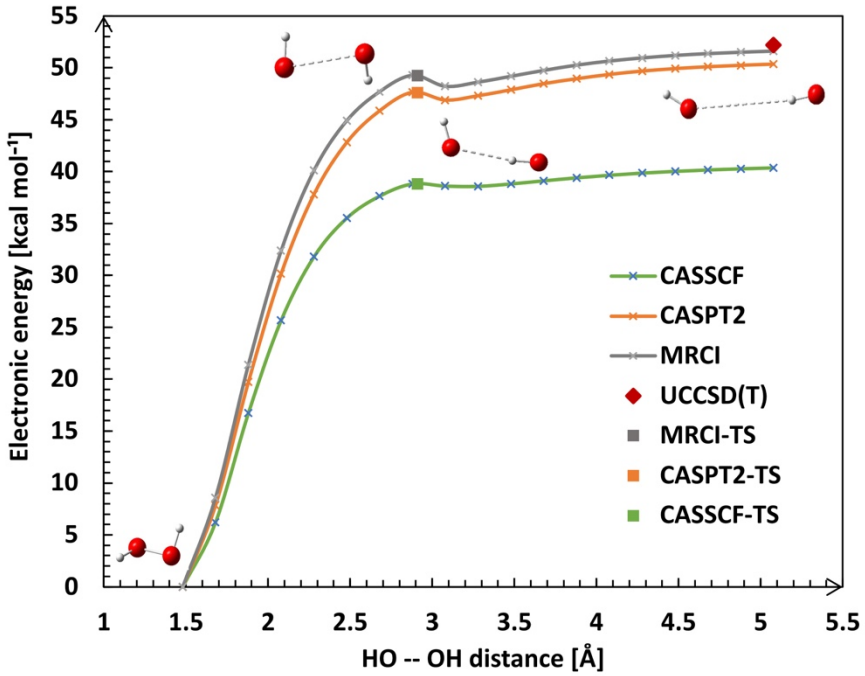

Fig. S35. The dissociation potential of HOOH calculated at the CASSCF, the MRCI, and the CASPT2 level with the aug-cc-pVTZ basis set. The full valence [14e, 10o] active space was used for all multireference calculations. The step size for the scan is 0.2 Å. Solid squares and diamond are described in the text.

The calculated dissociation potentials of HOOOH → HO + OOH are shown in Fig. S36. The calculations were performed in the same manner as for the HOOH dissociation and the full valence [20e,14o] active space for HOOOH was used. The CASSCF level TS was obtained at an O-O distance of 2.85 Å with an imaginary frequency of *i*134.5 cm^{-1} (Fig. S36, green square). Similar to the dissociation of HOOH, a depression at around 3 Å corresponding to the hydrogen-bonded product complex HO-HOO is observed for HOOOH dissociation. The reaction barrier, $E_a=E_{TS}-E_{HOOOH}$, is 32.2 kcal mol^{-1} at the MRCI level and 29.9 kcal mol^{-1} at the CASPT2 level. The decomposition energy calculated from the point at an O-O distance of 5.08 Å is 34.2 kcal mol^{-1} and 32.2 kcal mol^{-1} at the MRCI and CASPT2 level, respectively. The UCCSD(T) level decomposition energy is 35.5 kcal mol^{-1}.

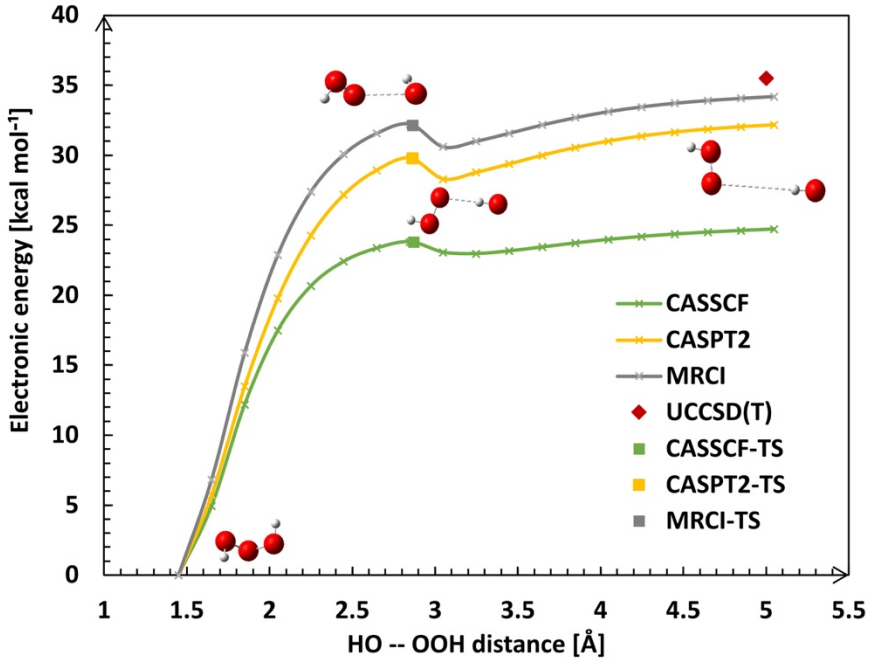

Fig. S36. The dissociation potential of HOOOH calculated at the CASSCF, the MRCI, and the CASPT2 level with the aug-cc-pVTZ basis set. The full valence [20e, 14o] active space was used for all multireference calculations. The step size for the scan is 0.2 Å. Solid squares and diamond are described in the text.

The calculated dissociation potential of CH_3OOOH → CH_3 + OOH is shown in Fig. S37. The full valence [26e,20o] active space calculation for CH_3OOOH cannot be achieved with our computational resources. Instead, the [14e,12o] active space which included all the p orbitals on the carbon and oxygen atoms is used. The TS is found at a O-O distance of 2.73 Å with an imaginary frequency of *i*192.17 cm^{-1}. The depression around 3 Å is,

again, the hydrogen-bonded complex formation between the dissociation products. The [14e,12o]-MRCI calculation is too memory consuming with our computational resources, thus only the [14e,12o]-CASPT2 single points were run. The reaction barrier, E_a, for CH_3OOOH at the CASPT2 level is 26.1 kcal mol^{-1} and the decomposition energy calculated from the point at an O-O distance of 7.03 Å is 28.3 kcal mol^{-1}. The decomposition energy calculated at the UCCSD(T) level is 2.3 kcal mol^{-1} higher than the CASPT2 value.

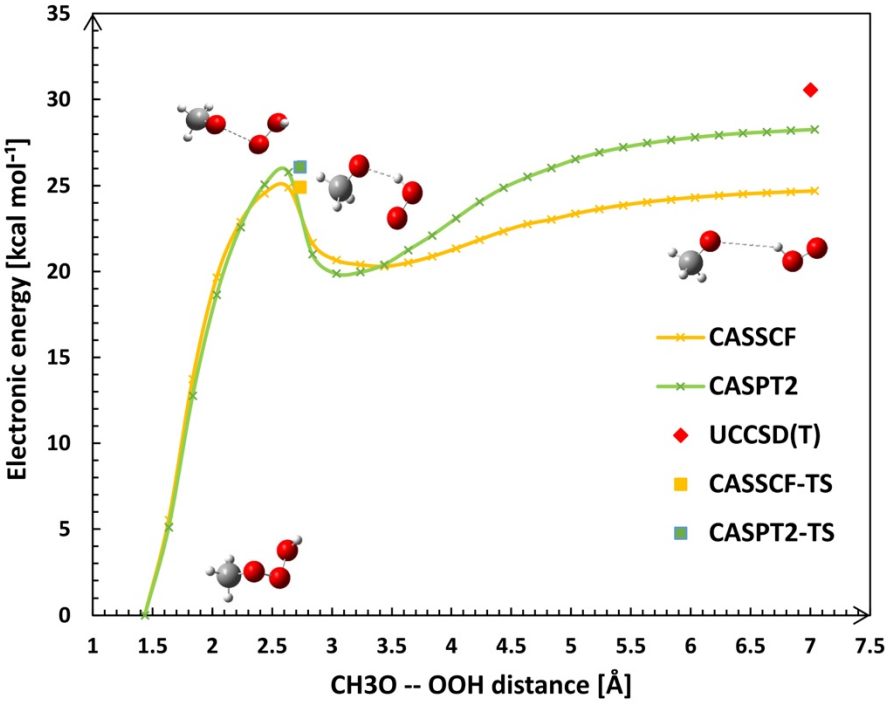

Fig. S37. The dissociation potential of CH_3OOOH calculated at the CASSCF, the MRCI, and the CASPT2 level with the aug-cc-pVTZ basis set. The [14e,12o] active space was used for all multireference calculations. The step size for the scan is 0.2 Å. Solid squares and diamond are described in the text.

Some overall trends can be observed for these three small test systems. First of all, the E_a and E_d values at the CASPT2 level are generally about 1-2 kcal mol^{-1} smaller than the values obtained at the MRCI level. We would consider the MRCI values more reliable than the CASPT2 ones, as the dynamic correlation energy at the CASPT2 level is obtained from the second order perturbation while the MRCI calculation we performed is a full CI in the active space and CISD for the other orbitals. Secondly, the decomposition energy, E_d, calculated at the MRCI from a finite (~5 Å) O-O distance is about 1-2 kcal mol^{-1} lower than the UCCSD(T) values. This difference is mainly due to the difference between the levels of theory and the incomplete dissociation at the MRCI potential surface. Finally, the difference between the reaction barrier, E_a, and the decomposition energy, E_d, obtained at the same level of theory is less than 2 kcal mol^{-1}. Therefore, by calculating the decomposition energy, it is

possible to estimate the reaction barrier and thus estimate the thermal stability of a hydrotrioxide. These tested small systems provide a valuable benchmark.

Comparison of different methods

We have shown that the decomposition energy calculated at the UCCSD(T) and MRCI levels are in reasonable agreement. However, the computational costs of UCCSD(T) and MRCI increases steeply with the system size and is not possible for the larger atmospherically relevant ROOOHs with our computational resources. Therefore, we performed a benchmark test including some of the most popular DFT methods as well as the explicitly correlated (F12) coupled-cluster approach which converges faster with basis set size than the CCSD(T) method. The results obtained at different levels are compared to the UCCSD(T) values. The UCCSD(T) level results are calculated with the geometries also optimized at the same level. The ROCCSD(T)-F12a (RF12) and UCCSD(T)-F12a (UF12) energies are single-point calculations performed on the M06-2X level optimized geometries. All DFT level energies are obtained with the geometry optimization at the corresponding level. For open shell systems, unrestricted DFT is used. The RF12 and UF12 calculations are performed with the VDZ-F12 basis set and the other level calculations are performed with the aug-cc-pVTZ basis set (aug-cc-pV(T+d)Z for S atom).

In Table S4, we show the differences in decomposition energy, E_d, calculated at different levels of theories compared to the UCCSD(T) results for 4 reactions. The DFT methods perform differently on different types of reactions. Most DFT methods overestimate the reaction barrier of H_2O_2 decomposition but underestimate the ROOOH decomposition energy, except for the two MN15 series functionals, which overestimated all decomposition energies. The functionals ωB97X-D, CAM-B3LYP, B3LYP, M11, and MN12-SX underestimate the ROOOH decomposition energy by roughly 6 kcal mol^{-1}. Among the tested DFT functionals, the M06-2X agrees with the UCCSD(T) result the best and the differences are within 1 kcal mol^{-1}. The results from the F12 methods generally agree with the UCCSD(T) results reasonably well, with the UF12 results slightly better than the RF12 as expected since we are benchmark against an unrestricted method.

Table S4. Calculated reaction barriers (electronic energies in kcal mol^{-1}) with different electronic structure methods compared with the UCCSD(T)/aug-cc-pVTZ (aVTZ) results for reactions i-iv shown below the table.

Method	Basis set	Reaction			
		i	ii	iii	iv
ωB97X-D	aVTZ	0.725	-2.435	-5.280	-3.432
M06-2X		1.773	0.383	-0.537	-0.452
M06		0.569	-0.688	-3.222	-1.389
MN15		4.011	2.127	0.537	1.489
MN15-L		2.002	3.386	2.018	3.013
CAM-B3LYP		-0.290	-2.855	-5.499	-4.084
B3LYP		-1.539	-3.837	-7.176	-5.201
M08-HX		2.306	0.030	-1.727	-0.711
M11		2.398	-0.596	-6.876	-5.869
MN12-SX		2.482	1.872	-4.100	-1.708
MRCI[a]		-0.603	-1.296	-	-
CASPT2[a]		-1.867	-3.328	-2.300	-
RF12//M06-2X	VDZ-F12	1.411	1.125	1.517	0.728
UF12//M06-2X		1.282	0.607	0.876	0.066
RCCSD(T)//M06-2X	aVTZ	-0.189	0.313	1.250	-0.961
UCCSD(T)		**0.000**	**0.000**	**0.000**	**0.000**

i. HOOH → 2 OH ii. HOOOH → HO + OOH
ii. $CH_3OOOH \rightarrow CH_3O + OOH$ iv. $CH_3OOOH \rightarrow CH_3OO + OH$
a. The active spaces and other details of the multireference calculations are explained in the "Multireference calculations" section

Based on these benchmark results, we performed the calculations for the formation and decomposition energies for the hydrotrioxides with the M06-2X functional. The conformer with the lowest zero-point vibrational

corrected electronic energy (E+ZPVE) at the M06-2X level (see section S4.1) is used for calculating the formation and decomposition energies. The calculations were also performed at the ωB97X-D level for comparison. For the smaller hydrotrioxides, a UF12 level single-point calculation was also performed on the M06-2X level lowest energy conformer. The formation and decomposition energies at the UF12 level are calculated using the UF12 level electronic energy and the M06-2X level ZPVE.

Calculated ROOOH formation and decomposition energies

The calculated formation energies [$E_f = E_{ROOOH} - (E_{ROO} + E_{OH})$] and decomposition energies [$E_d = (E_{RO} + E_{OOH}) - E_{ROOOH}$] for several atmospherically-relevant hydrotrioxides including those observed experimentally in this study are shown in Table S5. As expected from the benchmark test in Table S4, for all studied systems, the difference between E_f calculated at the M06-2X and UF12 levels is less than 1 kcal mol^{-1} and the values at the ωB97X-D level are about 3 kcal mol^{-1} lower than the M06-2X level values. The differences between E_d calculated at the M06-2X and UF12 levels are about 1 kcal mol^{-1}, while the ωB97X-D level values are generally 5-6 kcal mol^{-1} lower than the M06-2X level values.

Table S5. The formation energy (E_f) and the decomposition energy (E_d) for the atmospherically relevant hydrotrioxides calculated at the ωB97X-D/aug-cc-pVTZ level, the M06-2X/aug-cc-pVTZ level and the M06-2X level with a UCCSD(T)-F12a/VDZ-F12 single-point energy correction.

ROOOH structure	**Method**	**ωB97X-D**		**M06-2X**		**UCCSD(T)-F12a//M06-2X**	
	Parent compound	E+ZPVE [kcal mol^{-1}]					
		E_f	E_d	E_f	E_d	E_f	E_d
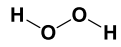	H_2O_2	46.7		47.7		47.2	
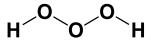	HOOOH	28.0		30.7		30.9	
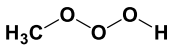	CH_3OOOH	-26.7	20.1	-29.6	24.4	-30.1	25.8
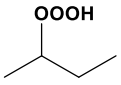	Butane	-26.0	21.1	-28.8	26.0	-29.6	27.4
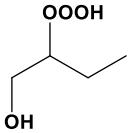	1-Butene	-26.5	20.0	-29.4	25.3	-30.3	26.4

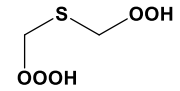	DMS	-29.7	19.5	-33.2	25.4	-33.0	25.3
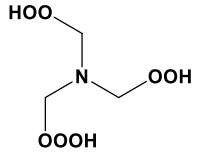	TMA	-31.7	24.3	-34.8	28.9	-35.0	30.0
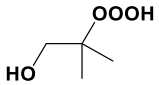	2-Methylpropene	-26.3	21.3	-29.5	26.5	-30.1	26.0
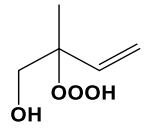	Isoprene	-27.2	21.1	-30.2	26.2	-30.9	27.2
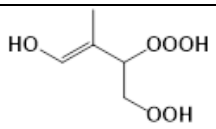		-26.4	18.8	-29.2	24.6	These calculations cannot be achieved with our computational resources.	
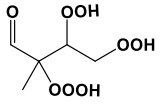		-28.2	18.0	-31.2	24.1		
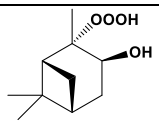	α-Pinene	-24.0	20.5	-26.9	23.6		
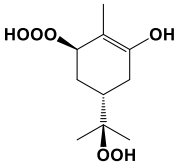		-27.1	22.1	-30.1	27.2		
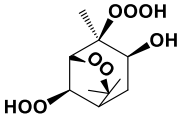		-26.8	21.5	-29.5	26.4		

As shown in Table S4 and Table S5, the decomposition energy of the hydrotrioxides at different levels of theory has fairly large differences. However, the trend in decomposition energies between different ROOOHs is similar at the different levels of theory (Fig. S38), for example, the decomposition energies of the ROOOH formed from TMA oxidation and HOOOH are significantly higher than of the other ROOOHs studied.

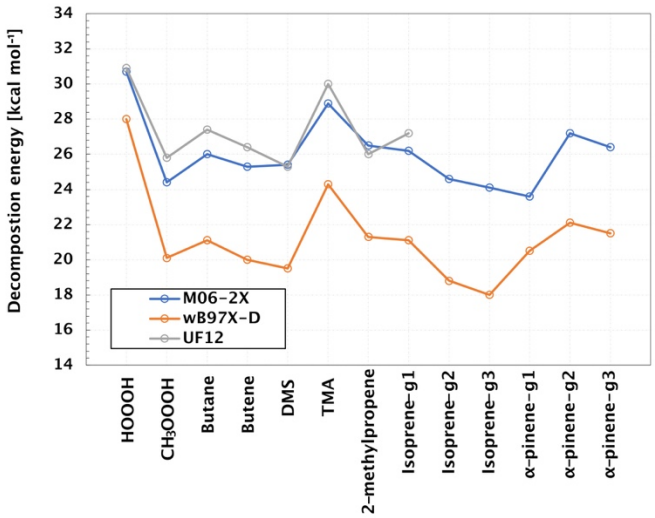

Fig. S38. The thermal decomposition energies of ROOOHs calculated at different levels of theory. The parent compounds of the hydrotrioxides are shown on the x-axis. Zero point vibrationally corrected electronic energies are shown.

Based on the multireference benchmark results for HOOH, HOOOH and CH_3OOOH, it seems reasonable to assume that the decomposition energy, E_d, of a hydrotrioxide is close to the decomposition reaction barrier, E_a. Within transition state theory, the reaction rate coefficient depends exponentially on the reaction barrier and the decomposition lifetime is inversely proportional to this rate coefficient.

The lifetime of the ROOOH formed by the OH-initiated oxidation of 2-methylpropene in the Caltech chamber experiment was determined to be about 20 min (see Section S1.7). This lifetime includes any loss of hydrotrioxide, in particular surface reactions on the chamber walls. Thus, 20 min is a lower limit of the gas-phase thermal lifetime of the ROOOH formed in the 2-methylpropene + OH oxidation (Fig. S33). If we compare the decomposition energies for hydrotrioxides that could be calculated at our highest level (UCCSD(T)-F12a), we see that they all have decomposition energies that are close to or higher than that of the hydrotrioxide formed from 2-methylpropene. Hence, we would expect these hydrotrioxides to have longer decomposition lifetimes than the 20 min. observed for the 2-methylpropene derived hydrotrioxide. One extreme is the ROOOH formed in the TMA+OH reaction, which has a barrier that is approx. 4 kcal mol^{-1} higher, which would lead to a thermal decomposition lifetime at 298K in the order of 5-10 days. For the other larger isoprene and α-pinene derived hydrotrioxides, their thermal decomposition lifetimes are comparable to the ROOOH formed through 2-methylpropene + OH and thermal lifetimes are expected to be similar.

S4.3. Photostability of hydrotrioxides

In addition to the thermal stability, we also investigate the photostability of ROOOHs. The electronic transitions of the hydrotrioxides are calculated with the time-dependent density functional theory (TD-DFT) calculations. We performed TD-DFT single point calculations on the lowest energy conformer of the hydrotrioxide at the M06-2X and ωB97X-D levels. For each hydrotrioxide, the first 20 singlet-singlet and singlet-triplet vertical excitations are calculated. No spin-orbital coupling was included thus all singlet-triplet transitions have 0 intensity in the calculation. All TD-DFT calculations were run with the Gaussain16 package.

The first singlet to singlet (S_0-S_1) and singlet to triplet (S_0-T_1) vertical excitation energies of the hydrotrioxides calculated at the M06-2X and the ωB97X-D level are shown in Table S6. The first singlet to singlet (S_0-S_1) transition of most ROOOHs are about 200 nm, except for the third generation ROOOH formed from isoprene + OH which has an S_0-S_1 transition of ~300 nm due to its -C=O functional group. The first singlet to triplet (S_0-T_1) transition is about 40 nm lower in energy than the S_0-S_1 transition for the studied ROOOHs.

We calculated the photolysis rate, J, of the third generation ROOOH formed from isoprene + OH which absorbs at significantly higher wavelengths than the other studied hydrotrioxides (Table S6) and thus is most likely to undergo photolysis in Earth's atmosphere. The photolysis rate, J, is calculated based on the wavelength λ, and oscillator strength, *f*, of the first 10 S_0-S_1 electronic transitions (covers the range of 300 - 170 nm) using the equation:

$$J = \int \sigma_{\lambda,T} \varphi_{\lambda,T} F_{\theta,T} \, d\lambda \qquad \text{(SXIIX)}$$

Where $\sigma_{\lambda,T}$ is the cross section of the molecule calculated from the oscillator strength and $\varphi_{\lambda,T}$ is the quantum yield of photolysis of the molecule, which is both a function of the temperature, T, and wavelength, λ. $F_{\theta,T}$ is the actinic flux as a function of the temperature, T, and the solar zenith angle, Θ. The actinic flux, $F_{\theta,T}$, at different altitudes (Θ = 0, equatorial region, 298.15K) is obtained from the TUV model (*58*) and the quantum yield, $\varphi_{\lambda,T}$, is assumed to be 1, to provide an upper limit. The absorption spectrum from the electronic transitions is simulated using a Gaussian band shape with a full width at half maximum of 4000 cm^{-1} for each transition.

The photolysis rate, J, of the third generation ROOOH formed from isoprene + OH is calculated to be 1.8×10^{-5} s^{-1} at 0 km altitude and 3.9×10^{-5} s^{-1} at 20 km altitude, which corresponds to an atmospheric lifetime with respect to photodissociation of 15 hours and 8 hours, respectively. For the other studied hydrotrioxides, the photolysis rate is smaller than 10^{-9} s^{-1} below 20 km altitude and will not be important for the atmospheric lifetime.

Table S6. The lowest singlet to singlet (S_0-S_1) and singlet to triplet (S_0-T_1) vertical excitation energies of hydrotrioxides calculated with TD-DFT using M06-2X and ωB97X-D functionals.

Parent compound	Structure	Vertical excitation energies [nm]			
		M06-2X		ωB97X-D	
		S_0-S_1	S_0-T_1	S_0-S_1	S_0-T_1
HOOOH	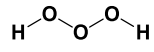	190.7	229.4	188.1	233.0
CH_3OOOH	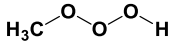	190.2	227.6	188.1	232.0
Butane	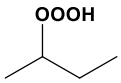	192.3	229.5	190.5	233.8
1-Butene	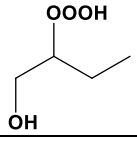	194.7	235.0	194.1	242.8
DMS	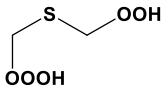	215.3	234.5	200.1	237.3
Isoprene	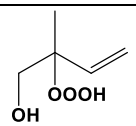	192.4	269.5	191.7	293.5
	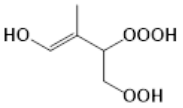	217.2	287.3	214.2	306.5
	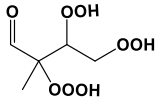	297.7	334.7	281.6	324.6
α-Pinene	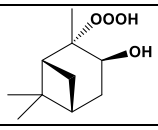	194.5	234.4	197.6	245.8
	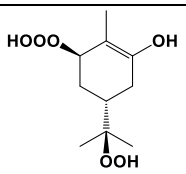	225.7	285.8	217.5	310.2
	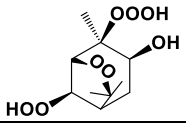	211.8	250.6	204.0	247.8
TMA	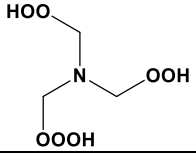	203.3	244.2	195.0	239.3

2-Methyl-propene	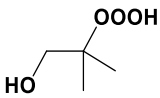	194.7	234.9	194.2	241.3

To assess the possibility of vibrational overtone pumping (*80-82*) of the OH-stretch as a means for dissociation of the hydrotrioxides, we have calculated the transition wavenumbers and oscillator strengths of the OH-stretching transitions in CH_3OOOH (Table S7). The values for Δv = 1-5 have been calculated numerically using a local mode approach based on 27 single-point calculations for OH bond lengths displacements of -0.4 Å to 0.9 Å from the optimized value at the B3LYP/aug-cc-pVTZ level. (*83*) For comparison, the values for Δv = 1-2 have been calculated using second-order vibrational perturbation theory (VPT2) as implemented in Gaussian 16. For the two frequencies where the calculations overlap, good agreement is observed for both the transition wavenumbers and oscillator strengths.

Table S7. Transition wavenumbers, $\tilde{\nu}$ and oscillator strengths, *f,* for the OH-stretching transitions in CH_3COOOH calculated using a 1D local mode model and the VPT2 method both at the B3LYP/aug-cc-pVTZ level.

	1D local mode		VPT2	
Δv	$\tilde{\nu}\ (cm^{-1})$	f	$\tilde{\nu}\ (cm^{-1})$	f
1	3541	5.47×10^{-6}	3531	5.26×10^{-6}
2	6918	1.01×10^{-6}	6893	1.02×10^{-6}
3	10131	5.84×10^{-8}	-	-
4	13185	3.81×10^{-9}	-	-
5	16083	3.64×10^{-10}	-	-

The UCCSD(T)-F12a/VDZ-F12 dissociation energy of CH_3OOOH is 25.8 kcal mol^{-1} (Table S5) corresponding to 9024 cm^{-1} and the other hydrotrioxides have comparable dissociation energies. Thus, the Δv = 3 transition provides enough energy to dissociate the hydrotrioxide. This transition has a calculated oscillator strength of 5.84×10^{-8}.

We calculated the photolysis rate, J, of CH_3OOOH based on the calculated $\Delta v = 3$ vibrational transition wavenumbers, $\tilde{\nu}$ and oscillator strength, *f*, based on equation SXIV. The vibrational band is simulated using a

Gaussian band shape with a full width at half maximum of 100 cm^{-1} (*84*) and we assume the quantum yield, $\varphi_{\lambda,T}$, to be 1 to provide an upper limit. The photolysis rate of CH_3OOOH via overtone pumping at 0 km altitude and 20 km altitude is calculated to be 1.5 $\times 10^{-6}$ s^{-1} and 1.8 $\times 10^{-6}$ s^{-1}, respectively. Thus, the atmospheric lifetime of the hydrotrioxides towards photodissociation by overtone pumping is on the order of 5-10 days. Compared to other pathways, this is thus negligible.

In summary, we expect no significant photolysis of the hydrotrioxides from either electronic transitions or vibrational overtone pumping in the troposphere, except for the third generation ROOOH formed from isoprene + OH.

S4.4. OH + isoprene: Addition to the double bond and hydrotrioxide formation

Addition of OH and O_2 to isoprene forms different isomers of the unsaturated peroxy radical ISOPOO, as exemplified in Fig. S39 for OH addition at the 1-position in isoprene. A number of possible reactions including interconversion via loss of O_2 complicate the dynamics of these peroxy radicals. (*63*) In addition to the OH addition to the terminal oxygen atom of the peroxy (RO_2) to form the hydrotrioxide, OH could react by addition to the double bond to form a hydroxy peroxy alkyl diradical (Fig. S39). H-abstraction is assumed to be negligible.

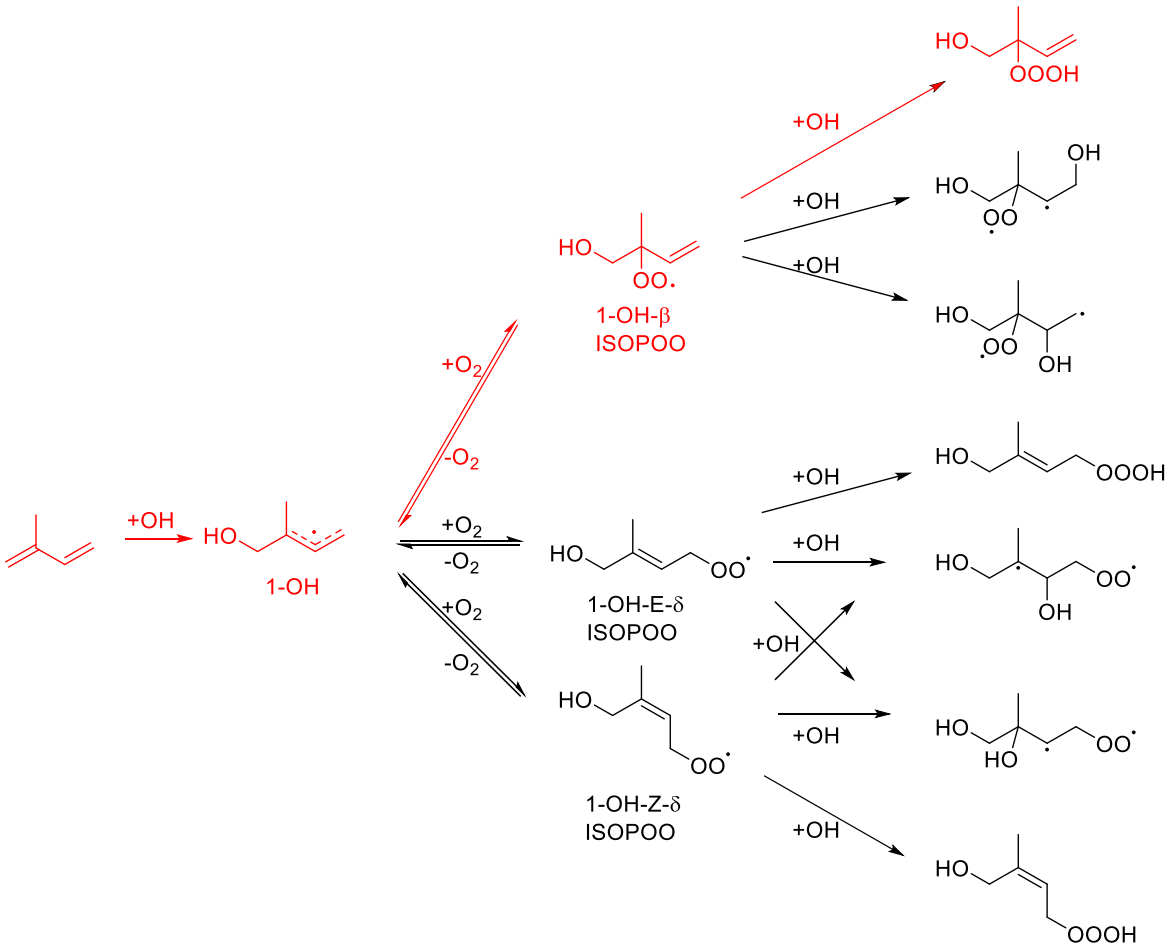

Fig. S39. Simplified route from isoprene to the isoprene-derived hydrotrioxides or hydroxy peroxy alkyl biradicals for addition to the 1-position in isoprene. The dominant route is given in red.

To assess the competition between addition to the double bond and the peroxy radical center, multireference calculations were performed for OH-addition to the terminal C of the double bond or to the peroxy radical in 1-OH-β ISOPOO.

For the diradical formation pathway, we first optimized the diradical with a [4e,4o] active space including the bonding and antibonding orbitals of the formed C-O bond and two radical orbitals at the CASSCF/cc-pVDZ level as a singlet. Then a relaxed scan was performed on the C-O bond from the equilibrium bond length of 1.43 Å to 10 Å at the same level. Subsequently, MRCI/cc-pVDZ level single points with the same active space were performed on the CASSCF level optimized scan steps. The same approach was used for the diradical formation on the triplet surfaces. The active spaces used for the diradical on the singlet and triplet surfaces are shown in Fig. S40.

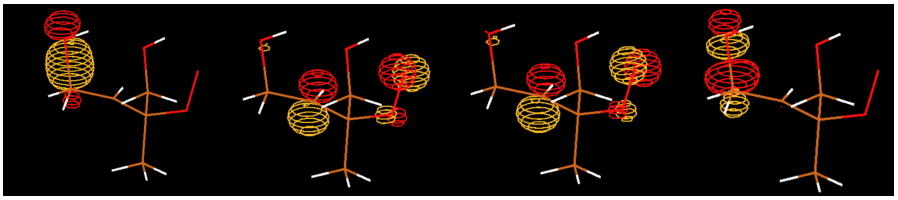

Singlet				
Occupation	1.97	1.08	0.92	0.03

Triplet				
Occupation	1.98	1.01	0.97	0.04

Fig. S40. The orbitals in the [4e,4o] active space used for the diradical formation on the singlet and triplet surfaces. The bonding and antibonding orbitals of the C-O bond are the same for both singlet and triplet. For the 2 singly occupied radical orbitals, the singlet state has the orbitals delocalized over both carbon and the peroxy oxygen atoms while the triplet state has the orbitals either localized on the carbon atom or the peroxy oxygen atom.

The orbital transformation of the 4 orbitals in the active space during the diradical formation on the singlet surface is shown in Fig. S41. The preexisting peroxy radical orbital remains unchanged during the diradical formation as expected.

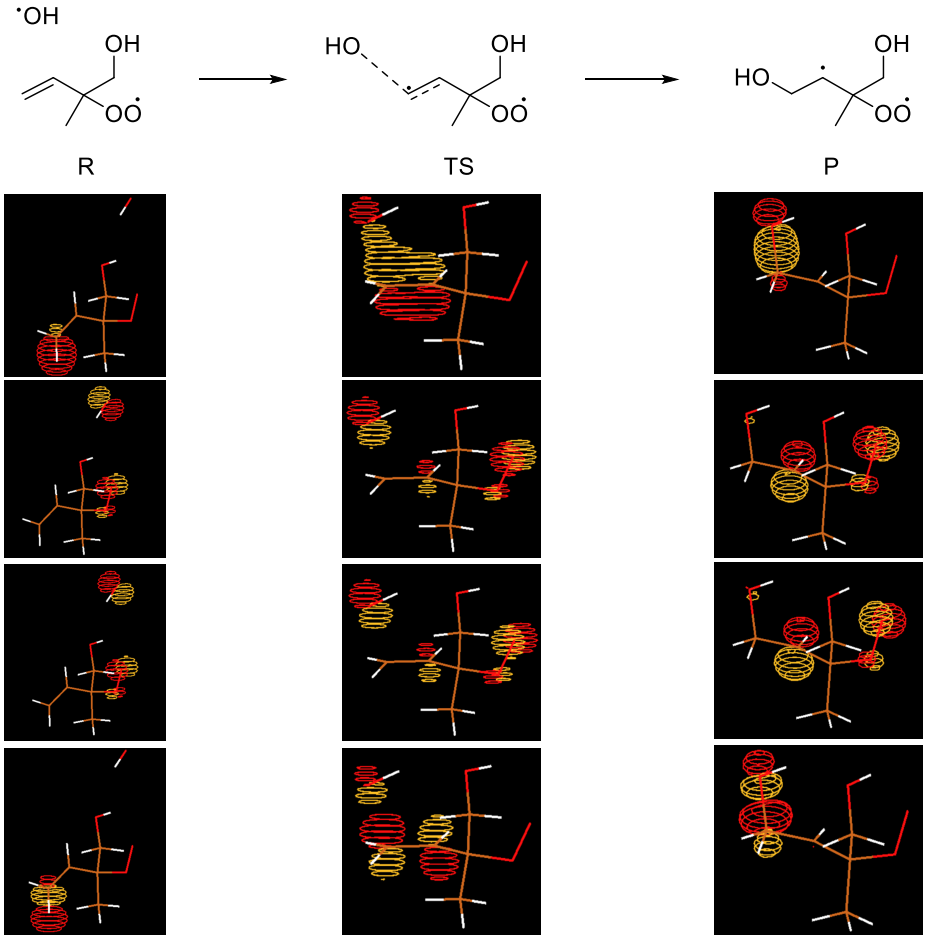

Fig. S41. The orbital transformation of the 4 orbitals in the active space during the diradical formation on the singlet surface.

For the hydrotrioxide formation, the hydrotrioxide is optimized with a [2e,2o] active space which only includes the bonding and antibonding orbital of the formed O-O bond at the CASSCF/cc-pVDZ level. This is followed by a relaxed scan of the O-O bond distance from the equilibrium of 1.48 Å to 10 Å at the same level, and the MRCI/cc-pVDZ level single point energy calculations on the CASSCF optimized geometries. The orbitals in the [2e,2o] active space used for the hydrotrioxide formation are shown in Fig. S42.

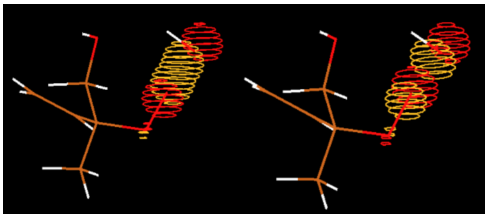

Occupation	1.97	0.03

Fig. S42. The orbitals in the [2e,2o] active space used for the hydrotrioxide formation.

The scans at the MRCI/cc-pVDZ//CASSCF/cc-pVDZ level on the singlet and triplet potential surface for the diradical formation and the hydrotrioxide formation on the singlet surface are shown in Fig. S43. The MRCI level results suggest that the diradical has nearly degenerate singlet and triplet states. The singlet state of the formed diradical is 0.12 kcal mol^{-1} lower in energy than the triplet state. The scan results suggest that the barrier for OH addition to the double bond is significantly higher than the addition to the peroxy radical, thus the diradical formation is unlikely.

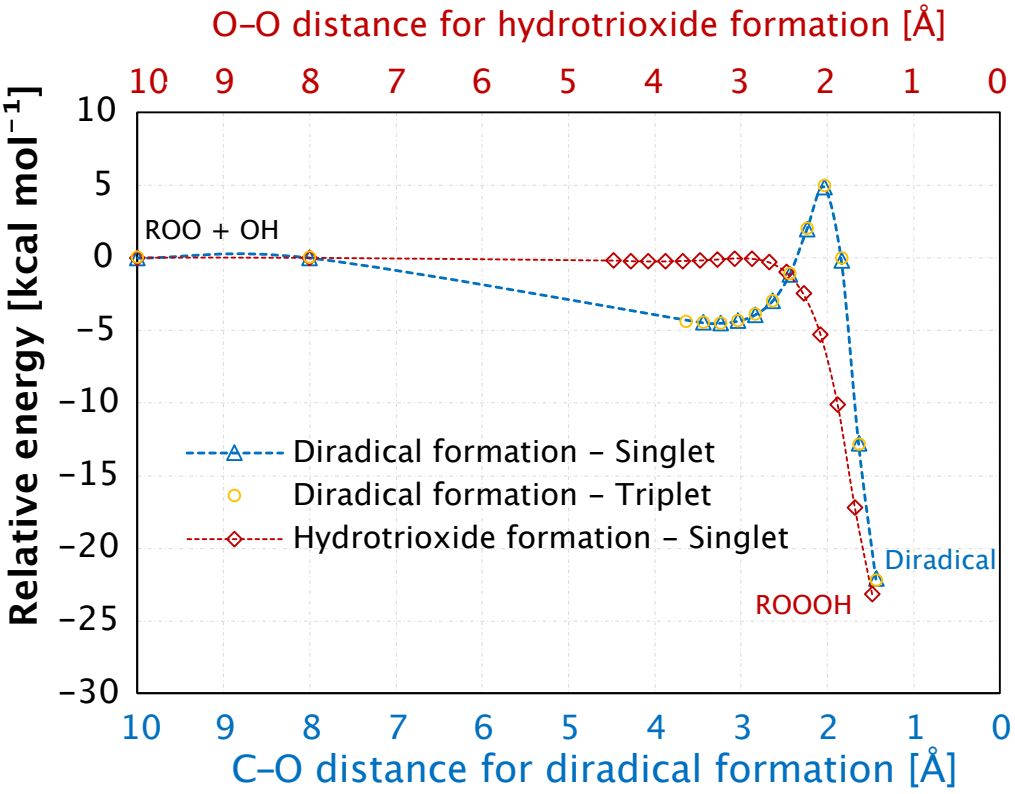

Fig. S43. The MRCI/cc-pVDZ//CASSCF/cc-pVDZ level relaxed scan of HO reacting with the 1-OH-β ISOPOO by double bond addition on the singlet (blue) and triplet (yellow) surface, and the hydrotrioxide formation (red) on the singlet surface. The double bond addition pathway (blue and yellow) has a higher barrier than the hydrotrioxide formation pathway (red). The products from the two reaction pathways (biradical R'-C-C-OH and the hydrotrioxide ROOOH) have similar relative energies compared to the reactants.

S4.5. Reaction of OH radicals with hydrotrioxides

In this section, we studied the reactions and possible products from the hydrotrioxides reacting with OH radicals. All calculations in this section are at the B3LYP/6-31+G(d) level. Conformer samplings were performed as described before in section S4.1. The B3LYP level reaction rate coefficients are calculated using the MC-TST approach as described in (*71*).

Reaction of OH radicals with the first-generation isoprene-derived hydrotrioxide

Due to the atmospheric importance of isoprene, we first studied the possible oxidation pathways for the first-generation hydrotrioxide ($HO\text{-}C_5H_8OOOH$) formed from OH + isoprene (Fig. S44).

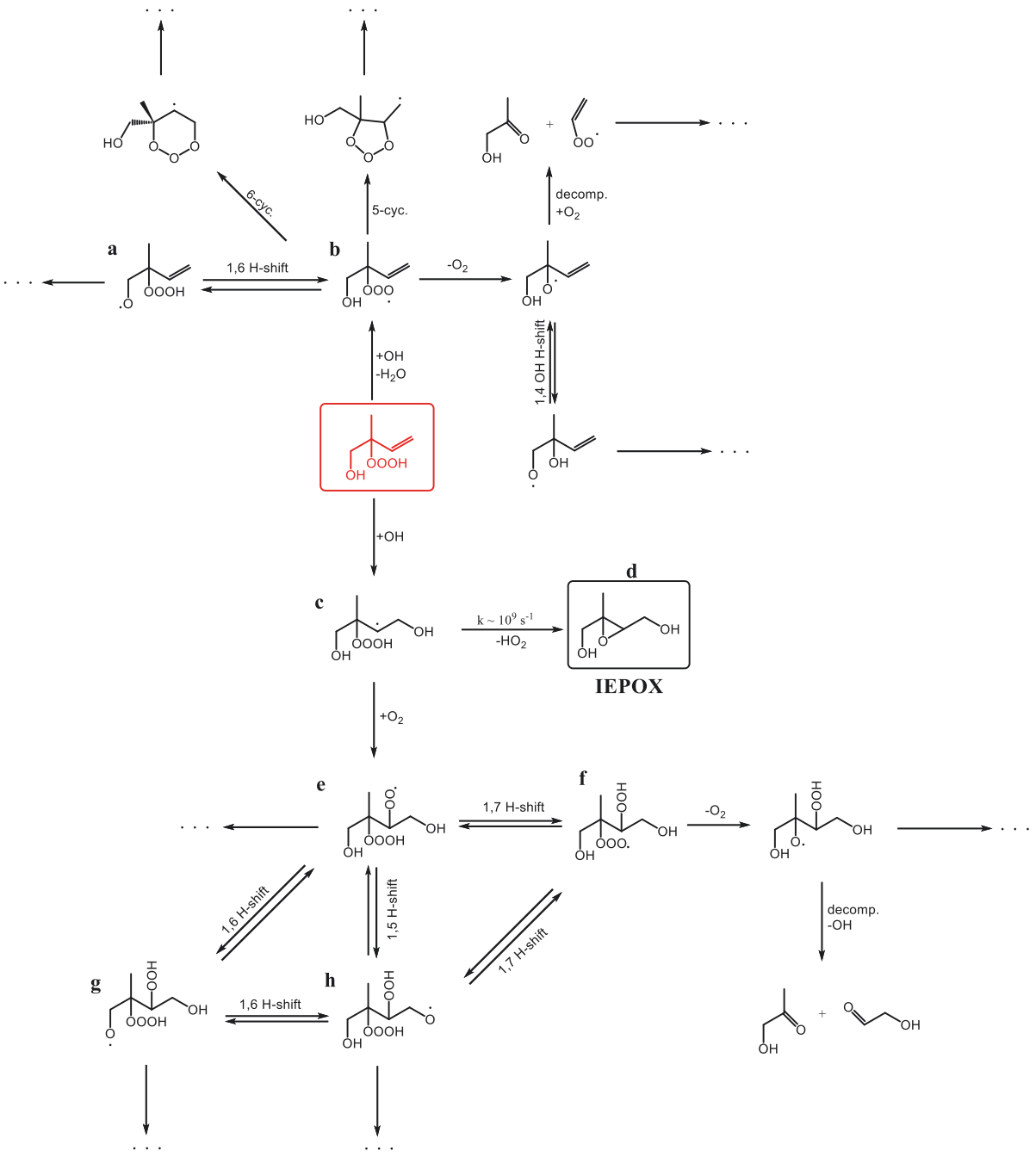

Fig. S44. Possible OH-initiated reactions for the first-generation hydrotrioxide (HO-C_5H_8OOOH) formed from OH + isoprene. The hydrotrioxide HO-C_5H_8OOOH is marked with a red box. The major product IEPOX is marked with a black box.

The hydrotrioxide HO-C_5H_8OOOH can react with OH radicals by either OH addition to the double bond or H-abstraction reactions. The corresponding isoprene-derived hydroperoxide HO-C_5H_8OOH (ISOPOOH) has been shown to react with OH radical mainly through the OH addition pathway and forming the isoprene dihydroxy epoxide (IEPOX).(*22*) We calculate the O-H binding energies in the -OOOH and the -OH groups of the hydrotrioxide HO-C_5H_8OOOH to be 72 kcal mol^{-1} and 96 kcal mol^{-1}, respectively. For comparison, the O-H binding energy in the -OOH group of the hydroperoxide HO-C_5H_8OOH is calculated to be 76 kcal mol^{-1}. The results suggest similar O-H binding energies in the -OOOH and -OOH group, thus we also expect the OH addition to be the major route for the hydrotrioxide HO-C_5H_8OOOH. We found that the OH addition product of the hydrotrioxide (structure **c** in Fig. S44) can undergo a very rapid unimolecular reaction forming the IEPOX (structure **d** in Fig. S44) and an HO_2 radical. This reaction has a barrier of only 4.8 kcal mol^{-1}, and the reaction rate coefficient is 10^9 s^{-1} at the B3LYP level. The reaction barrier of the corresponding hydroperoxide leading to IEPOX and OH radical was calculated to be 4.9 kcal mol^{-1}. (*85*) Therefore, IEPOX formation is also likely the dominant route for the hydrotrioxide HO-C_5H_8OOOH.

In addition to this primary pathway leading to IEPOX formation, we have also investigated some other minor pathways. For the OH addition pathway, another possibility is the O_2 addition forming structure **e** in Fig. S44. It is known that H-shifts between the alkoxy and peroxy groups are rapid and will reach equilibrium within ~10^{-7} s. (*14*) We have calculated the H-shift reaction between the peroxy group and the trioxy group, and the results suggest that the barrier for such a H-shift is about 8 kcal mol^{-1} ($k \sim 10^8$ s^{-1}) thus also rapidly reaching equilibrium. Therefore, the distribution between structures **e**, **f**, **g** and **h** depends on their relative energies. Our calculation suggests that the trioxy radical (**f**, ROOO) has the lowest energy, and the relative energies of **e** (ROO), **g** (RO) and **h** (RO) against **f** are 4.8 kcal mol^{-1}, 19.6 kcal mol^{-1}, and 18.1 kcal mol^{-1}, respectively. This means the trioxy radical is the most favored and the two alkoxy radicals are very unfavored in the equilibrium. The same trend is observed for structures **a** and **b** formed from the H-abstraction pathway, where the trioxy radical **b** is 23.9 kcal mol^{-1} more stable than the alkoxy radical **a**. The reaction barrier of the two cyclization reactions (6-cyc and 5-cyc) from the structure **a** are calculated to be 20 kcal mol^{-1} and 18 kcal mol^{-1}, respectively. A previous theoretical study has shown that for the trioxy radical CH_3OOO, the decomposition reaction leading to the alkoxy radical CH_3O and singlet oxygen, $CH_3OOO \rightarrow CH_3O + {}^1O_2$, only has a barrier of approximately 6 kcal mol^{-1} and is the dominant route for the CH_3OOO radical. (*86*) Thus we expect the alkoxy formation is also the major route for the trioxy radicals **b** and **f**.

Overall, the IEPOX formation is likely the major route for the first-generation hydrotrioxide (HO-C_5H_8OOOH) formed from OH + isoprene in the gas phase, with alkoxy radical formation being minor pathways.

Reaction of OH radicals with TMA- and butene-derived hydrotrioxide

Besides the unsaturated hydrotrioxide formed by isoprene + OH, we also studied the OH reactions of the saturated hydrotrioxides derived from TMA and butene (Fig. S45 and Fig. S46). For such hydrotrioxides without a C=C double bond, the OH H-abstraction from the -OOOH and the -OOH (if present) groups are expected to be the dominant pathways.

The TMA-derived hydrotrioxide $(HOOCH_2)_2NCH_2OOOH$ (Fig. S45, red) has two hydroperoxide groups and a hydrotrioxide group. Irrespective of which of the O-H hydrogens is abstracted, we calculate that the equilibrium between the peroxy and trioxy radicals via the 1.8 H-shift is reached within ~10^{-7} s. The trioxy radical is 5.6 kcal mol^{-1} more stable than the peroxy radical and the equilibrium concentration ratio between the trioxy (ROOO) and the peroxy radical (ROO) is approximately 200 to 1, with the trioxy radical being favored. Therefore, the formation of the alkoxy radical $(HOOCH_2)_2NCH_2O$ and $^1O_2$ is likely the major route of the TMA-derived hydrotrioxide, as noted from the isoprene-derived trioxy radicals above. The two amides formed by 1,5 H-shift from the peroxy radical can only be minor products.

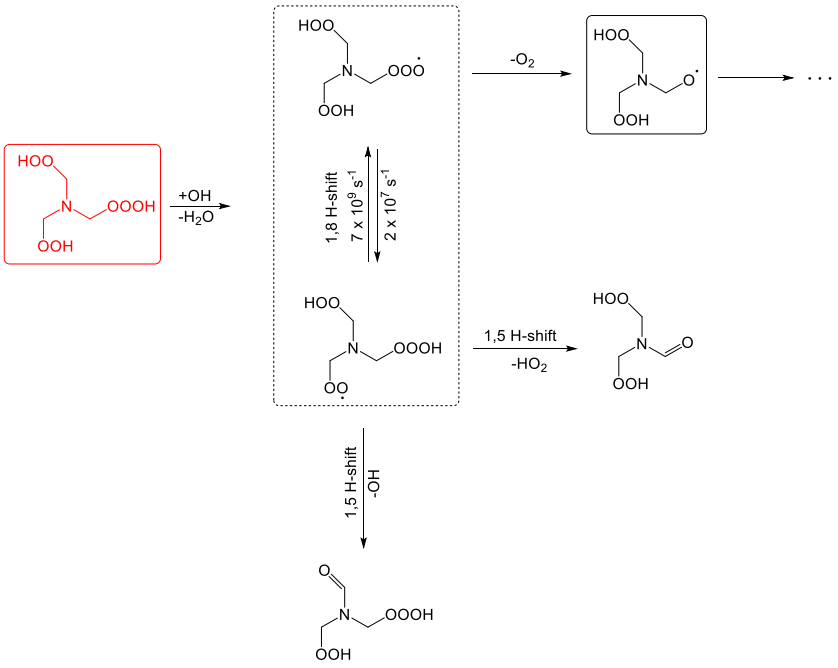

Fig. S45. Possible OH-initiated reactions for the hydrotrioxide formed from OH + TMA. The hydrotrioxide $(HOOCH_2)_2NCH_2OOOH$ is marked with a red box. The expected alkoxy radical formed from the dominant route is marked with a black box.

For the butene-derived hydrotrioxide HO-C_4H_8OOOH, we expect the OH H-abstraction from the -OOOH group forming the trioxy radical to be the dominant pathway (Fig. S46). The equilibrium between the trioxy radical (ROOO) and the alkoxy radical (RO) is calculated to greatly favor the trioxy radical side (Fig. S46), due to the trioxy radical being 23 kcal mol^{-1} more stable than the alkoxy radical. This trend agrees with what we observed for the isoprene and TMA-derived hydroperoxides. We do not expect the formed trioxy radical to have other unimolecular reactions that can compete with the O_2 loss reaction, thus the formation of the alkoxy radical $HOCH_2CH(O)CH_2CH_3$ is expected to be the major route.

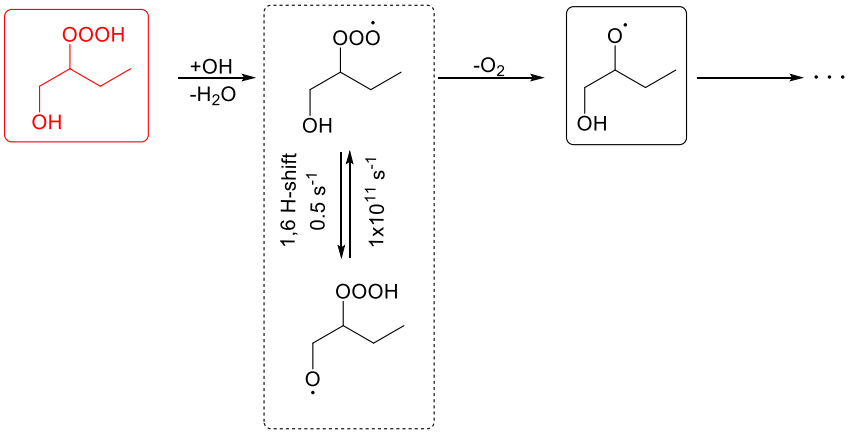

Fig. S46. Possible OH-initiated reactions for the hydrotrioxide formed from OH + butene. The hydrotrioxide HO-C_4H_8OOOH is marked with a red box. The expected alkoxy radical formed from the dominant route is marked with a black box.

S4.6. Water-catalyzed alcohol formation from hydrotrioxides

Hydrotrioxides are known for generating singlet oxygen, $^1O_2$, and alcohol (ROH) in the liquid phase (*1*) and the hydrotrioxide CH_3OOOH has drawn attention due to its potential of forming CH_3OH in the atmosphere (*5*). The direct reaction of $CH_3OOOH \rightarrow CH_3OH + {}^1O_2$ in the gas phase has been shown to be unlikely (*7, 86, 87*). Here, we studied the possibility of the reaction $ROOOH \rightarrow ROH + {}^1O_2$ catalyzed by H_2O in the gas phase.

We have shown that the hydrotrioxides formation is a generic route for many atmospheric RO_2 radicals, therefore, the structure $(CH_3)_3CCH_2OOOH$ is used for calculations in this section as a model system for the hydrotrioxides. We calculated the reaction barriers and reaction rate coefficients (Table S8) for the 2 reactions shown in Fig. **S47**, as well as the equilibrium constant for the formation of the $(CH_3)_3CCH_2OOOH{\bullet}H_2O$ complex in the gas phase (Table S9). The reaction rate coefficients are calculated by the IRC-TST approach (*71*) where the reactant (R) and product (P) are the optimized IRC endpoints of the TS and only one conformer of the R, TS and P is included.

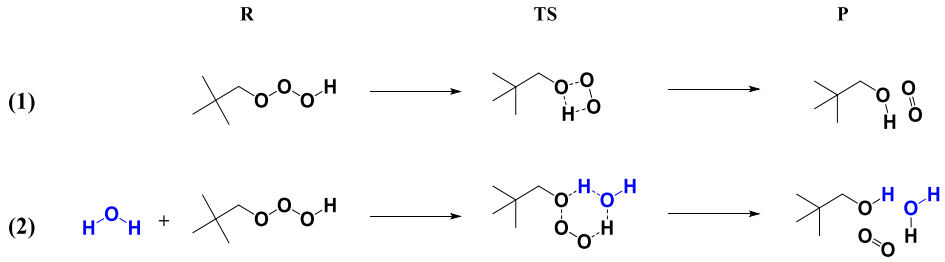

Fig. S47. Formation of alcohol and singlet O_2 from hydrotrioxide without (1) and with (2) water catalysis.

The calculated reaction barriers and reaction rate coefficients for the reactions in Fig. S47 at the B3LYP, M06-2X, ωB97X-D and ROCCSD(T)-F12 levels (see section S4.2) are shown in Table S8. The water-catalyzed reaction (reaction 2 in Fig. S47) is treated as a unimolecular reaction where the reactant is the $ROOOH{\bullet}H_2O$ complex. With H_2O as the catalyst, the reaction barrier decreases from approximately 41 kcal mol^{-1} to approximately 22 kcal mol^{-1}. This is not overly surprising since the involvement of H_2O changed the TS structure from an unfavorable 4-membered ring to a 6-membered ring. The reaction rate coefficient increases by more than 10 orders of magnitude with H_2O catalysis, which is in line with previous knowledge that ROOOH generates $^1O_2$ in the liquid phase. (*1*)

Table S8. The calculated reaction barriers, E_a (kcal mol^{-1}), and unimolecular rate coefficients, k_{uni} (s^{-1}), at different levels for the reactions shown in Fig. S47. Energies shown are zero point vibrationally corrected electronic energies.

Reaction	B3LYP/6-31+G(d)		M06-2X/aug-cc-pVTZ		ωB97X-D/aug-cc-pVTZ		ROCCSD(T)-F12/VDZ-F12//ωB97X-D/aug-cc-pVTZ	
	E_a	k_{uni}	E_a	k_{uni}	E_a	k_{uni}	E_a	k_{uni}
(1)	41.4	5.4×10^{-14}	45.5	4.5×10^{-20}	44.2	3.5×10^{-17}	41.2	5.7×10^{-15}
(2)	20.6	8.0×10^{-3}	26.3	3.8×10^{-7}	24.8	1.2×10^{-5}	22.6	5.1×10^{-4}

The water-catalyzed reaction proceeds as:

$$ROOOH + H_2O \rightleftharpoons ROOOH \cdot H_2O \xrightarrow{k_{uni}} ROH + {}^1O_2 + H_2O \quad \text{(SXIX)}$$

The total bimolecular reaction rate coefficient, k_{tot}, of ROOOH reacting with H_2O forming ROH + $^1O_2$ + H_2O is thus described by

$$k_{tot} = \frac{k_f}{k_d P^\theta} k_{uni} = \frac{K_{eq}}{P^\theta} k_{uni} \quad \text{(SXX)}$$

where P^θ is the standard pressure, k_f and k_d is the forward and backward reaction rate coefficients of the equilibrium $ROOOH + H_2O \rightleftharpoons ROOOH \cdot H_2O$, respectively, and K_{eq} is its equilibrium constant. Whether the H_2O-catalyzed reaction is important in the atmosphere, thus, also depends on the equilibrium constant, K_{eq}, for the complexed formation. In Table S9, we show the calculated equilibrium constant and the corresponding bimolecular reaction rate, k_{tot}, at different levels of theory, where the lowest energy conformer of ROOOH and the complex from the IRC endpoints of the H_2O catalysis reaction are used. The reaction rate coefficients obtained from different levels of calculations show 5 orders of magnitude difference, where the B3LYP level gives the fastest reaction rate coefficients.

We estimate the pseudo-first-order reaction rate coefficient, $k_{pseudo} = k_{tot} \times [H_2O]$, at 100 % RH and 298 K, 1 atm ($[H_2O] \sim 7\times10^{17}$ molecule cm^{-3}). At the B3LYP level, k_{pseudo} for the H_2O-catalyzed reaction is about 10^{-5} s^{-1} with 100 % RH, which should be the upper limit. This is comparable to an estimated pseudo-first-order rate coefficient of the competing ROOOH + OH reaction (k ~10^{-11} molecule^{-1} cm^3 s^{-1} and [OH] = 10^6 molecule cm^{-3}). As such, gas-phase decomposition (H_2O-catalyzed or uncatalyzed) into ROH + $^1O_2$ is unlikely to play a major role in the atmosphere compared to e.g. reaction with OH and transfer to the aerosol phase. This result supports our experimental observation that the measured ROOOH concentrations are independent of RH (see Fig. S3).

Table S9. Calculated equilibrium constants, K, of $(CH_3)_3CCH_2OOOH$ bound with H_2O at 298.15 K, and the unimolecular, bimolecular, and pseudo-first-order reaction rate coefficients for decomposition into ROH + $^1O_2$ with H_2O catalysis calculated at different levels of theories.

Level of calculations	K	k_{uni} [s^{-1}]	k_{tot} [cm^3 $molecule^{-1}$ s^{-1}]	k_{pseudo} (RH:100 %, T:298 K, p:1 atm)
B3LYP	0.048	8.00×10^{-3}	1.51×10^{-23}	1.1×10^{-5}
ωB97X-D	0.020	4.00×10^{-7}	3.15×10^{-28}	2.2×10^{-10}
M06-2X	0.103	1.30×10^{-5}	5.24×10^{-26}	3.7×10^{-8}
ROCCSD(T)-F12	0.046	5.20×10^{-4}	9.43×10^{-25}	6.6×10^{-7}